Title
Grasper Integrated Miniaturized Tri-Axial Force Sensor System for Robotic Minimally Invasive Surgery

Author
Dai, Yuan

Publication Date
2018

Peer reviewed|Thesis/dissertation

UNIVERSITY OF CALIFORNIA

Los Angeles

Grasper Integrated Miniaturized Tri-Axial Force Sensor System for Robotic Minimally Invasive Surgery

A dissertation submitted in partial satisfaction of the

requirements for the degree Doctor of Philosophy

in Electrical and Computer Engineering

by

Yuan Dai

2018

ABSTRACT OF THE DISSERTATION

Grasper Integrated Miniaturized Tri-Axial Force Sensor System for Robotic Minimally Invasive Surgery

by

Yuan Dai

Doctor of Philosophy in Electrical and Computer Engineering

University of California, Los Angeles, 2018

Professor Robert N. Candler, Chair

Minimally invasive surgery (MIS) has gained popularity over traditional open surgery due to its advantages of decreased incision size and pain to the patient, lower risk of infection, and shorter recovery time. Recent developments in robotic surgical systems have shown promise to further advance MIS by offering the surgeons with increased manipulability and dexterity along with 3D vision.

However, the lack of tactile feedback is the key feature that is needed for robotic surgery to reach its full potential. Recent research efforts have successfully integrated some degree of tactile feedback components onto surgical robotic instruments, and have shown significant improvement of the outcome of the surgical performance. The primary barrier to the adoption of tactile feedback in clinical use is the unavailability of suitable tri-axial force sensing technologies that can be integrated with the medical instruments. Besides well-understood normal force sensing, shear force sensing is also critical in clinical tasks, such as suturing, where shear sensing could prevent breakage of sutures due to excessive shear force.

This paper describes the design, batch microfabrication, and characterization of a miniature force sensor for providing haptic feedback in robotic surgical systems. We demonstrate for the first time a microfabricated sensor that can provide triaxial sensing (normal, x-shear, y-shear) in a single sensor element that is integrated with commercial robotic surgical graspers. Features of this capacitive force sensor include differential sensing in the shear directions as well as a design where all electrical connections are on one side, leaving the backside pristine as the sensing face for surgical tasks.

The sensor readout is performed by a custom-designed printed circuit board with 24-bit resolution. The integration of read-out circuits with the capacitive sensor is designed on two printed circuit boards that can be clipped together, providing the possibility for disposable sensors. The sensing system is first connected to the LabVIEW-based controller, to convert the analog capacitor signal to a digital signal representing force. After the functionality of the sensor is proven, the tactile sensor system is then integrated with our custom Visual Studio based feedback control system.

Initial LabVIEW results validate the batch fabrication of the capacitive sensors and the design of the control circuit. The sensor is characterized using a sensing circuit with a *24*-bit resolution at *11 Hz-109 Hz*. With the LabVIEW program, the sensor and the readout circuitry contribute to a noise down to *0.8 fF* to the normal *z*-direction, *0.2 fF* to the shear *x*-direction, and *0.9 fF* to the shear *y*-direction at 8 Hz bandwidth.

The grasper integrated sensor system uses an Arduino based controller to multiplex between x, y, and z directions, providing *24* packets of tri-axial data per second to the Visual Studio-based computer application, with down to *0.094 fF* capacitance noise to the normal z-direction, *0.078 fF* to the shear x-direction, and *0.0825 fF* to the shear y-direction at *87.2 Hz* bandwidth. The sensitivity measured for the sensor is *14.58 fF/N* for normal z direction, *0.83 fF/N* for the shear x direction, and *0.62 fF/N* for the shear y direction. We report a normal resolution of *6.45 mN*, x-shear resolution of *94.7 mN*, and y-shear resolution of *133 mN*, all of which are more than sufficient for clinically relevant forces. A data latency of less than *42 ms* is achieved to obtain a triaxial data package and transmit it to the computer through the WiFi network.

A user study has been performed to tackle the suture breakage phenomenon that occurs during robotic surgery with the application of excessive forces due to lack of haptic feedback. The work aims to develop and validate a bi-axial shear feedback system that warns the operator to anticipated suture breakage. The benefits of a suture breakage warning system may be a reduced incidence of suture failure with otherwise equivalent knot quality during the tying procedure.

Biaxial shear sensors were placed on the Cadiere grasper tips of a da Vinci robotic surgical system. *17* novice subjects were then instructed to tighten 10 knots made from Silk *3-0* sutures, five times with the Haptic Feedback System (HFS) enabled, and five times with the system disabled (i.e., without any feedback). During each trial, the number of suture breakages was recorded. After trial completion, knots were evaluated for tightness. This was accomplished by measuring the amount of knot slippage following knot tying. Additional metrics recorded were the time required for completing each trial and both the average force and peak force applied in each trial.

Seven suture failures occurred in trials with HFS enabled while seventeen occurred in trials without feedback. The biaxial shear sensing system reduced the incidence of suture failure by 59% ($p = 0.0371$). It also resulted in 25% lower average applied force in comparison to trials without feedback ($p = 0.00034$), which is relevant because average force was observed to play a role in suture breakage (p=0.03925). Results of a *55%* decrease in standard deviation of quality knots tied with HFS also indicate an improvement in consistency when using the feedback system.

These results suggest this system may improve outcomes related to knot tying tasks in robotic surgery and reduce instances of suture failure while not degrading the quality of knots produced.

The dissertation of Yuan Dai is approved.

William J Kaiser

Ankur M Mehta

Veronica Santos

Pei-Yu Chiou

Robert Candler, Committee Chair

University of California, Los Angeles

2018

ACKNOWLEDGMENTS

First and foremost, I want to express my sincere gratitude to my advisor Prof. Rob Candler. I appreciate all his contributions of time, ideas, encouragement, motivation, kindness, and funding to make my Ph.D. experience productive and delighted. His guidance helped me in all the time of research and writing of this thesis. I could not have imagined having a better advisor and mentor for my Ph.D. study.

Besides my advisor, I would like to thank the rest of my thesis committee: Prof. William Kaiser, Prof. Eric Chiou, Prof. Veronica Santos, and Prof. Ankur Mehta for their insightful comments and encouragement.

My sincere thanks also goes to Dr. Erik Dutson, who proposed the project and gave me access to the research facilities. I was funded by the NIH award #R01EB019473-02. I gratefully acknowledge the funding sources that made my Ph.D. work possible.

For the measurement and testing with da Vinci surgical robot, I would like to thank group members in Prof. Grundfest's group, Ahmad Abiri, Jake Pensa, Anna Tao, Songping Sun, and of course, Prof. Warren Grundfest.

I would like to thank the Nanoelectronics Research Facility (NRF) and the Integrated Systems Nanofabrication Cleanroom (ISNC) in the California NanoSystems Institute (CNSI) at UCLA for making fabrication of the devices possible. We would also like to express our gratitude to The Center for High Frequency Electronics (CHFE) at UCLA for valuable discussion and suggestions.

The members of the Sensors and Technology Laboratory have contributed immensely to my personal and professional time at UCLA. The group has been a source of friendships as well as good advice and collaboration. I am especially grateful for the fun group members: Max Ho, Sidhant Tiwari, Jimmy Wu, Zhuyun Xiao, Ling Li, Siyuan Liu, and Ben Pound. Other past and present group members that I have had the pleasure to work with or alongside of are grad students Omeed Paydar, Hyumin Sohn, Srikanth Lyer, Jonathan Lake, Yongha Hwang –thank you.

Last but not least, I would like to thank my family for all their love, support, and encouragement. Special thanks to my mom who loves me and supports me in all my pursuits. And for my loving, supportive, encouraging, and patient husband Qiming, thank you.

VITA

Education

B.S. | University of Illinois, Urbana-Champaign| Electrical and Computer Engineering 2012

Honors & Awards: Graduated with Honor, Dean's List every year

Research Experiences

Sensors and Technology Laboratory 2013-2018

Pop's Laboratory 2010-2012

Journal Publications

8. **Y. Dai**, A. Abiri, J. Pensa, S. Liu, O. Paydar, H. Sohn, P. A. Pellionisz, C. Pensa, P. Dutson, W. S. Grundfest, R. N. Candler, "Biaxial Sensing Suture Breakage Warning System for Robotic Surgery," *IEEE Trans. on Biomedical Engineering*, under review
7. **Y. Dai**, S. Liu, O. Paydar, A. Abiri, H. Sohn, P. A. Pellionisz, E. P. Dutson, W. S. Grundfest, R. N. Candler, "Compact Triaxial Haptic Sensing System for Minimally Robotic Surgery," *Sensors and Actuators*, under review
6. A. Abiri, S. J. Askari, Y. Juo, A. Tao, **Y. Dai**, J. Pensa, R. N. Candler, E. P. Dutson, W. S. Grundfest, "Suture Breakage Warning System for Robotic Surgery," *IEEE Trans. on Biomedical Engineering,* 2018
5. F. Xiong, S. Deshmukh, S. Hong, **Y. Dai**, A. Behnam, F. Lian, E. Pop, "SANTA: Self-Aligned Nanotrench Ablation via Joule Heating for Probing Sub-20 nm Devices*," Nano Research*, 2016
4. F. Xiong, S. Hong, **Y. Dai**, A. Liao, E. Pop, "Sub-20 nm Self-Aligned Trench Formation via Joule Heating," in review at *Nanoscale*, (2016)
3. F. Xiong, **Y. Dai**, S. Hong, A. Behnam, Y. Cui, E. Pop, "Electrical breakdown of Carbon Nanotubes Due to Oxygen Collisions," in review at *Nano Research*, (2016)
2. A. Behnam, F. Xiong, A. Cappelli, N.C. Wang, E. Carrion, S. Hong, **Y. Dai**, A. Lyons, E. Chow, E. Piccinini, C. Jacoboni, E. Pop, "Nanoscale Phase Change Memory with Graphene Ribbon Electrodes," *Applied Physics Letters*, DOI: 10.1063/1.4931491 (2015)
1. F. Xiong, **Y. Dai**, M.-H. Bae, A.D. Liao, A. Behnam, E. Carrion, S. Hong, D. Ielmini, E. Pop, "Self-Aligned Nanotube-Nanowire Phase Change Memory," *Nano Letters*, DOI: 10.1021/nl3038097 (2013)

Conference Publications

12. **Y. Dai,** S. Liu, O. Paydar, A. Abiri, A. Tao, S. Sun, E. P. Dutson, W. S. Grundfest, R. N. Candler, "Miniature High Resolution Multi-Axis Force Sensor for Haptic Robotic Surgery",

The 40th Annual International Conference of the *IEEE Engineering in Medicine and Biology Society (EMBC'18),* 2018

11. **Y. Dai,** A. Abiri, S. Liu, O. Paydar, H. Sohn, E. P. Dutson, W. S. Grundfest, R. N. Candler, "Grasper Integrated Tri-Axial Force Sensor System for Robotic Minimally Invasive Surgery", The 39th Annual International Conference of the *IEEE Engineering in Medicine and Biology Society (EMBC'17),* 2017
10. **Y. Dai,** O. Paydar, A. Abiri, Z. Xiao, X. Guan, S. Liu, A. Tao, E. P. Dutson, W. S. Grundfest, R. N. Candler, "Miniature Multi-axis Force Sensor for Haptic Feedback System in Robotic Surgery", The 38th Annual International Conference of the *IEEE Engineering in Medicine and Biology Society (EMBC'16),* 2016
9. A. Abiri, X. Guan, **Y. Dai**, A. Tao, Z. Xiao, E. P. Dutson, R. N. Candler, W. S. Grundfest, "Depressed-Membrane Pneumatic Actuators for Robotic Surgery," The 38th Annual International Conference of the *IEEE Engineering in Medicine and Biology Society (EMBC'16),* 2016
8. J. Lake, Y.-H Hwang, E. Ng, C.-H. Ahn, V. Hong, Y. Yang, **Y. Dai**, R. N. Candler, "Experimental Validation of 3D Intuitive Modeling Approach for Anchor Loss In Mems Resonators", *Proceedings of Solid State Sensors, Actuators, and Microsystems Workshop (Hilton Head)*, Jun. 2014, Hilton Head Island, SC
7. F. Xiong, **Y. Dai**, A. Behnam, E. Pop, "Activation Energy of Carbon Nanotube Joule Breakdown in Variable Oxygen Environments", *Materials Research Society (MRS) Spring Meeting*, Apr. 2014, San Francisco, CA
6. A. Behnam, A. Cappelli, F. Xiong, **Y. Dai**, S. Hong, E. Carrion, A.S. Lyons, E. Piccinini, C. Jacoboni, E. Pop, "Phase Change Memory with Graphene Ribbon Electrodes," *Materials Research Society (MRS) Spring Meeting*, Apr. 2013, San Francisco, CA
5. C.-L. Tsai, F. Xiong, **Y. Dai**, E. Pop, M. Shim, "Ultra-Low Current Switching of AlOx-Based RRAM with Carbon Nanotube Crossbar Electrodes," *Materials Research Society Spring Meeting*, Apr. 2013, San Francisco, CA
4. F. Xiong, M.-H. Bae, **Y. Dai**, A.D. Liao, A. Behnam, E. Carrion, S. Hong, D. Ielmini, E. Pop, "Scaling Towards Fundamental Limits of Phase Change Memory," *IEEE Device Research Conference (DRC)*, Jun. 2012, State College, Pennsylvania, USA
3. E. Pop, F. Xiong, A. Liao, **Y. Dai**, M.-H. Bae, A. Behnam, "Low-Power Phase-Change Memory with Carbon Nanotube Electrodes," *Materials Research Society (MRS)* Spring Meeting, Apr. 2012, San Francisco, CA
2. F. Xiong, M.-H. Bae, A.D. Liao, **Y. Dai**, E. Pop, "Phase-Change Memory Nanowires with Self-Aligned Carbon Nanotube Electrodes," *SRC TECHCON 2011*, Sep. 2011, Austin, Texas, USA (Best paper in session award)
1. F. Xiong, M.-H. Bae, A.D. Liao, **Y. Dai**, E. Pop, "GST Nanowires with Self-aligned Carbon Nanotube Electrodes," *MATERIALS Research Society (MRS) Spring Meeting*, Apr. 2011, San Francisco, California, US

TABLE OF CONTENTS

LIST OF FIGURES

LIST OF TABLES

LIST OF ACRONYMS

ADC	analog-to-digital converter
AOE	advanced oxide etcher
ARC	Animal Research Committee
BLE	Bluetooth low energy
CDC	capacitance-to-digital converter
AMR	anisotropic magnetoresistive
CPU	central processing unit
ETO	ethylene oxide
ERM	Eccentric Rotating Mass
FDRIE	fast deep reactive ion etching
FLS	Fundamentals of Laparoscopic Surgery
FPCB	flexible printed circuit board
FSR	free spectrum range
FTI	flexible tactile imager
GMR	giant magnetoresistive
GPIO	general purpose input/output
HFS	haptic feedback system
HMDS	hexamethyldisilazane
ICP	inductively coupled plasma
IDE	integrated development environment

IRB	Institutional Review Board
I2C	inter-integrated circuit
MEMS	microelectromechanical systems
MIS	minimally invasive surgery
MUX	multiplexer
MR	magnetoresistive
OFET	organic field effect transistor
PCB	printed circuit board
PDMS	polydimethylsiloxane
PE	polyethylene
PECVD	plasma-enhanced chemical vapor deposition
SAGES	Society of American Gastrointestinal Endoscopic Surgeons
SCL	serial clock line
SDA	serial data line
SNR	signal-to-noise ratio
SPI	serial peripheral interface
TMR	tunneling magnetoresistive
UART	universal asynchronous receiver/ transmitter

Chapter 1: Introduction

1.1. Minimally Invasive Surgery

Minimally invasive surgery (MIS) is a type of surgery that is less invasive than traditional open surgery. In open surgery, a surgeon views the field directly from a large incision area and performs surgery with his or her hands or hand-held tools, while in MIS procedures, surgeons look through an endoscope and external monitors into smaller incisions (typically 12-15 mm) to accomplish identical tasks [1]. The prevalence of minimally invasive surgical techniques since the late 1980s has led to great improvements in patient outcomes. The reduced surgical trauma, reduced intraoperative blood loss, alleviated postoperative pain and reduced risk of postoperative infection, shorter hospital stays, decreased pain, and quicker return to the work force have all been touted as great steps forward for surgeons, patients, and healthcare systems [2-6]. MIS is becoming a preferred approach in many domains of surgery including prostatectomy, cholecystectomy, cystectomy, hysterectomy, and nephrectomy [6-8].

There are two types of MIS; one is non-robotic MIS surgery, or called endoscopic/ laparoscopic surgery, and the other is minimally invasive robotic surgery.

1.1.1. Laparoscopic Surgery

Laparoscopic surgery is a minimally invasive surgery that has the surgical area around patient's abdomen. As the laparoscopic skills of today's surgeons have improved, the number of surgical procedures performed laparoscopically have increased [9-12]; however, the limitations related to the counter-intuitive hand-eye-coordination required to perform laparoscopic surgeries, the persistent limitations of the 2D visual modality due to the restricted endoscopic view, the loss

of degrees of freedom in dexterity, the amplification of hand tremors via the rigid instruments, and the loss of tactile feedback remain an impediment to traditional laparoscopic surgeons in a variety of fields [13-18]. The introduction of robotic surgical systems was aimed at alleviating these persistent limitations [19-21].

1.1.2. Robotic Surgery

The introduction of robot-assisted laparoscopic surgery has revolutionized the field of MIS. For conventional MIS the surgeon operates directly on the patient by using an endoscopic interface, whereas for robot-assisted MIS a surgeon employs a surgical robot to operate the surgical instruments on the patient. According to Fortune (in Year *2016*), within five years, *1/3* of U. S. surgeries will be performed with robotic systems [22]. Fig. 1 demonstrates the comparison of the open surgery and robotic surgery. In robotic surgery, the surgeon comfortably works in front of a console while the instruments themselves are moved by specialized robotic arms commanded remotely by the surgeon [7]. The benefits commonly attributed to MIS, such as reduced trauma, faster recovery, apply equally to conventional and robot-assisted MIS.

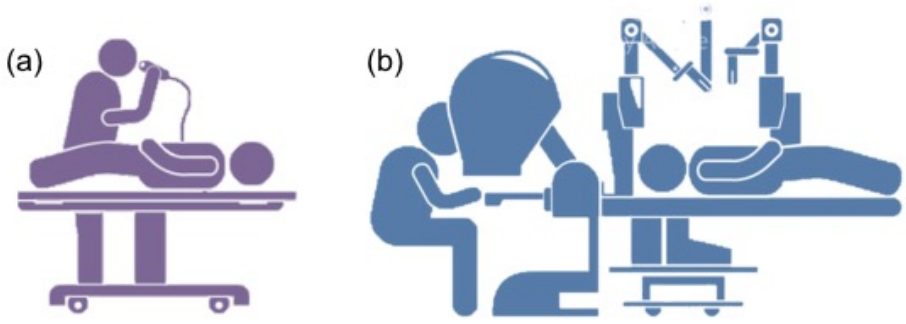

Figure 1 Icons for demonstrating (a) open surgery and (b) robotic surgery. In open surgery, the surgeon performs the surgery directly on the patient while in the robotic surgery, the surgeon is operating a master robot to control a slave robot to perform the surgery indirectly on the patient (reprinted from all-free-download.com)

Figure 2 The da Vinci surgical system[23]

Fig. 2 shows a typical master-slave robot-assisted da Vinci surgical system. The da Vinci Surgical system, which was FDA approved in *2000* [24], is the first and leading commercial instrument, consisting of three major components: the surgical console; the Insite Vision System; and the patient side cart with the robotic arms. The surgical console can be placed anywhere in, or even outside, the operating room. While operating, the surgeon is viewing a stereoscopic image projected in the console and controls the robotic arms with hand manipulators and foot pedals. The position provides an optimal hand-eye alignment. The system provides no haptic (force) feedback, so surgeons must rely on visual feedback. In the Insite Visio System, a three-dimensional high-definition view is created and the viewer provides six-to-ten times magnification of the operation field. Because of the three-dimensional view, the visual feedback is excellent and allows the surgeon to work very precisely. The robotic system has four robotic arms; the EndoWrist instruments are attached to the arms. The wrist has a total of seven degrees of freedom, similar to the human hand, which are three degrees of freedom in translation, *x, y* and *z*, one degree of freedom of grasping, and three degrees of freedom in rotation: yaw, pitch, and roll. The surgeon's hand (fingertip) movements are translated to corresponding movements of the instruments by the

computer. Very precise movements of the robotic instruments are possible because the computer filters out normal physiological hand tremor, avoids the reverse-fulcrum effect, which occurs in traditional laparoscopy, and has the opportunity for motion scaling. In this way, a number of the disadvantages of conventional laparoscopy are eliminated, which results generally in a shorter learning curve for robot-assisted laparoscopy than for conventional laparoscopy. Alongside the surgical advantages are the ergonomic advantages for the surgeon, which reduce the physical complaints associated with conventional laparoscopic surgery [25].

To conclude, the advantages of robotic surgical systems include greater depth perception, increased dexterity, scalability of hand movements and the elimination of physiological tremors and the fulcrum effect [26]. Yet similar to early laparoscopy, the limitations of robotic surgery, including high cost, prolonged surgical times, and loss of tactile feedback, remain barriers to acceptance in many fields. Thus, while the improvements to visualization and intuitive and scalable control have been beneficial, the disadvantages of robotic surgery have relegated the acceptance of the technology to only a few disciplines where these disadvantages are not dire.

The advantages and disadvantages of traditional open surgery, laparoscopic surgery and robot-assisted surgery are summarized in Table 1.

Table 1 Comparison between traditional open surgery, laparoscopic surgery and robotic surgery [21]

	Robot-Assisted Surgery	Conventional Laparoscopic	Open Surgery
Pros	• Reduced trauma • Virtually scar-less • Shorter recovery time • Tremor removal • 3-D visualization • Scaled movements • Tele-surgery	• Reduced trauma • Minimal scarring • Shorter recovery time • Affordable and ubiquitous • Well-developed technology	• Strong hand-eye coordination • Dexterous • Direct contact with patient • Surgeon familiarity • Availability
Cons	• Expensive tooling • Lack of tactile feedback • New technology	• Amplification of tremors • Loss of 3D vision • Compromised dexterity • Lack of tactile feedback	• Scar formation • Long recovery periods • Painful

Table 2 (adapted from [27]) shows the quantitative outcome comparison for da Vinci, laparoscopic surgery and open surgery. From the table, we can see that da Vinci use the shortest operative time, cost the least blood loss, take the shorted average hospital stays, and cause equally least complications among the three.

Table 2 Outcome Comparison: da Vinci vs. Laparoscopy vs. Open Surgery (adapted from [27])

Comparative Data	Da Vinci (n=100)	Laparoscopy (n=100)	Open surgery (n=5875)
Operative time (minutes)	78.7	92.4	86.1
Estimated blood loss (ml)	61.1	113.0	305.1
Complications %	2%	2%	17.2%
Average length of hospital stay (days)	1.1	1.6	6.0

1.2. Tactile Sensation Challenges

Robotic surgical platforms have been in increasing use for a variety of Urological and Gynecological procedures, where the benefits of the robotic system have been shown to outweigh both the health and financial costs [21, 28-30].

However, within general surgery, Gastrointestinal (GI) procedures have been less likely to transition to robotic platforms. This has been attributed to the delicate nature of these procedures that seems to amplify the disadvantage of a loss of tactile feedback. Therefore, the costs of the robotic systems tend to outweigh the benefits. Despite this, several GI procedures have recently been demonstrated using the robotic platform [31] including the Cholecystectomy [32], Bariatric surgery [33-39], bowel resection [40, 41], colectomies [42, 43], and nonresection proctopexy [44]. These comparative studies have revealed that robotic surgeries perform as well as traditional laparoscopy, and at times resulted in decreased procedure time, decreased duration of hospital stay, and more rapid training times [31-42]. An interesting example can be found in the Roux-en-Y Gastric Bypass procedure [33-39].

Robotic bypass procedures have increased in acceptance in recent years. Many studies have shown that the use of the robotic system, for either just the gastrojejunostomy or the full procedure, have resulted in lower complication rates, no gastrointestinal leaks, and no mortality [33-36, 38, 39]. In addition, several studies have revealed more rapid learning curves through means of greater technical precision, greater degrees of freedom, and better visualization using 3 dimensions as compared to laparoscopy [45], reporting numbers of procedures to reach proficiency in the range of 14-30, in contrast to the 75-100 interventions reported for traditional laparascopic gastric bypass [38, 39]. Moreover, the robotic procedure allows hand-sewn anastomoses, in place of stapling, when performing the gastrojejunostomy, which was reported by participating surgeons to be superior and technically easier to perform [37]. Despite this increased acceptance of robotics for the Roux-en-Y Gastric Bypass, there were a few studies that indicated either neutral or negative impacts of the robotic system [37, 44]. Reported complications included substantial jejunal tearing

during manipulation of the alimentary loop, or tears along the gastric pouch [37]. In both of these cases, the surgeons believe that incorporating tactile feedback into the robotics system would have prevented these complications [37, 44]. The haptics technology is to provide the sensation of touch of the patient to the surgeon, which is absent in robotic surgery, as demonstrated in Fig. 3. The gastric bypass surgery seems to be an opportune candidate for incorporation of a haptic feedback system within the existing robotic surgical platform, and will possibly offer a solution to the final hurdle facing widespread acceptance of robotic techniques for this procedure. We hypothesize that robotically performed gastric bypass can reduce operation time and tissue damage compared to traditional laparoscopic Roux-en-Y gastric bypass.

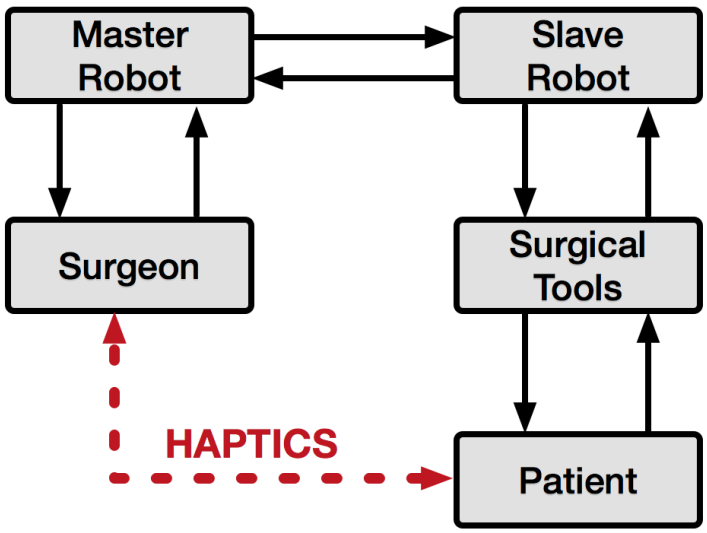

Figure 3 The haptics technology is to let the surgeon regain the sense of touch which is absent in robotic surgery.

Tactile sensation is critical in many delicate surgical procedures, such as tissue manipulation, retraction, dissection, and suturing, to prevent the application of excessive forces. As found in several experimental studies, performing such important tasks without tactile feedback could result in increasing tissue trauma, prolonged operative time, and increased risk of surgical errors. Wagner

et al. found that the absence of tactile feedback increased errors causing tissue damage by a factor of 3 [46]. Also, study showed that the addition of tactile sensation helped compensate for the effect of visual-perceptual mismatch in robotic surgery [47].

This lack of touch sensation negatively influences the outcome of the surgery and is considered a major weakness in current minimally invasive systems [3, 42, 48-52]. To tackle the problem concerning the lack of tactile sensing feedback, various tactile feedback systems have been developed. These systems utilize different sensing mechanisms to detect the forces applied to the tissue by the laparoscopic instruments. Many force sensing technologies have been proposed, including piezoresistive-based [53, 54], piezoelectric-based [55, 56], capacitive-based [57-59], and optical-based [60, 61] sensors. Sensor-integrated instruments have also been designed accordingly such as force sensitive forceps [62, 63], sensorized grippers and graspers [64-67], and sensor-integrated scalpels [68, 69]. However, most sensing solutions were not optimized for surgical environments and were limited in sensing capacity, accuracy, cost, size, sterilizability, biocompatibility, disposability, or long-term stability [70]. For example, piezoresistive sensors have high sensitivity and low noise, but miniaturized multi-axis piezoresistive sensors are difficult to fabricate. Piezoelectric sensors are good for dynamic applications but are inadequate for static sensing due to charge leakage. The details will be shown in Section 2.2.

1.3. The Scope of this Work

A major effort of this thesis is to present the approaches and strategies for structuring an efficient and effective tactile feedback system that has been specifically designed for integration with the existing RMIS tools used in the da-Vinci Surgical robot. The system incorporates a miniature force

sensor that provides tri-axial sensing (normal, shear x, and shear y) from a single sensing element, connected with a specialized IC circuit board for signal processing, has a wireless link to communicate, and a custom user interface to show the real-time data plot and post-experiment data processing. This tri-axial tactile feedback system can provide the surgeons with intelligent, computer aided instructions for manipulating surgical tools, as illustrated in Fig. 4.

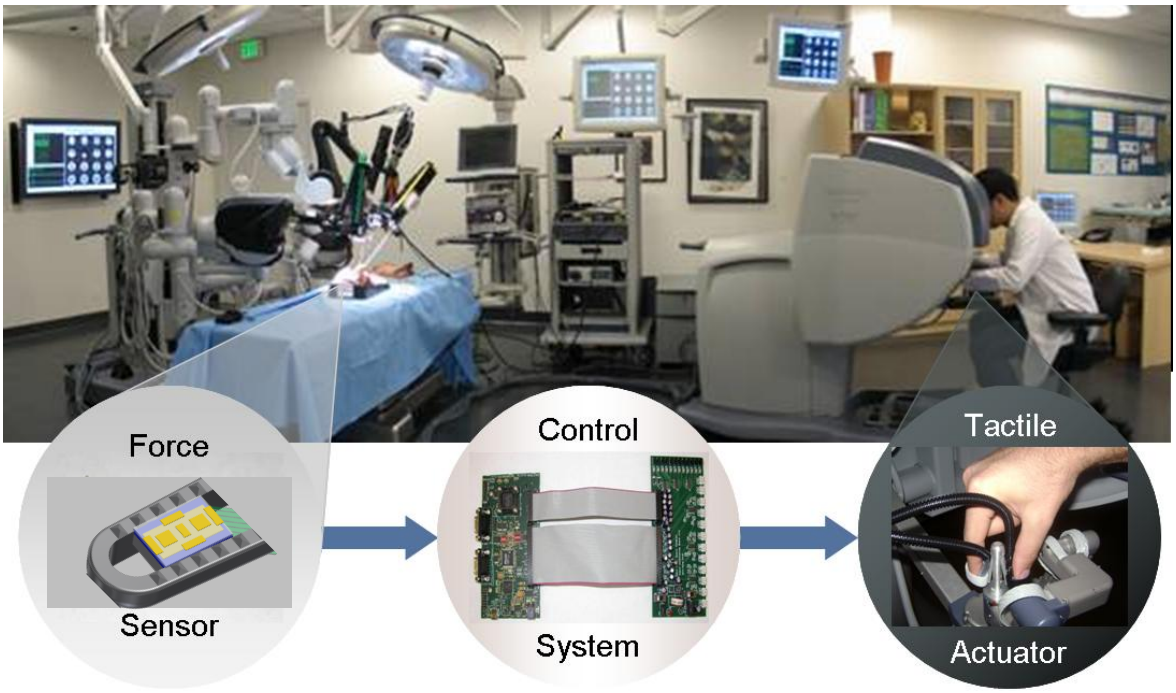

Figure 4 Our solution: we are providing a tri-axial force sensing system to the surgical robot, letting the surgeon regain the sense of touch.

In this work, we first focus on the capacitive tactile feedback sensor design, sensing circuit design, the control system integration, and the integration with the surgical instrument. Then we show the measurements and results for evaluating the tactile system. Finally, we carried out user studies and present the performance results.

1.4. Organization of this Thesis

The structure of the thesis is organized as follows: In Chapter 2, an overview of basic physical principles of sensing technologies, piezoresistive sensors, capacitive sensors, piezoelectric sensors, optical sensors, and magnetic based sensors are provided. This is followed by a discussion of the functional and technical requirements for the tri-axial tactile feedback sensor.

The design and analysis of proposed capacitive sensor models is presented in Chapter 3. We start with a review of state-of-the-art tri-axial capacitive sensor design. Based on the previous discussion, a single-sided capacitive sensor model is proposed along with justification for design choices that were made. Analytical and simulation results are also provided.

This is followed by a discussion about integration of designed capacitive sensor, sensing circuit to the surgical tools in Chapter 4. A first version of the flexible printed circuit board design is showed before we talk about the proposed improved version of 4-layer PCB design. The data analysis is carried out with a LabVIEW program for verification of the functionality of our sensor, and improved noise performance and consistency of the sensor performance are shown. The RMS noise discrepancy for the three directions is discussed.

The integration of the proposed sensing system with the rest of the haptic feedback system (HFS) is accomplished by programming an Arduino based microcontroller shown in Chapter 5. The protocol choice, data transfer techniques, the microcontroller used, and coding flowcharts are discussed.

Chapter 6 show experimental studies for verifying the proposed capacitive tactile feedback system, where the capacitance baseline, noise performance, force calibration, grounding verification and thermal test results are all presented.

Chapter 7 shows several preliminary user studies with normal force feedback and shear force feedback enabled for da Vinci. An extensive knot tying experiment is carried out showing our proposed tactile feedback helps improve the performance of robotic surgery.

Chapter 8 contains conclusions while Chapter 9 talks about the future directions of the work.

Chapter 2: Tactile Sensor Technologies

Humans utilize the five physiological senses— vision, hearing, touch, taste and smell— to perceive outside stimuli from the environment and experience reality. Derived from the Greek word "haptikos", haptics represents the sense of touch and is regarded as the most proficient physiological sense in living organisms [71]. In general, haptic feedback can be divided into two categories: kinesthetic feedback and tactile feedback. Kinesthetic feedback consists of the sensation generated from the sensors in muscles, joints, and tendons, like weight and stretch; while tactile feedback describes feelings on the skin, such as pressure, texture and heat [72].

Research in haptic feedback was originally motivated by telerobots [73] and gained more attention because of the advancement of virtual reality [74]. Various technologies have been utilized to translate the sense of touch, and haptic feedback systems are involved in a wide range of applications. Research teams have been working on a haptic feedback system that allows visitors at a museum to appreciate the artworks in a three-dimensional manner by "touching" the objects [75]. In military applications, haptics technology can be used to simulate battlefield conditions in training and to assist extravehicular space exploration [76, 77]. There is also great interest arising from the entertainment industry. As virtual reality (VR) and holography increase in popularity, haptic feedback helps users become fully immersed in what was once only a visual environment. Last but not least, haptic feedback systems have shown tremendous potential in the surgical and medical environment, especially in robotic surgery. One of the primary application areas for haptics is surgical simulation and medical training [76] [78-80]. More importantly, haptic feedback plays a significant role in improving surgeons' performance in minimally invasive robotic surgery (MIS).

A considerable amount of research has been done on tactile sensor design and fabrication during the last decade. There are many candidates for tactile sensing: resistive sensors, capacitive sensors, inductive sensors, piezoelectric sensors, optical sensors, magnetic sensors, ultrasonic sensors, magnetoelectric sensors, and organic field effect transistor (OFET) sensor. A summary of some of the relevant concepts and specifications in sensing are presented in this section.

As mentioned above, tactile perception plays a crucial role in surgery. However, in conventional minimally invasive surgery, the surgeon's ability to perceive valuable force information through surgical instruments is severely impaired, while in robotic surgery case, it is totally lost.

Studies show that tactile feedback significantly reduced the average applied force and the rate of errors [48, 81-83]. Additionally, more consistent tension was seen applied to suture materials during knot tying [84].

To tackle the problem concerning the lack of tactile sensing feedback (in MIS), various force sensing technologies have been proposed (see Fig. 4 for haptics demonstration) [3, 59, 85, 86], including piezoresistive-based [53, 54, 87], fluidic-based [88, 89], piezoelectric-based [55, 56, 90], capacitive-based [57-59, 91-93], magnetic-based, optical-based [60, 61, 94, 95] sensing *etc*. Sensor-integrated instruments have also been designed accordingly such as force sensitive forceps [1, 62, 63], sensorized grippers [64, 65], sensorized graspers [1, 66, 67, 96], and sensor-integrated scalpels [68, 69].

However, there are limitations in these devices regarding the sensing capacity, accuracy, cost, size, sterilizability, biocompatibility, disposability and long-term stability [3, 70]. For example, commercially available load cells cannot be easily adopted for MIS since they are neither disposable nor easily sterilizable [97]. The piezoresistive sensor has high sensitivity, low noise but its signal drifts as time goes on and is not suitable for MIS. Piezoelectric devices generate electrical signals only in response to a change in the applied force, since under stress free carriers drift toward the dipoles, eventually discharging the devices [98], making piezoelectric sensor good for dynamic application but bad at static sensing. The magnetic sensor is robust but its size is usually too large to be deployed during MIS. These limitations are the reason why they have not yet been introduced in real clinical environments.

2.1. Functional and Technical Requirement

One major challenge for haptics implementation in surgery is the acquisition of haptic information. Strict limits are set in order to meet the requirement of the operating room, including size, robustness, sterilization *etc* [48]. Similar to human tactile sensing, the robotic tactile sensing in the surgery setting should be able to detect both normal and tangential force, detect both dynamic and static force, and have a list of requirement as artificial sensor characteristics including resolution, transfer function, sensitivity, calibration, linearity, hysteresis, accuracy, span or dynamic range, and noise, all of which must meet the requirement set by the clinical usage. Listed below are the definitions and classifications for some of the important characteristics for sense of touch [99].

- Transfer function: the relationship between the input physical input signal and the output electrical signal

- Sensitivity: the ratio of the output signal to the input signal, i.e., the slope of the transfer function
- Linearity: the output signal of the sensor is linearly increasing or decreasing with the change of the input signal
- Hysteresis: sensors do not have the same output value when the input signal return to its original value from a different path from previous
- Accuracy: measured as the maximum discrepancy between the actual value and the ideal value
- Span or dynamic range: two definitions can be used in the sensors. One is the range of the input signal and the other is the ratio of the maximum input signal value to the minimum input signal value, for example, 1000: 1
- Noise: can be divided into two categories, inherent noise within the circuit and interference noise picked up from outside of the circuit
- Resolution: the ratio of the noise to the sensitivity of the sensor
- Response time: amount of time passed between the application of a physical input signal and the resulting indication of that change in the output electrical signal

Common sense lead us thinking that the humidity effect would affect the stability of the sensor, temperature variance would affect the sensitivity of the sensor, and susceptibility to electromagnetic interferences would affect the frequency response of the sensor. In short, the environmental factors affect the sensor characteristics to a large extent and must be considered when choose the sensor design.

Following the previous discussion and pioneers hard work, some basic design criteria can be formulated for tactile sensing in a robotic surgery system [100-102], as addressed in Table 3.

Table 3 Design guidelines for tactile sensing systems

Design Criteria	Guideline
Sensing Surface	Compliant and durable
Force Direction	Both normal and tangential
Spatial Resolution	2 mm
Temporal Variation	Both dynamic and static
Force Sensitivity	0.01N
Dynamic Range	0.01-10 N
Linearity	Monotonic, not necessary linear
Frequency Response	> 100 Hz
Time Response	1 ms
Stability and Repeatability	Good
Robustness	Withstand application defined environment
Hysteresis	Low
Integration and fabrication	Simple, minimal wiring, low power consumption and low cost

2.2. Sensor Types and Basic Working Principles

2.2.1. Piezoresistive sensors

A piezoresistor sensor detects mechanical stress/ strain by a change in resistance of the piezoresistive material itself [103, 104]. As a result, piezoresistive sensor is also called a strain gauge.

The underlying physics of the electrical conductivity σ / resistivity ρ change comes from changing of the effective mass, m^*.

$$\frac{1}{\rho} = \sigma = \frac{qt}{m^*}$$

which is caused by changing of the shape of energy band. In the above expression, q is the elementary charge of an electron and t is the diffusion constant. With *E(k)* being the electron energy of at wavevector *k* in that band, $\hbar$ being the reduced Planck constant,

$$m^* = \frac{\hbar^2}{d^2E(k)/dk^2}$$

rising from the crystal lattice deformation, as a result of applied strain/ stress. In short, the resistivity of a material depends on the internal atom positions and their motions. Strains change these arrangements and, hence, the resistivity.

Now knowing that the resistivity is sensitive to stress, we can write

$$\rho = \rho_{no\ stress} + \Delta\rho(s, \tau)$$

Where s and τ are the normal and shear tensile stress components, respectively.

Writing the Ohms' Law with respect with electric field $\boldsymbol{E}$ and current density $\boldsymbol{J}$ in matrix form:

$$\begin{bmatrix} E_1 \\ E_2 \\ E_3 \end{bmatrix} = \begin{bmatrix} \rho_1 & \rho_6 & \rho_5 \\ \rho_6 & \rho_2 & \rho_4 \\ \rho_5 & \rho_4 & \rho_3 \end{bmatrix} \begin{bmatrix} J_1 \\ J_2 \\ J_3 \end{bmatrix}$$

we have the relationship between the change of resistance $\Delta\rho$ and the applied stress s and strain τ as:

$$\frac{1}{\rho}\begin{bmatrix}\Delta\rho_1\\ \Delta\rho_2\\ \Delta\rho_3\\ \Delta\rho_4\\ \Delta\rho_5\\ \Delta\rho_6\end{bmatrix}=\begin{bmatrix}\pi_{11} & \pi_{12} & \pi_{13} & 0 & 0 & 0\\ \pi_{12} & \pi_{11} & \pi_{12} & 0 & 0 & 0\\ \pi_{12} & \pi_{12} & \pi_{11} & 0 & 0 & 0\\ 0 & 0 & 0 & \pi_{44} & 0 & 0\\ 0 & 0 & 0 & 0 & \pi_{44} & 0\\ 0 & 0 & 0 & 0 & 0 & \pi_{44}\end{bmatrix}\begin{bmatrix}s_1\\ s_2\\ s_3\\ \tau_1\\ \tau_2\\ \tau_3\end{bmatrix}$$

where π_{ij} are piezoresitive coefficients in the longitudinal and transverse direction. To identify the directions, three axes termed 1, 2, and 3 are used, analogous to X, Y, and Z of the classical three dimensional orthogonal set of axes. From the above expression, the corresponding stress can be detected with the change of resistance.

Piezoresistive responses are more significant in semiconductor materials like silicon, germanium, than in metal. However, it should be noted that semiconductor piezoresistive sensors are quite sensitive to temperature variations too. Therefore, temperature-compensating networks must be implemented. Two techniques are commonly used. The first is to apply a reference resistor which is subject to the same temperature but not strain, and the difference will be used to account for the strain effect. The second technique is to connect the gauge to a Wheatstone bridge circuits.

2.2.2. Capacitive sensors

The fundamental structure of a capacitive sensor is of two flat parallel plates with area *A* and distance *d* (Fig. 5)

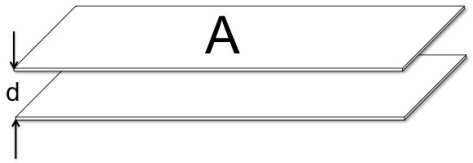

Figure 5 A parallel plate capacitive sensor

When *d* is much smaller than the dimension of the plates, the capacitance equation is valid:

$$C = \frac{\varepsilon_0 \varepsilon_r A}{d}$$

where ε_0 is permittivity of vacuum ($\varepsilon_0 = 8.85\times10^{-12} F/m$), and ε_r is the relative permittivity of the dielectric material in between the plates.

This formula is the key to design capacitive sensor, by establishing the relationship between the capacitance and the plate area, the distance and the relative dielectric constant of the material. Varying either the overlap area or the distance will change the capacitance's value, and changing the dielectric material will change the sensitivity of the sensor. It should be noted that the equation $C = \frac{\varepsilon_0 \varepsilon_r A}{d}$ holds only for parallel capacitor. A change of the geometry will require a modified formula.

Capacitive sensors [91, 105-107] benefit from low cost, easy fabrication, and high sensitivity. However, complex electronics are needed to measure the capacitance and to derive the relative position.

2.2.3. Piezoelectric sensors

Piezoelectric based sensors [108-111] can be treated as force sensitive voltage sources. They convert an applied force or stress (accounting the contacting area) into an electrical potential difference, i.e., voltage, which arises from polarization.

The electric displacement *D* is defined as

$$D \equiv \varepsilon_0 E + P$$

where E is the electric field, P is the polarization density. The polarization density P and the stress is related by the following expression $P = dT$, where d is piezoelectric strain constant, T is stress vector composed of normal stress s and shear stress τ as mentioned in section 2.2.1. Writing the formula in matrix form, we have

$$\begin{bmatrix} D_1 \\ D_2 \\ D_3 \end{bmatrix} = \begin{bmatrix} \varepsilon_{11} & 0 & 0 \\ 0 & \varepsilon_{22} & 0 \\ 0 & 0 & \varepsilon_{33} \end{bmatrix} \begin{bmatrix} E_1 \\ E_2 \\ E_3 \end{bmatrix} + \begin{bmatrix} 0 & 0 & 0 & 0 & d_{15} & 0 \\ 0 & 0 & 0 & d_{24} & 0 & 0 \\ d_{31} & d_{32} & d_{33} & 0 & 0 & 0 \end{bmatrix} \begin{bmatrix} s_1 \\ s_2 \\ s_3 \\ \tau_1 \\ \tau_2 \\ \tau_3 \end{bmatrix}$$

The generated voltage V from piezoelectric material is

$$V = S_v \cdot p \cdot d$$

where

S_v = voltage sensitivity of the material (Volt*meter/ Newton)

p = pressure (Newton/ meter^2) (the scalar quantity of the tensor format stress T)

d = Thickness of the material (meter).

2.2.4. Optical sensors

Several types of optical sensors are on the market and for research, including photoconductive devices [112], photovoltaics [113], photodiodes [114], phototransistors [115], Michelson interferometer [116] *etc*. Among which, Fabry-Perot sensors [117] are used to detect small displacement with high precision, operating with light interference phenomenon.

The cavity with separation d selects which frequencies may oscillate inside the cavity, (q is the mode number and λ is the wavelength of light),

$$d = \frac{\lambda_1}{2} q$$

$$d = \frac{\lambda_2}{2}(q+1)$$

with $= \frac{c}{nv}$, where c is speed of light in vacuum, n is refractive index, we have

$$\nu_1 = q\frac{c}{2nd}$$

$$\nu_2 = (q+1)\frac{c}{2nd}$$

Consequently, we get the free spectrum range (*FSR*) $\Delta\nu = \frac{c}{2nd}$ for the transmitted light spectrum. Whatever may cause change in the cavity separation (mirror movement), may be detected by the change of *FSR*. These include strain, force, pressure, and temperature.

2.2.5. Magnetic sensors

There are many types of magnetic sensors on the market, including anisotropic magnetoresistive (AMR) sensors [118], which are based on spin-orbit scattering; giant magnetoresistive (GMR) sensors [119], which are based on spin accumulation; tunneling magnetoresistive (TMR) sensors [120], which are based on dependent tunneling effect *etc*. Among which, magnetism based tactile sensors measure the change in flux density as a result of the applied force. The flux measurement can be made either by utilizing Hall effect [121, 122] or magnetoresistive (MR) [123] effect. The underlying working principle of which is Lorentz force. The above-mentioned AMR, GMR, and TMR sensors all detect magnetic field, while Hall effect sensors and MR sensors detect the secondary field as magnetic flux density.

2.3. Comparison of Different Sensor Types

Now we have enough information to compare each of the sensor types mentioned in Chapter 2.2. in terms of the specifications for tactile sensing. A summary of the comparison is listed below.

Table 4 Comparison of the reviewed sensing techniques [102, 124]

Sensor Type	Merits	Demerits
Piezoresistive (strain gauge)	1. High sensitivity 2. Low cost 3. Low noise 4. Simple electronics 5. High spatial resolution 6. 3D force sensing possible	1. Stiff and fragile 2. Non-linear response 3. Hysteresis 4. High temperature dependence 5. Signal drift (low repeatability) 6. Relatively costly materials and fabrication techniques
Piezoelectric	1. High sensitivity 2. Well suited for dynamic applications 3. High bandwidth 4. Robust and chemically resistant	1. Temperature sensitive 2. Lacks robust electrical connections 3. Decay of static response (poor static sensing) 4. Not stretchable
Capacitive	1. Sensitive 2. Low cost (simple fab) 3. Suitable for static and dynamic signal 4. Temperature independent 5. Small sizes and high spatial resolution possible 6. 3D force sensing possible	1. Cross-talk between sensor elements (noise) 2. Hysteresis 3. Relative complex circuitry 4. Parasitic capacitances 5. Sensitive to electromagnetic interference
Magnetic	1. High sensitivity 2. Good dynamic range 3. Robust 4. No mechanical hysteresis	1. Restricted to non-magnetic medium 2. Complex computations 3. Somewhat bulky 4. High power consumption
Optical-based	1. Good sensing range 2. Reliable/ repeatable	1. Bulky 2. Non-conformal

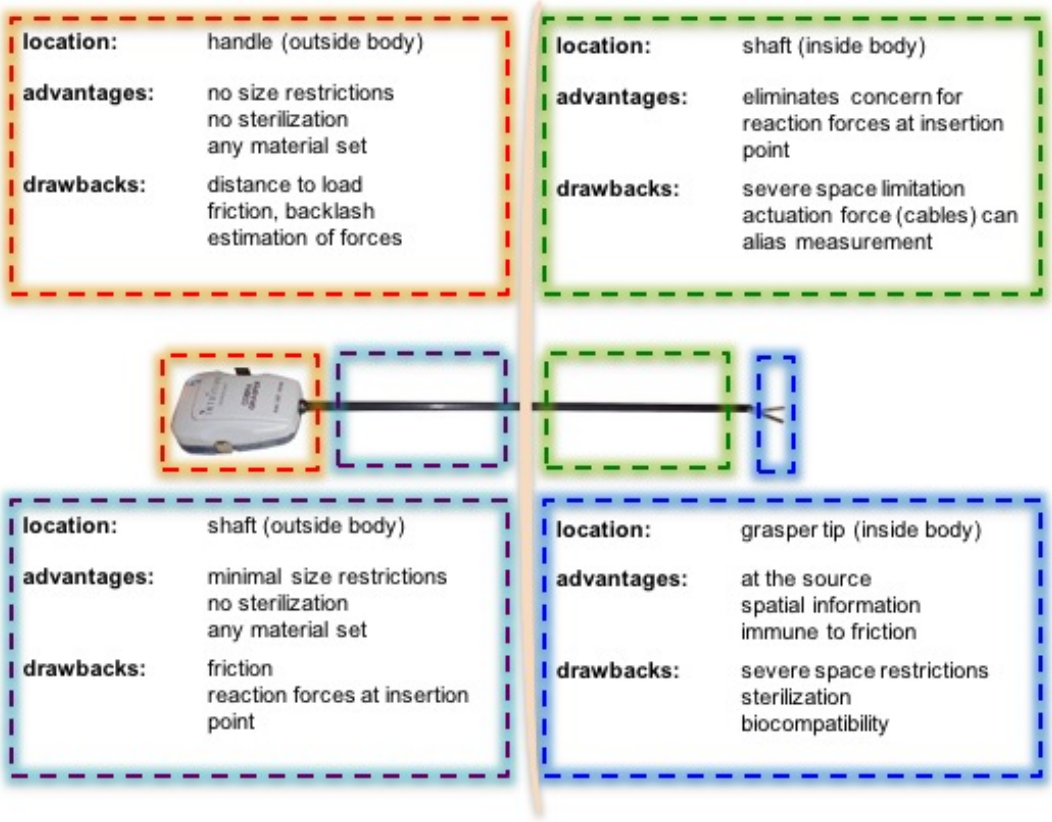

Figure 6 Comparison of tactile sensing on different locations of a surgical grasper. Locations include handle (outside body when doing a surgery), shaft (outside the body), shaft (inside the body) and the grasper tip (inside the body). Each of the location has advantages and drawbacks (detailed in the figure)

Fig. 6 shows the comparison of the advantages and drawbacks of locate the tactile sensing on different parts on a surgical grasper. While putting the tactile sensing on the grasper tip gives us disadvantages as severe space restrictions, sterilization problem, and biocompability concern, we are benefiting from the best accuracy we can get since it is at the source of applied force and it is immune to friction.

From Table 4, we can see that optical-based sensors and magnetic sensor cannot be used in this case, since currently available devices are too bulky for our surgical grasper tip. Piezoresistive sensors have the issue of high temperature dependence, while most piezoelectric sensors lack the

ability of sensing static force. Although capacitive sensors are susceptible to noise and parasitic capacitance, and the need of a complex readout circuit, those issues can be solved by using a capacitance to digital converter (CDC) and differential design.

3.1. Triaxial Capacitive Sensing Design Insights

There are several surgical robotic systems with tactile feedback capabilities [125-127], however, all of them are in research prototype. The da Vinci surgical system is the only general RMIS system available in the market (as of 2018). Because of its commercial nature, there is no way to modify the existing system, including the surgical instruments that we would like to integrate our haptic feedback system with. This alone puts strict limits on the size and circuit wiring.

There are groups working on mounting tactile feedback system with the da Vinci surgical system, but so far, only uniaxial feedback system has been developed [82, 84, 128, 129](as of 2018).

Our group is trying to develop a triaxial capacitive sensing system with the da Vinci system.

3.1.1. Triaxial capacitive sensors

Cheng *et al* [130] presents a polymer-based three- axial capacitive sensing array which is realized by micromachining and flexible printed circuit board (PCB) technique. This design is capable of sensing both normal and shear force.

Dobrzynska *et al* [131] developed a flexible-substrate-based three-axial force sensor. This sensor design is comprised of finger-shaped capacitive electrodes and the three layer of polymeric packaging (polymide, parylene-C, and polydimethylsiloxane) makes the proposed sensor fully flexible and elastic.

Surapaneni *et al* [132] designed a flexible tactile imager (FTI) which utilizing microelectromechanical systems (MEMS) and FPCB techniques, comprising a flexible array of normal and shear stress sensors. The normal stress is measured by the net capacitance of the cell and the shear stress is calculated by the overlap difference of the floating electrodes with respect to the bottom electrodes. One thing to notice is that they made use of the floating electrodes for simplifying the circuit.

Brookhu *et al* [133] have fabricated a silicon force–torque sensor which consists two parts can detect both normal and shear stress. The top part consists of equally distributed silicon pillars and the bottom part consists of electrodes for capacitive read-out. The normal force can be detected by a change in the gap from the compression of the silicon pillars and the shear force can be determined by the sideways bending of the silicon pillar. The comb structures enable the measurement of shear force as well as all the torque components.

3. 1. 2. Design insights of capacitive sensor

It is important to quantify various signal and noise parameters associated with any system in order to evaluate its performance and reliability. Any unwanted change in the signal, whether from devices operating in its vicinity or environmental changes, can be termed as noise. When measuring a change in capacitance of the order of femto Farads, a small amount of noise can also lead to spurious detections. Before going into the techniques of how to build a system where the effect of noise is minimal, it is important to understand the possible sources of noise.

A capacitive sensing system is mainly susceptible to noise generated from the following three sources:

a. Radiated noise

Any operating circuitry radiates energy that can potentially create problems with the operation of other circuits in its vicinity. Capacitive sensing buttons constitute only the user interface part of any system, and generally there is much circuitry sitting behind the user interface. This nearby circuitry can also radiate noise if not properly designed. Sources of noise can be the LCD (Liquid Crystal Display), switching power supplies, mobile phone, Wi-Fi radio, etc.

b. Conducted noise

A noisy power supply is the most common source of conducted noise. The increasing demand of low cost implementations forces developers to use less expensive supplies which in turn generate more noise. This can adversely affect the operation of the sensor. A human body touching the sensor can also couple a 50/60Hz common mode noise into the system.

c. Environmental noise

Changes in environmental parameters such as humidity, temperature, and device aging also change the capacitance of the sensor. Such unwanted changes can also be termed as noise.

There are multiple techniques for achieving a good signal-to-noise ratio (SNR). Including tuning, auto correction, software filters, and a proper schematic and PCB layout can address most of the problems mentioned above. A tuning method is to calibrate the device during the design phase to ensure that it exhibits a minimum of *5:1* SNR for fail-safe operation. By using some software coding overhead, this manual tuning effort can be switched to auto-tuning where the device can calibrate itself to ensure that it achieves the minimum SNR required. An auto correction method is to compensate the gradual changes in capacitance due to temperature, humidity, or component aging by monitoring the counts abstained in firmware and updating with the gradual change

observed. Software filters can also improve the SNR by processing the digital counts obtained with the cost of an increased response time.

However, our first insight from literature review is to design a differential capacitive sensor, which is widely employed for the measurement of linear and angular displacement, pressure, and acceleration. The differential design benefits from its compensation of common mode noise or errors, which can include tilting, temperature variation, some sources of electrical noise, humidity, and pressure.

A typical differential capacitive sensor is made of two capacitors, C_1 and C_2, the change of the input physical signal will cause one capacitance (C_1) to increase and the other capacitance to decrease (C_2), also known as push-pull capacitive sensors. For a simple parallel capacitor,

$$C_0 = \frac{\varepsilon_0 \varepsilon_r A}{d}$$

If the parameter that changes with the physical quantity being sensed is either the area A or the relative permittivity ε_r, then

$$C_1 = C_0(1 + kx)$$

and

$$C_2 = C_0(1 - kx)$$

The difference is what we care about

$$\Delta C = C_1 - C_2 = 2C_0 kx$$

as well as the ratio

$$\frac{C_1}{C_2} = \frac{1 + kx}{1 - kx} = 1 + \frac{2kx}{1 - kx} \approx 1 + 2kx$$

where ΔC is the nominal value of sensor capacitance C_1 and C_2, k is the transformation constant of the sensor and x is the physical quantity being sensed.

From the equations, it is clear that the variances of temperature, pressure effect to dielectric material can be compensated by ratiometric measurement.

And the second design insight is to use unconnected floating electrodes as proposed in [132] with the benefit of eliminating the need for patterning electrical wiring and thus simplifying the design and ultimately making the integration easier.

Two sensor designs would be described in the following section 3.2 and section 3.2, the first one is a joystick model, and the second is a single-sided sensor model. Both of them have a triaxial sensing capability, with the differential design for the shear-x and shear-y directions, while, the single-sided model utilizes the floating electrode design to eliminate the need for complex wiring, leaving a pristine surface for surgical tasks.

3.2. Joystick Model

3.2.1. Schematic of joystick design

The joystick capacitive sensor is designed as this: we have the PDMS as the elastic material embedded between two layers of Au conducting plates, forming the capacitor. The area insides red line is the bottom plate, while the area insides the grey dotted line is the top plate (Fig. 7). The top plate possesses five parts, the center square plate, and the surrounded four trapezoids working as differential shear force detectors. The working principle is as follows: any force can be divided into three directions, *x, y, z* with z direction force be normal force, and *x, y* direction force be shear

force. After applying a force, we will have displacement in x and y direction and decrease distance between the top and bottom plates because of the normal force. All of these make the capacitances change as indicated by Fig. 7 (*b*).

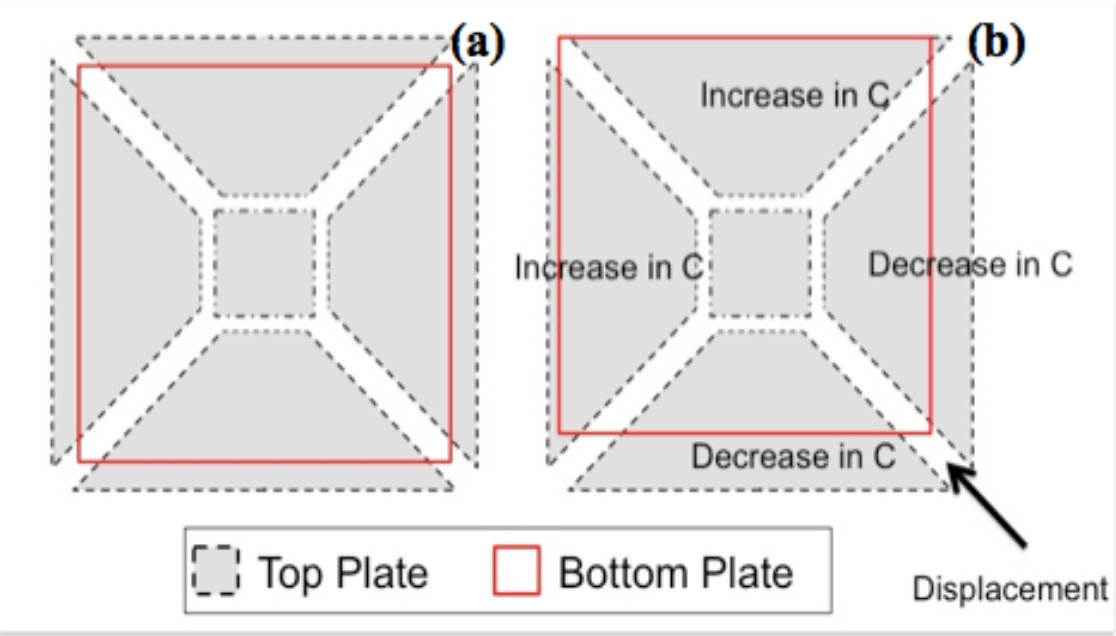

Figure 7 Working principle of joystick model. The center plate can detect normal force while the surrounded four parts of electrodes are capable of sensing shear force.

The schematic drawing for the trapezoid is plotted in Fig. 8, where x_0 is the original overlap distance with the underlying square, S_0 and S_2 are the designed length of the trapezoid and h is the height of the trapezoid.

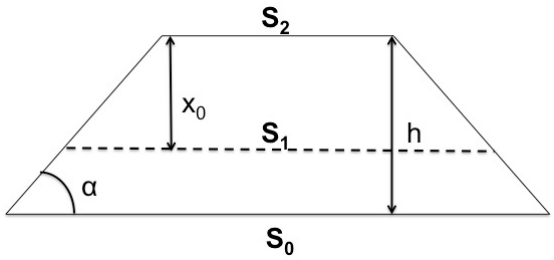

Figure 8 Schematic drawing for one trapezoid in the capacitive sensor design

3.2.2. Sensitivity calculation

S_0, S_1, and S_2 have the relationship:

$$S_0 = S_2 + 2h\cot\alpha \Rightarrow S_2 = S_0 - 2h\cot\alpha$$
$$S_1 = S_2 + 2x_0\cot\alpha \Rightarrow S_1 = S_0 - 2(h - x_0)\cot\alpha$$

the overlap area is

$$A_{overlap} = \frac{1}{2}(S_1 + S_2)x_0 = (S_0 - 2h\cot\alpha)x_0 + (\cot\alpha)x_0^2$$

then we can calculated sensitivity *dc/dx* as

$$\frac{dc}{dx} = \frac{2\varepsilon}{d}\left[S_0 - 2\cot\alpha(h - x_0)\right]$$

Plotting the sensitivity with respect to the designing angle α (see Appendix A for python code)

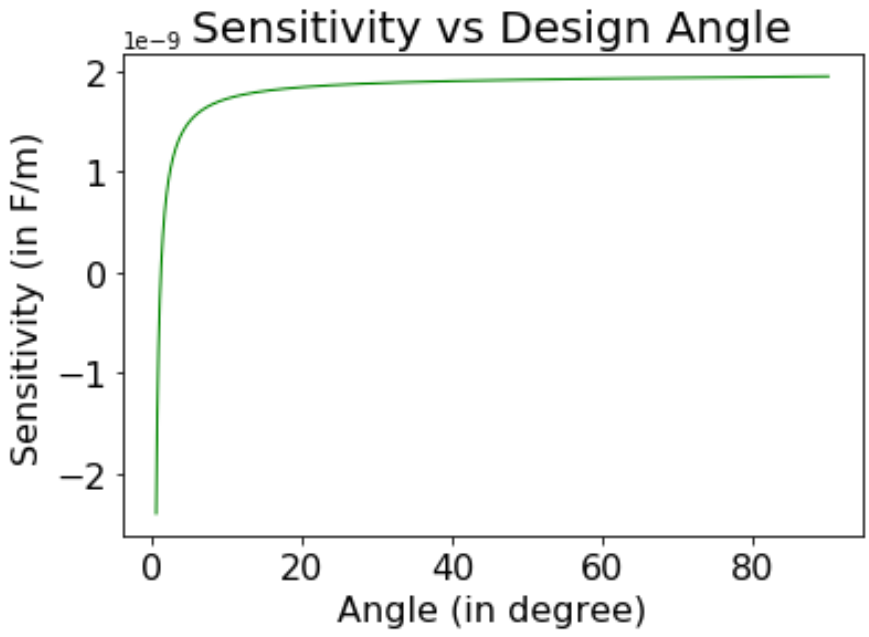

Figure 9 Sensitivity dc/dx with respect to different angle (in degree)

The values show that when the angle is 90 degrees, *dc/dx= 4.87 aF/um*, and when the angle is *45 degrees, dc/dx= 4.77 aF /um*. It is easy to see from both the plot and the values that the sensitivity

does not change much from angle 45 degrees to 90 degrees, varies only *0.1 aF/um* (*1aF= 1E-15 Farad*). It is reasonable to design the trapezoid with angle 45 degrees for simplicity.

Now the simplified sensitivity *dc/dx* is

$$\frac{dc}{dx} = \frac{2\varepsilon}{d}\left[S_0 - 2(h - x_0)\right]$$

The design insight is thus to make overlap x_0 close to the height h.

$$A_1 = a^2$$
$$A_{2,3,4,5} = \left(S_0 - 2h\right)x_0 + x_0^2$$

Looking at the geometry in Fig. 10, naming the center electrode as C_1, the y-direction electrodes as C_2 and C_4, the x-direction electrodes as C_3 and C_5.

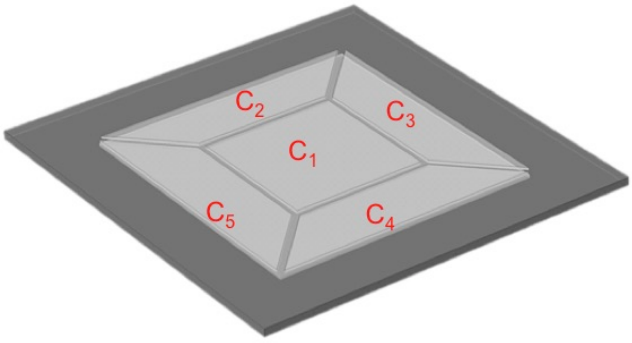

Figure 10 Geometry of the top layer of the joystick model

3.2.2.1. normal force only

For the simulation of the sensor's behavior upon applied load, we assumed a simplified linear elastic stress-strain model. When normal compressive stress F_N is applied to the sensor, the polymer dielectric compresses and the initial distance between the electrodes decreases by Δd, and the Young's modulus E of the polymeric material between the electrodes can be written as

$$E = \frac{F_N / A}{\Delta d / d}$$

where A is the area on which the normal force is applied.

Then we can have the compressed distance d as

$$d' = d - \triangle d = d(1 - \frac{F_N}{AE})$$

$$C = \varepsilon_0 \varepsilon_r \frac{A}{d'} = \varepsilon_0 \varepsilon_r \frac{A}{d}(1 + \frac{F_N}{AE}) \text{ if } \frac{F_N}{AE} \ll 1$$

3.2.2.1. shear force only

We simplify the shear force in positive x direction, and only cause the area of capacitor 3 and capacitor 5 changes:

$$A_5' = (S_0 - 2h)(x_0 + x') + (x_0 + x')^2$$
$$A_3' = (S_0 - 2h)(x_0 - x') + (x_0 - x')^2$$

$$C = \varepsilon_0 \varepsilon_r \frac{A_{3,5}'}{d}$$

By the same token, if we have positive y-direction force, simply change the A_3 and A_5 to be A_2 and A_4.

3.2.2.3. coupling of both normal and shear force

It is easy to understand that the center square capacitor C_1 and the top and bottom capacitor C_2 and C_4 only influenced by F_N, the value of these capacitors are as follows:

$$C_1 = \varepsilon_0 \varepsilon_r \frac{A_1}{d'} = \varepsilon_0 \varepsilon_r \frac{a^2}{d}(1 + \frac{F_N}{A_1 E}) = \varepsilon_0 \varepsilon_r \frac{a^2}{d} + \frac{\varepsilon_0 \varepsilon_r}{dE} F_N$$
$$C_2 = C_4 = \varepsilon_0 \varepsilon_r \frac{A_2}{d}(1 + \frac{F_N}{A_{trap} E}) = \varepsilon_0 \varepsilon_r \frac{A_2}{d} + \frac{\varepsilon_0 \varepsilon_r}{dE} \frac{A_2}{A_{trap}} F_N$$

the sensitivities are

$$\frac{dC_2}{dF_N} = 2.3pF/N$$
$$\frac{dC_1}{dF_N} = 2.43pF/N$$

while C_3 and C_5 are influenced by both F_N and F_s, the capacitance are:

$$C_3 = \frac{\varepsilon}{d}\left[x_0^2 + (S_0 - 2h)x_0\right] + \frac{\varepsilon}{dE}F_N - \frac{\varepsilon(S_0 - 2h)}{A_{grasper}G}F_s + \frac{\varepsilon(S_0 - 2h)}{A_{grasper}^2 EG}F_s F_N$$
$$C_5 = \frac{\varepsilon}{d}\left[x_0^2 + (S_0 - 2h)x_0\right] + \frac{\varepsilon}{dE}F_N + \frac{\varepsilon(S_0 - 2h)}{A_{grasper}G}F_s - \frac{\varepsilon(S_0 - 2h)}{A_{grasper}^2 EG}F_s F_N$$

Initial Cap Constant	Normal Force Only	Shear Force Only	Coupling Component

Here we use ε to replace $\varepsilon_0\varepsilon_r$, the differential capacitance is thus

$$C_5 - C_3 = 2\frac{\varepsilon(S_0 - 2h)}{A_{grasper}G}F_s - 2\frac{\varepsilon(S_0 - 2h)}{A_{grasper}^2 EG}F_s F_N$$

Gives us both the direction (either the C_5-C_3 is positive or negative) and the amplitude. As a result, the shear force sensitivity is

$$\frac{dC}{dF_S} = 2\frac{\varepsilon(S_0 - 2h)}{A_{grasper}G} = 3.6fF/N$$

For the above calculation, F_s is by nature F_x. Any force can be divided into three directions, *x, y,* and *z*. For example, the above calculation for *x*- direction capacitances C_3 and C_5 were only considered influenced by normal force and *x*- direction force, not *y*- direction force. However, by considering both *x* and *y*- direction force, there is an additional displacement in y, causing no change in C_3 and C_5. In conclusion, the calculation above can be applied to any case.

3.2.3. Optimal design parameters

Figure 11(*a*) shows the change of capacitance with normal force with different materials: polydimethylsiloxane (PDMS), silicon dioxide, silicon nitride, polyimide, parylene C, and polyethylene. From the plot, we can notice the sensitivity (*dC/dF*) varies 5 orders of magnitude, with PDMS 2 orders more sensitive than the second silicon dioxide. The large difference comes from Young's modulus of each material. Detailed explanation will be given in section 3.3. We pick PDMS to be the dielectric material as a result.

Fig. 11(*b*) shows the capacitance change linearly with electrode dimensions a, which is the size of the center electrode shown in Fig. 10. With larger electrode dimension, we can have more sensitive sensor, unfortunately, the grasper size limits. For a typical grasper tip used in robotic surgery, its size is *2 mm* by *10 mm*. Making the electrode dimension a *500 um* to be the optimal parameter we use.

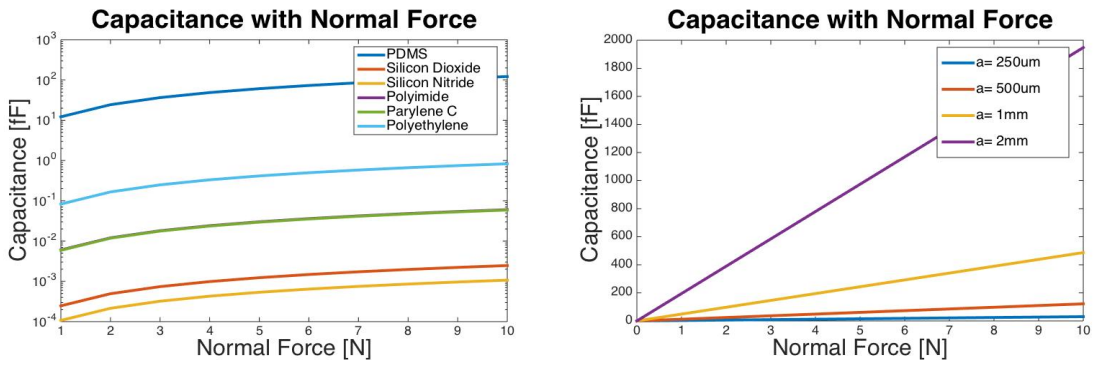

Figure 11 Change of capacitance with compression force 0-10N for (a) different materials, (b) different electrode dimensions with PDMS as the dielectric.

Similarly, Fig. 12 (*a*) shows the change of capacitance with shear force (shear sensitivity) for different materials, (*b*) shows the shear capacitance with different electrode dimensions. The conclusion is the same as for normal force: use PDMS as the dielectric material and the designed parameter value is *a= 500 um*.

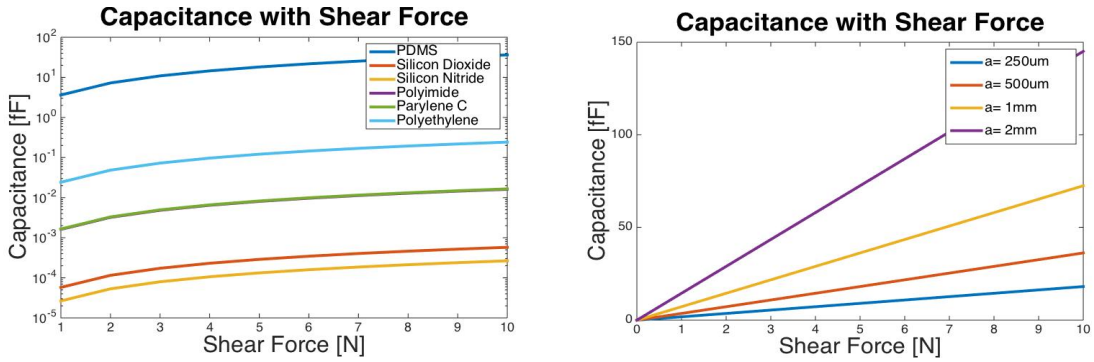

Figure 12 Change of capacitance with shear force 0-10N for (a) different materials, (b) different electrode dimensions with PDMS as the dielectric.

3.2.4. Fabrication process

The fabrication process is detailed in Fig. 13.

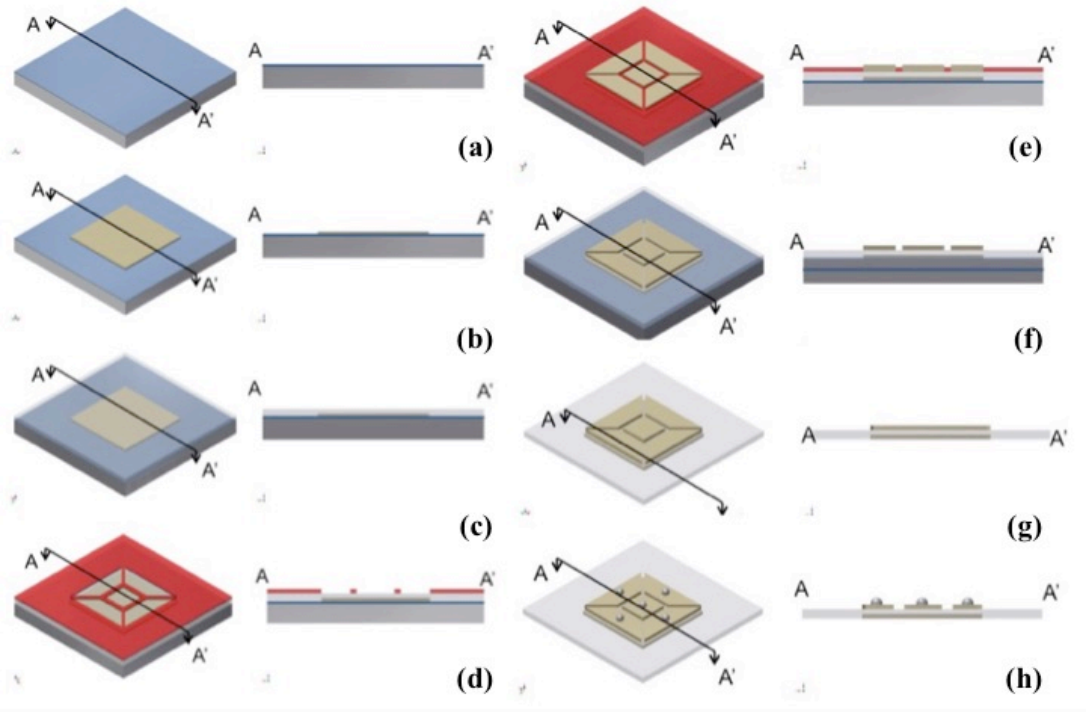

Figure 13 Fabrication process of making joystick model capacitive sensor

Step 1: starting with a silicon substrate, and Plasma-enhanced chemical vapor deposition (PECVD) *5 um* oxide (SiO_2)(*a*). The front side oxide will act as etch stop for the Fast Deep Reactive Ion Etching (FDRIE) step while the backside oxide will act as insulating layer for the plating step.

Step 2: using e-beam evaporator CHA to deposit a Ti/Cu/Ti seed layer, and then we can electroplate a *5 um* Au layer (*b*). This step is designed to create a bondable surface for assembly and back-end processing. The bottom *20-nm* Ti layer works as the adhesion layer, while the top *1.5-um* Ti layer serves as a mechanical robust, biocompatible electrode. The Au layer is used to be bonded as a biocompatible electrode.

Step 3: spin coating a *25-um* PDMS layer (c). The recipe is under examination so far, but ideally, we spin on a *5-mL 5:1* ratio PDMS, with spinning condition as: *500 rpm* at *100 rpm/s* for *5* seconds, and then *2000 rpm* at *300 rpm/s* for *30 seconds*, and finally *25 rpm* at *100 rpm/s* for *15 seconds* to stop. We can use the Q-tip with acetone to remove the edge bead.

Step 4: lithographically defining top plate (*d*). As a standard routine, we put the wafer in hexamethyldisilazane (HMDS) for *10 minutes* before spin on the negative photoresist KMPR 1005. The recipe is *500 rpm* at *100 rpm/s* for *5 seconds*, *2000 rpm* at *300 rpm/s* for *30 seconds* and *25 rpm* at *100 rpm/s* for *15 seconds*. Next, soft bake on the hotplates for *5 minutes* at *100 degree*. After exposure and post bake at *100 degree* for *2 minutes*, we use the negative photoresist SU-8 to develop for *2 minutes* and *30 seconds* with strong agitation.

Step 5: electroplate another *5-um* Au layer (*e*).

Step 6: striping the plating mold and the seed layer (*f*).

Step 7: removing the substrate by grinding to the silicon dioxide layer, and then use Hydrogen Fluoride (HF) to etch away remaining SiO_2.

Step 8: after dicing the wafer, we can flipchip and solderbump to the flexible printed circuit board (FPCB).

3.3. Single-sided Sensor Model

3.3.1. Schematic of single-sided sensor design

We present a tri-axial high-resolution cost-effective capacitive sensor with simple structure, minimal wiring, and low power consumption.

In our design, the normal and the shear sensing capability is realized through the top electrodes of the sensor which is patterned as seven separate elements. The compressive load results in reduction in the dielectric thickness, and shear force is detected by a change in the overlap area of the four differential electrodes on the sensor sides when its surface is shifted laterally. As discussed previously, differential capacitance operation principle yields a high-precision measurement for capacitive sensors with increased signal-to-noise immunity. This differential design minimizes errors caused by parasitic capacitance and stray capacitance of the sensor pads as mentioned as the demerits for capacitive sensor in Table 4. In summary, our single-sided model is based on differential capacitive measurement for the benefit of tilt compensation and temperature, humidity, and pressure variance tolerance.

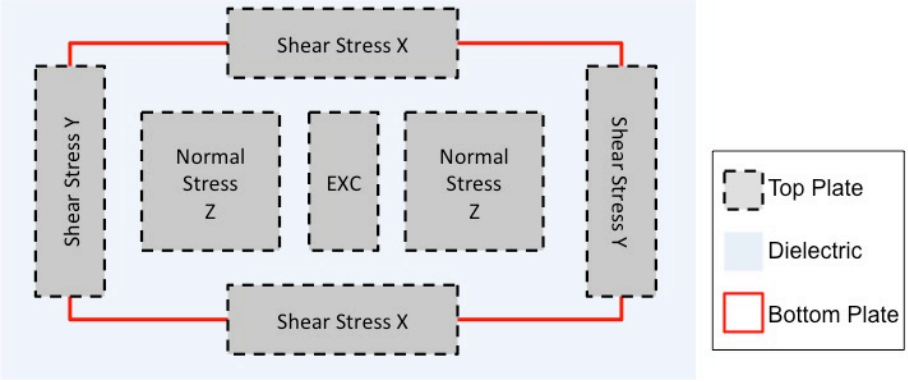

Figure 14 Schematic for single-sided capacitive sensor

The single-sided capacitive sensor is designed for easier integration with the surgical system. The sensor schematic design is described in Fig. 14: we have the polydimethylsiloxane (PDMS) as the elastic dielectric material embedded between two layers of gold (Au) conducting plates, forming the capacitance. The area insides red line is the bottom plate, while the area insides the grey dotted line is the top plate. The top plate consists of seven parts, the center plate for excitation single input, and the surrounding four rectangular plates working as differential shear force detectors. The two square plates are used for normal stress testing.

The key component of our material design is the micro-structuring of thin film of the dielectric elastomer PDMS. PDMS is well known for it good elastic properties, and its biomedical compliance with human tissue [134] and living cells [135]. This material also allows us to achieve sufficient resolution while providing a high dynamic range from theoretical calculation. And the sensing range and resolution can easily be customized by changing the PDMS—"softer" PDMS enable high force resolution sacrificing range and vice versa.

The working principle is as follows (Fig. 15):

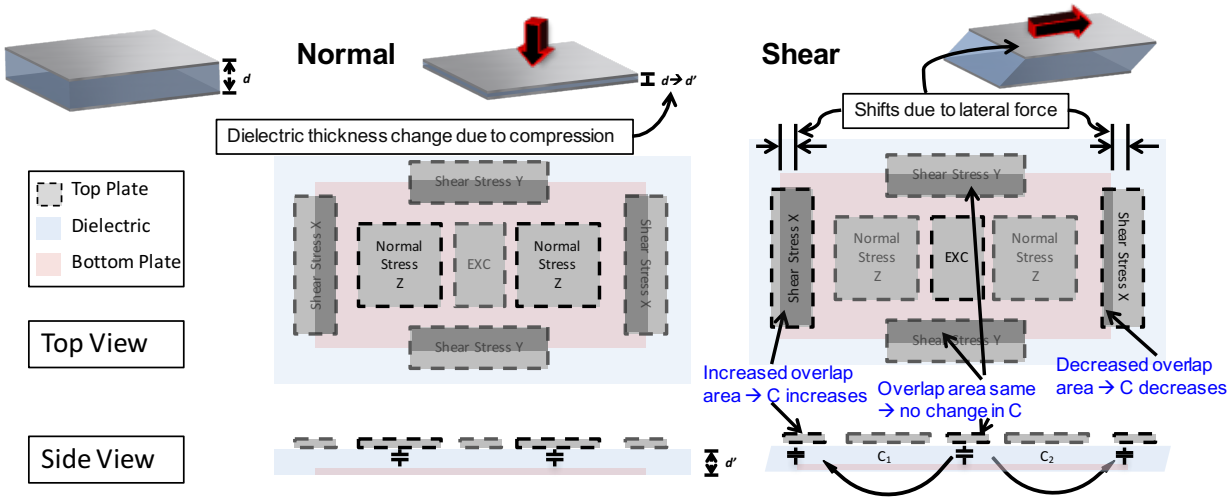

Figure 15 Working principle for single-sided capacitive sensor

1. Vertical displacement causes changes in the dialectic elastomer's thickness *d*, which alters the capacitance value. Since the applied force is directly related to displacement, changes in the capacitance enable the applied force to be computed.

2. When the horizontal force is applied to the sensor surface, changes in the overlapping area as presented in Fig. 15 causes the change in capacitance.

3.3.2. Sensitivity calculation

3.3.2.1. normal force

Vertical displacement causes changes in the dielectric elastomer's thickness *d*, which alters the capacitance value. Since the applied force is directly related to displacement, changes in the capacitance enable the applied force to be computed.

Figure 16 shows how capacitance will change with normal force. The two capacitors corresponding to the normal force are linked in series. $C_z = \frac{C_1 C_2}{C_1 + C_2}$, with the square plate area being

S^2 and the compressed distance being d', $C_1 = C_2 = \frac{\epsilon_0 \epsilon_r S^2}{d'}$, leading to $C_z = \frac{\epsilon_0 \epsilon_r S^2}{2d'}$, where $\epsilon_0 = 8.854\times10^{-12}\ F/m$ is the free space permittivity and $\epsilon_r = 2.75$ is the relative permittivity of the PDMS.

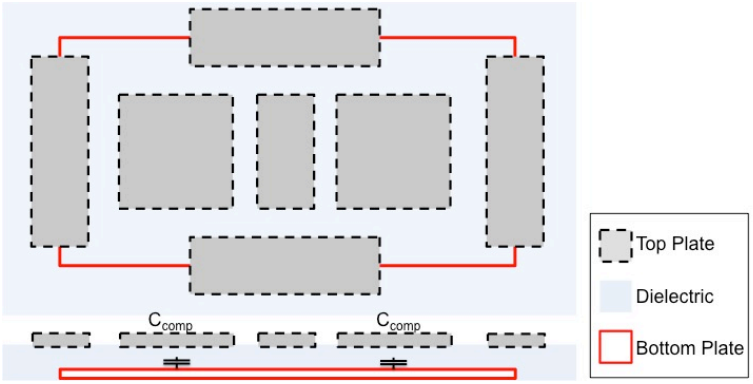

Figure 16 Illustration of how capacitance change with normal force

Normal stress $\sigma = \frac{F_{normal}}{A}$ where A is the area of the sensor over which force F_{normal} is applied. The normal stress relates to normal strain ε by $\sigma = E\varepsilon$, where E is the Young's modulus *10 MPa* in our case, and strain $\varepsilon = \frac{d-d'}{d} = 1 - \frac{d'}{d}$. Re-arrange the equations, we have the relation $d' = d(1 - \frac{F_{normal}}{AE})$. For the case where the sensor width is *3 mm*, and the sensor length is *6 mm*, we have *A= 18 mm*^{2}.

Combining equations, we obtain the relationship between the normal force and the capacitance: $C_z = \frac{\epsilon_0 \epsilon_r S^2}{2d(1-\frac{F_{normal}}{AE})}$, or $F_{normal} = AE(1 - \frac{\epsilon_0 \epsilon_r S^2}{2dC_z})$. When $F_{normal} \ll AE = 180\ N$ (with *A=18 mm*^{2}, *E=10 MPa*), then $C_z \cong \frac{\epsilon_0 \epsilon_r S^2}{2d}(1 + \frac{F_{normal}}{AE})$ and $F_{normal} \cong AE(\frac{2dC_z}{\epsilon_0 \epsilon_r S^2} - 1)$.

Often it is useful to consider the baseline capacitance C_0 (under no compression): $C_0 = \frac{\epsilon_0 \epsilon_r S^2}{2d}$. Normal sensitivity is changing with the compression force as $\frac{dC_z}{dF_{normal}} = \frac{C_0/AE}{(1-F_{normal}/AE)^2}$. The resolution (noise/ sensitivity) is changing for normal force due to the nonlinearity of the system, but we will approximate the resolution at the point of zero applied force. For our system, the expected normal force sensitivity is: $\frac{dC_z}{dF_{normal}} = \frac{\epsilon_0 \epsilon_r S^2/2d}{AE(1-F_{normal}/AE)^2} \cong 20\ fF/N$

3.3.2.2. shear force only

Capacitance change with an applied shear force is demonstrated in Fig. 17. When a horizontal force is applied to the sensor surface, changes in the overlapping area cause a change in capacitance. As an example, consider applying the force in a horizontal direction to the right. We will get an increase in capacitance from the left capacitor because of increased overlap area, and decrease in capacitance from the right capacitor because of decreased overlap area, while the center capacitance remains the same due to unchanged overlap area. As mentioned, the electrodes corresponding to the shear force are used for excitation signal input and differential capacitance input. We will use *CIN(±)* to describe the differential electrodes and *EXC* to describe the excitation electrode, which is used by the capacitive measurement circuit for differential measurement.

Since there is no compression, *d'= d*, the original distance between top and bottom plates (i.e., the PDMS thickness) is unchanged.

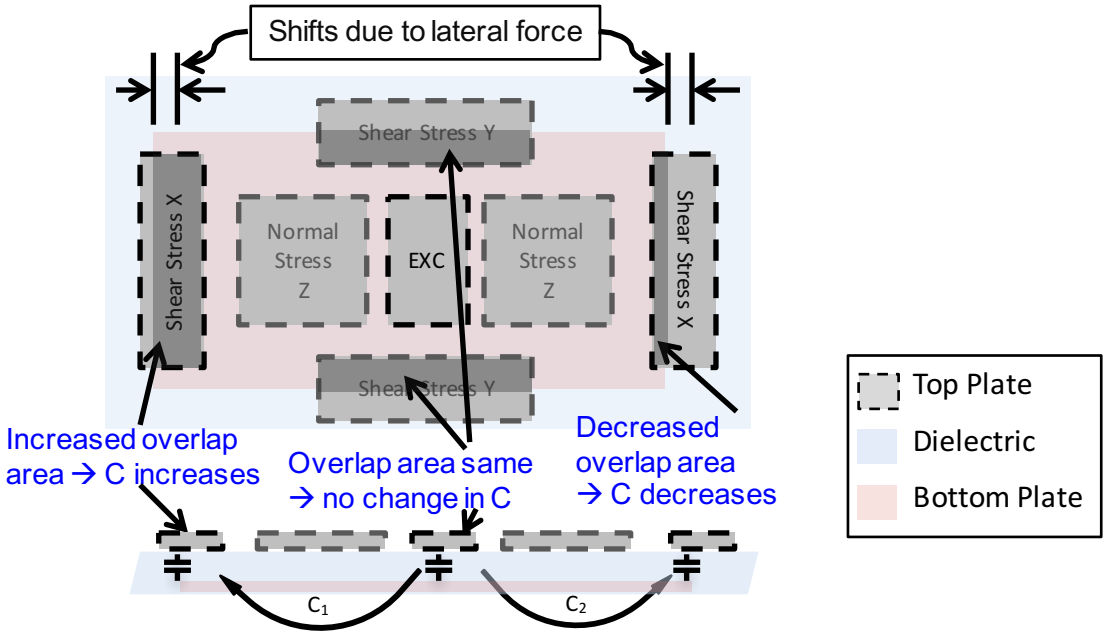

Figure 17 Illustration of how capacitance changes with shear force

Defining *y* as deflection due to the shear stress, we have the corresponding overlap area for *CIN(±)* and *EXC* plates as:

$$A_{CIN\pm} = (\frac{S}{4} \pm y')l$$

$$A_{EXC} = \frac{Sl}{4}$$

The differential capacitance C_y is the difference between C_1 and C_2, each of which comprises two capacitors in series, from its respective shear electrode to the bottom plate and bottom plate to the EXC electrode (Figure 17).

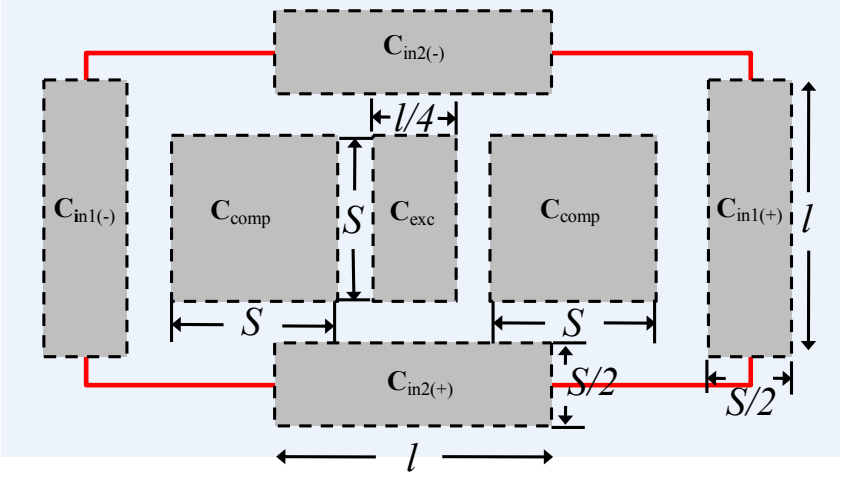

Figure 18 Size information for each fabricated plate

$$C_1 = \frac{(\frac{\epsilon_0\epsilon_r A_{EXC}}{d})(\frac{\epsilon_0\epsilon_r A_{CIN-}}{d})}{(\frac{\epsilon_0\epsilon_r A_{EXC}}{d}) + (\frac{\epsilon_0\epsilon_r A_{CIN-}}{d})} = \frac{\epsilon_0\epsilon_r}{d}\frac{A_{EXC}A_{CIN-}}{A_{EXC}+A_{CIN-}}$$

$$C_2 = \frac{(\frac{\epsilon_0\epsilon_r A_{EXC}}{d})(\frac{\epsilon_0\epsilon_r A_{CIN+}}{d})}{(\frac{\epsilon_0\epsilon_r A_{EXC}}{d}) + (\frac{\epsilon_0\epsilon_r A_{CIN+}}{d})} = \frac{\epsilon_0\epsilon_r}{d}\frac{A_{EXC}A_{CIN+}}{A_{EXC}+A_{CIN+}}$$

$$C_y = C_2 - C_1 = \frac{\epsilon_0\epsilon_r A_{EXC}^2}{d}\frac{A_{CIN+}-A_{CIN-}}{(A_{EXC}+A_{CIN+})(A_{EXC}+A_{CIN-})}$$

$$C_y = -\frac{\epsilon_0\epsilon_r}{d}(\frac{Sl}{4})^2\left(\frac{2yl}{(\frac{Sl}{2})^2-(yl)^2}\right) = -\frac{\epsilon_0\epsilon_r}{2d}\frac{S^2ly}{S^2-4y^2}$$

Shear stress τ is defined as $\tau = \frac{F_{shear}}{A}$, where A, as mentioned in the previous section, is the sensor area over which the force F_{shear} is applied. Shear stress is related to shear strain by $\tau = \gamma G$, where G is the shear modulus of the isotropic material, and the shear strain has the relation of $\gamma = \frac{y}{d}G$. The shear modulus is related to Young's modulus E by $G = \frac{E}{2(1+\upsilon)}$ where $\upsilon = 0.49$ is the Poisson ratio for PDMS. Combining the equations, we have the relationship $C_y = -\frac{\epsilon_0\epsilon_r l(1+\upsilon)}{AE}F_{shear}$.

$$y = \frac{F_{shear}}{AG} d = \frac{2F_{shear}(1+\nu)}{AE} d$$

$$C_y = -\frac{\epsilon_0 \epsilon_r S^2 l}{S^2 - \frac{16F_{shear}^2(1+\nu)^2 d^2}{A^2 E^2}} \frac{F_{shear}(1+\nu)}{AE}$$

Rearranging the equation, we have the quadratic equation

$$\frac{16(1+\upsilon)^2 d^2}{A^2 E^2} F_{shear}^2 C_y - \frac{\epsilon_0 \epsilon_r (1+\upsilon) S^2 l}{AE} F_{shear} - S^2 C_y = 0$$

The symmetric design allows us to obtain the same force and capacitance relationship for the shear *x-direction* as

$$C_x = C_y = \frac{\epsilon_0 \epsilon_r S^2 l}{S^2 - \frac{16F_{shear}^2(1+\nu)^2 d^2}{A^2 E^2}} \frac{F_{shear}(1+\nu)}{AE} \cong \frac{\epsilon_0 \epsilon_r (1+\upsilon) l}{AE} F_{shear}$$

The expected shear sensitivity for our design is therefore:

$$\frac{dC_x}{dF_{shear}} = \frac{dC_y}{dF_{shear}} = \frac{\epsilon_0 \epsilon_r (1+\upsilon) l}{AE} \cong 0.5 fF/N$$

3.3.2.3. coupling between normal and shear force

Although differential measurement of shear force should reject the effect of normal force to the first order, a large normal compression would change the baseline capacitance, impacting the sensitivity of the measurement to shear strain. To determine the range of normal forces that would have substantial impact to shear sensitivity, consider the change in baseline capacitance as the sensor is compressed in the normal direction.

$$F_{shear} = -\frac{\epsilon_0 \epsilon_r AES^2 l}{16(1+\upsilon) d^2 C_{shear}}$$

$$C_{shear,coupled} = -\frac{\epsilon_0 \epsilon_r AES^2 l}{16(1+\upsilon) d'^2 F_{shear}}$$

where we have the compressed distance between plates being:

$$d' = (1 - \frac{F_{normal}}{AE})d$$

$$C_{shear,coupled} = -\frac{\epsilon_0 \epsilon_r AES^2 l}{16(1+\upsilon)(1-\frac{F_{normal}}{AE})^2 d^2 F_{shear}}$$

As long as $F_{normal} \ll AE\ (180\ N)$, which it does in the applications considered here, we can ignore the normal force to calculate the shear force.

3.3.3. Fabrication process

The fabrication process of the proposed single-sided capacitive sensor is shown step by step in Fig. 19:

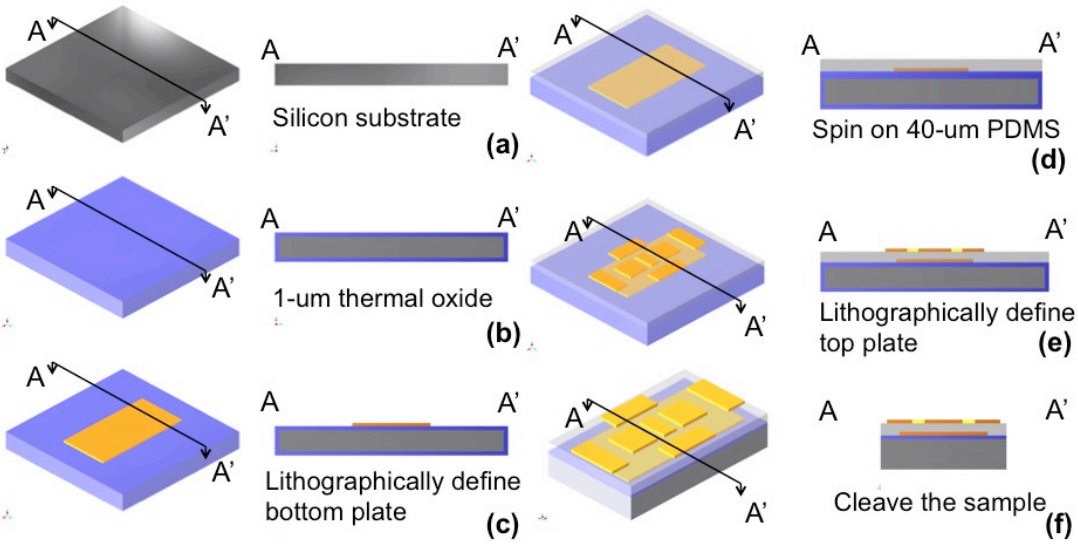

Figure 19 Fabrication process for capacitive sensor (a) silicon substrate (b) thermal oxidation (c) evaporation and liftoff (d) spin on and cure PDMS (e) evaporation and liftoff (f) cleave sample and release final device

Step 1: Thermal Oxidation. Starting with a silicon substrate, grow *1 um* oxide (SiO_2) in the furnace using the wet oxide recipe at temperature *1050 C* (*a*).

Step 2: Define the top bottom pattern. Use the SVG track coater recipe 2,2,2 to take care of the wafer prime, bake, and spin softbake steps. Exposure the wafer in Karl Suss III for *10 second* using hard contact recipe. Use recipe 2,2,2 in SVG development coater to take care of the post-exposure bake, develop, and hardbake steps. Use Matrix Descum recipe at *50 C* to clean the wafer.

Step 3: Evaporate Ti/Au/ Ti to create bondable surface for assembly and back-end processing. using CNSI CHA to deposit a Ti/Cu/Ti seed layer (*b*). The bottom *20-nm* Ti layer works as the adhesion layer, while the top *20-nm* Ti layer serves as a mechanical robust, biocompatible electrode. The *300-nm* Au layer is used to be bonded as a biocompatible electrode.

Step 4: Lift-off resist to reveal the bottom metal pattern. We need to strip the photoresist using NMP in an *80 C* beaker with a stir bar. Next we put the wafer in a beaker filled with acetone, and put the beaker in ultrasonic machine for *5 second*. Finally descum the wafer using matrix asher at 80C.

Step 5: Spin coating a *35-um* polydimethylsiloxane (PDMS) layer (c). The recipe is under examination so far, but ideally, we prepare a *10:1* solvent to hardner (*40-mL:4-mL*) using Thinky Mixer (detailed in *Appendix B*) for *5 minutes* to well mix the material, then put in the vacuum dessicator for one hour to get rid of any air bubbles. We spin on a *5-mL 5:1* ratio PDMS onto our wafer, with spinning condition as: *500 rpm* at *100 rpm/s* for *5 seconds*, and then *2000 rpm* at *300*

rpm/s for *30 seconds*, and finally *25 rpm* at *100 rpm/s* for *15 seconds* to stop. We can use the Q-tip with acetone to remove the edge bead. We put the wafer in a high vacuum chamber for *30* minutes before we cure it in an oven at *100 C* for *2 hours*.

Step 6: lithographically defining top plate (*d*). As a standard routine, we put the wafer in HMDS for *10 minutes* before spin on KMPR 1005. The recipe is *500 rpm* at *100 rpm/s* for *5 seconds*, *2000 rpm* at *300 rpm/s* for *30 seconds* and *25 rpm* at *100 rpm/s* for *15 seconds*. Next, soft bake on the hotplates for *5 minutes* at *100 degree*. Next do the exposure using Karl Suss III same as before but with soft contact technique for *2 minutes*. After exposure and post bake at *100 degree* for *2 minutes*, we use SU-8 to develop for *2 minutes* and *30 seconds* with strong agitation. Clean the wafer with IPA for *10 seconds*, and spray rinse with DI water for *20 seconds*. Dry with nitrogen gun.

Step 7: We repeat the evaporation and liftoff process with *20-nm* Ti and *300-nm* Au to get the top seven pads as electrodes (*e*).

Step 8: we can cleave the sample to get the devices (*f*).

The prime problem with the fabrication process is the height control of PDMS. For a robust and repeatable manufacture, the thickness must be both accurately controllable and uniform across the entire film. The spin-coating technique is employed to meet the requirement of a uniform thickness PDMS layer.

Assume that we pour the PDMS on the wafer as a cylinder with height h_0 and diameter d. By using Navier-Stokes equation, the height of the PDMS can be derived as:

$$\frac{1}{h_t^2} - \frac{1}{h_0^2} = \frac{4\rho\omega^2 t}{3\mu}$$

where h_t is the height of the PDMS, h_0 is the initial height of the poured PDMS, ρ is the density of the PDMS, ω is the spin speed, t is the spin time, and μ is the dynamic viscosity of PDMS. From the expression, we notice that, the final height is uniform, not related to the radial location or the size of the film (the size of the wafer). However, it is sensitive to the initial height. If we make $h_t \gg h_0$, i.e., making the initial pour volume large, the initial height will no longer be an issue.

$$h_t \approx \sqrt{\frac{3\mu}{4\rho\omega^2 t}}$$

However, various factors will affect PDMS's property, including the dynamic viscosity, modulus of elasticity, Poisson's ratio, tensile strength and adhesion energy. For example, the dynamic viscosity increases over time once monomer and cross-linker are mixed. The Young's modulus is sensitive to the temperature and time during curing as well as can increase with the increased ratio of cross-linker to monomer. The remaining issue yet to be adequately resolved are how accurate the height model is and how accurate the properties of the PDMS can be made as desired.

Table 5 shows material properties for silicon dioxide, silicon nitride, polyimide, parylene C, polyethylene, and PDMS. The major difference is their Young's modulus. Besides PDMS, the other five materials all have Young's modulus in GPa range, while what PDMS has Young's Modulus in the MPa range. The sensitivity, shown previously, is inversely proportional to Young's

modulus. With all the other parameters equal or close, PDMS exhibits at least two orders of magnitude better sensitivity. From resolution point of view, we expect only PDMS and Polyethylene (PE) can meet the requirement of less than 1N resolution (the noise used to calculate resolution is *20 aF* from AD7746 datasheet [136]).

Table 5 Material properties including silicon dioxide, silicon nitride, polyimide, parylene C, polyethylene, and PDMS

Material	ε_r	Young's modulus (GPa)	Poisson ratio	Normal sensitivity (fF/N)	Shear sensitivity (fF/N)	Normal resolution (N)	Shear resolution (N)
Silicon Dioxide	3.9	70	0.17	2.50e-04	5.70e-05	8.00	351
Silicon Nitride	7.5	310	0.24	1.10e-04	2.66e-05	1.82	752
Polyimide	3.4	2.5	0.34	6.02e-03	1.61e-03	3.32	124
Parylene C	3.2	2.4	0.4	5.90e-03	1.65e-03	3.39	121
Polyethylene	2.25	0.12	0.46	8.30e-02	2.42e-02	0.241	0.826
PDMS	2.75	1.00e-03	0.49	12.2	3.63	1.64e-03	5.51e-03

3.3.4. Sensor scaling performance

Figure 20 A typical surgical grasper used in the da Vinci surgical system

Currently, our sensor size and shape are mostly decided by the surgical grasper, as shown in Fig. 20, while miniaturization is easy to be implemented by MEMS fabrication process. When considering the scaled performance, a table of scaled parameter performance is calculated and presented below (the detailed calculation is in Appendix D). We can figure out from this table that in order to maintain the same electrical field in the device, we need to scale the power by the same scaling factor, then, the circuit delay time, the power dissipation, the circuit density, the thermal noise, both normal and shear sensitivity, and both normal and shear resolution all taking the

advantage of the miniaturized size. However, we should also note that the linear dynamic range suffers from the scaled size by a factor of $1/\kappa^2$ (i.e., if currently we have a linear dynamic range of 90 N for the normal direction, by shrinking the length of both sides by a factor of κ, we would have only 10 N of the linear dynamic range, which would pose a challenge for us. But, it is still something we can overcome by a modification of some of the parameters, for example, the thickness of the PDMS (d).

Table 6 Sensor scaling performance

Scaled parameters	Constant field scaling
S, l, d	$1/\kappa$
Chip area (A)	$1/\kappa^2$
Power supply (V_{dd})	$1/\kappa$
Electric field in device (E)	1
Capacitance	$1/\kappa$
Circuit delay time τ (CV/I)	$1/\kappa$
Power dissipation (P)	$1/\kappa^2$
Power density ($\sim P/A$)	1
Circuit density	κ^2
Current (I)	$1/\kappa$
Sensitivity	κ
Thermal noise	$\sqrt{\kappa}$
Resolution	$\sqrt{1/\kappa}$
Linear Dynamic range	$1/\kappa^2$

Chapter 4: Sensing Circuit

The Capacitance-to-digital Converter (CDC) Chip AD7746 offers us a simple solution to the capacitance measuring circuit, which has a resolution down to 4 aF and can take in differential inputs for the two of the shear force directions. By flip-chip bonding the sensor to the designed printed circuit board (PCB), we can integrate the tri-axial capacitive sensor with a surgical operating grasper.

In the dissertation, we will go over three versions of the PCB we have made. The first and second versions are flexible PCB as I call later version I, for their advantages such as high reliability, great space utilization, and small in size. We then designed our version II rigid PCB for advantages such as lower cost, less complexity, better noise performance, easier integration with the grasper, and capability of disposable. We further improved with a version III, making the sensing system more durable and stable, miniaturized in size, enhanced noise performance, and waterproofing feature.

Afterwards, the capacitive data from the sensing chip will be relayed to the microcontroller for software processing using an I2C interface detailed in Chapter 5.

4.1. Capacitance-to-Digital Converter AD7746

Our readout circuit encompassed two high resolution AD7746, which were implemented on a printed circuit board (PCB). The chosen converter has *24-bit* accuracy on capacitive data readings, and a resolution down to 4 *aF*. It is designed for floating capacitors and can take in differential inputs for our two-directional shear force.

4.1.1. Analog-to-digital conversion

A simplified process flowchart for analog-to-digital conversion (ADC) is drawn in Fig. 21, and a vivid picture showing the process is also shown. We can find that the continuous time data goes into an anti-alias filter and get the samples and hold. The discrete time with continuous amplitude data come out from the sampling, after the quantization, we get discrete time and discrete amplitude data, which is then going through a digital encoding to be our digital bits.

ADC can vary greatly. A *10-bit* ADC means it has the ability to detect $(2^{10}=)$ *1024* discrete analog levels and a *16-bit* ADC has $(2^{16}=)$ *65536* discrete levels.

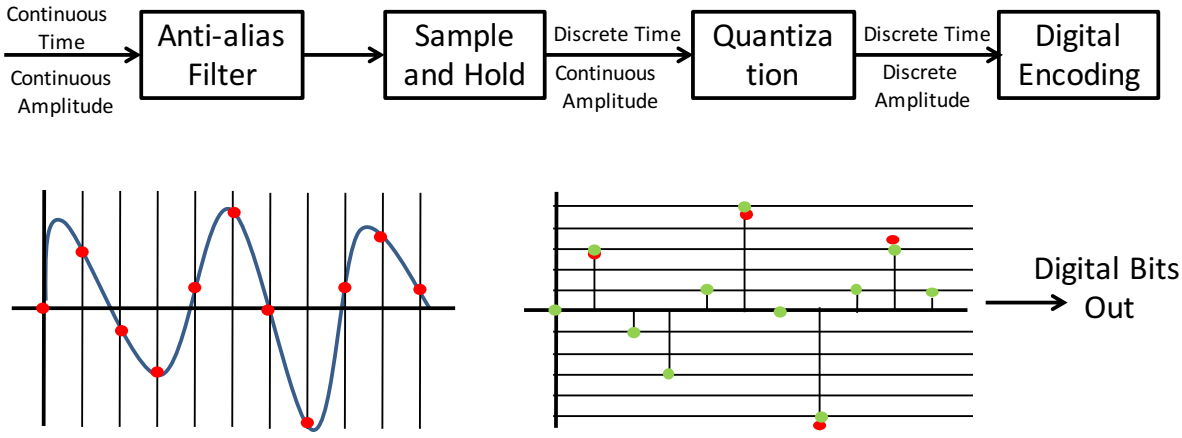

Figure 21 The process of analog to digital conversion

4.1.2. Comparison between different CDCs

The reason for choosing AD7746 for our project is basically coming from the channel number needed, the capability to handle differential capacitance input, the resolution and the noise resistance capability. Table 7 shows a comparison between different CDCs.

The AD714x series are ideal for multiple capacitance inputs, such as a capacitor array. However, their functionality only based on single-ended sensor, we would need to utilize a differential amplifier in order to use them.

The AD774x series are based around a *24-bit* sigma-delta modulator, which directly converts the capacitance value of the sensor into a *24-bit* digital output. In this series, AD7745 and AD7746 are designed for floating capacitive sensors, meaning neither trace on the capacitive sensor input pins is grounded, while AD7747 is designed for grounded capacitive sensors. We chose AD7745/6 over AD7747 because AD7747 is much more prone to parasitic capacitance. Since both traces are floating in AD7745 and AD7746, only capacitance formed between the two traces will contribute to the system base capacitance.

Both AD7745 and AD7746 are good candidates for our project. The only difference is that AD7745 allows for one channel of conversion while AD7746 allows for two, where each channel can be configured as single-ended or differential, perfect for our project. We can use the single-ended mode for normal force measurement and differential mode for shear force measurement.

Table 7 Comparison for different CDCs

	Channels	Resolution	Problem/ advantage
AD7745,7746	1-2	1fF	Floating; Differential inputs
AD7747	1	1fF	1 channel; Differential, grounded
AD715X	1-2	Low	Cheap, low power consumption
AD714X	Multiple		
AD7147, 7147	13	~8fF	Grounded
AD7142	14	1fF	Need differential amplifier
AD7143	8	1fF	Grounded, Need differential amplifier

4.1.3. Working principle of AD7746

As described in the Chapter 4 introduction part, the AD7746 is the mediate between our proposed capacitive sensor and the microcontroller. The AD7746 uses direct method for measuring the capacitance. In this method, the electrode is injected by high precision current source with a known value and time, later AD7746 measure the voltage on the electrode pair. To measure the voltage, high impedance input and a very low current are required. Capacitance value that has been converted into a voltage is then converted into digital data through sigma-delta analog-to-digital converter (ADC) circuit.

The core of the AD7746 is a *24-bit* Sigma-Delta architecture ADC which is modified to convert capacitance directly to a corresponding digital signal. A simplified diagram of this CDC in the AD7746 can be seen in Fig. 22. At a high level, the Sigma-Delta CDC functions by balancing charge through two capacitors – the variable sensor capacitor, and an internal reference capacitor. The capacitors are switched between a fixed input voltage to charge them, and then discharge through an integrator.

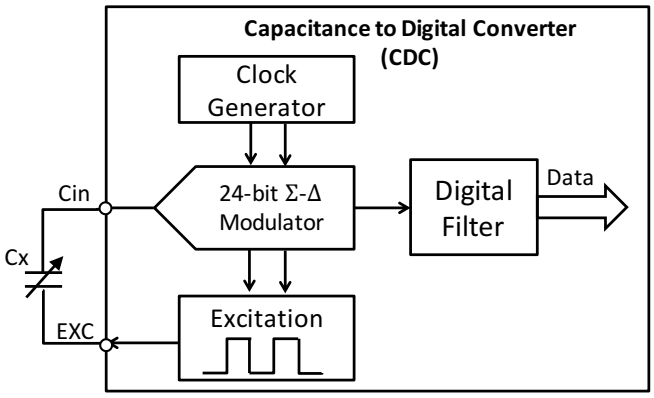

Figure 22 AD7746 simplified Block diagram (redraw from [136])

In AD7746, the high-resolution capability is mainly through a technique called oversampling, which uses a sampling frequency much higher than Nyquist rate. This technique, besides to improve resolution, can also reduce noise and avoid aliasing.

As for the wiring, we use two CDCs in our read-out circuit, one for normal sensing, and the other for shear sensing. The single-sided sensor, as displayed in Fig. 23, has two pads made for normal compression and five pads made for shear sensing. The left compression pad is connected to the normal CDC excitation pin, the right compression pad is connected to normal CDC capacitance input to get compression capacitance; as for the shear sensing, the center pad is connected to the shear CDC excitation pin, and the surrounding four shear sensing electrode pads are connected to the capacitance input pins on the shear sensing CDC.

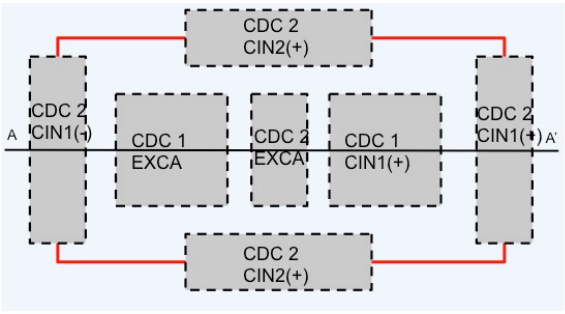

Figure 23 Illustration of wire connection for single-sided sensor with AD7746

4.1.4. Data acquisition from AD7746

Data acquisition is the process to get the real world physical property and convert it to digitalized numeric data, which can be manipulated by a computer for further analysis. In our case, the data acquisition includes, first, the capacitive sensor which can convert physical parameters into electrical signals, and next, a sensing circuit, which can convert electrical signals into a form which can be converted to digital values. AD7746 is not a stand-alone device, it requires a host processer

(typically a microcontroller) to configure it and process the data it produces. The analysis is then performed to give us 3-axial force values as well as information about noise, resolution etc.

The AD7746 interfaces with the chosen microcontroller using the I2C communication system, in which the AD7746 is the Slave and the microcontroller is the Master. I2C stands for "Inter-Integrated Circuit", and is technically a multi-master serial single-ended computer bus. More details can be found in Chapter 5.

The interface connection mentioned above can be achieved by either employing *RS232*, USB, *I2C* (inter-integrated circuit bus), *SPI* (serial peripheral interface), *UART* (universal asynchronous receiver transmitter) or some *GPIO* (general purpose input/output). In our case, The AD7746 supports an *I2C* compatible serial interface, thus the *I2C* interface is used. More communication protocols details can be found in Chapter 5.

The *I2C* communication system is a two-wire system involving a SCL (clock) and a SDA (data) line. These two wires carry all address, control, and data information bit-by-bit over the bus to and from all connected devices. The controlling processor (typically a microcontroller) in a system is known as the I2C Master, and the devices under control, are known as the *I2C* Slaves (AD7746). The Master is responsible for producing the clock signal that synchronizes the Master and Slave devices, and for initiating all data communications between the two devices using standardized procedures as shown below:

1. Data Transfer is initiated with a START bit signaled by SDA being pulled low while SCL stays high.

2. SDA sets the first data bit level while keeping SCL low.
3. The data is received when SCL rises for the first bit.
4. This process repeats, SDA transits while SCL is low, and the data is read while SCL is high.
5. A STOP bit is signaled when SDA is pulled high while SCL is high.

The Slave AD7746 measures the capacitance and converts it to digital data which is stored in three 8-bit registers inside AD7746. This data is passed onto the register block through the I2C bus, which can be then processed and analyzed by the microcontroller.

The AD7746 contains *19 8-bit* registers, 10 of them must be set to configure the CDC into the correct operating mode for the proposed sensing system. The microcontroller is responsible for writing the correct binary data or the hex value into the registers.

The *10* registers of interest to our project are status register, capacitance data register H, capacitance data register M, capacitance data register L, configuration register, cap DAC A and capacitance setup register.

The first four registers (first two lines) in Table 8 are read-only registers while the rest six (last five lines) are read/write registers and they need to be set initially for a specific value before a capacitance measurement.

Table 8 Major CDC registers used in our project, with the functions that are used

Registers	Function
Status Register	provides details on the current status of the AD7746 converter to the Master
Cap Data Register	three separate registers containing the current capacitive data from the capacitive sensor
Cap Setup Register	allows configuration of the capacitance input
Voltage Setup Register	allows configuration of the voltage input
Excitation Setup Register	allows configuration of the excitation signals
Configuration Register	allows configuration of the mode of operation of the AD7746
Cap DAC A/B Register	stores the capacitance data used to null out the base capacitance for channel 1/ channel 2

Configuration register: as shown in Table 8, its function is to allow the configuration of the mode of operation of the AD7746, it is one of the most important registers. Its address pointer is *0x0A*, and the default value is *0xA0*. For *continuous conversion mode*, the configuration register values are listed in Table 9. For idle state (which will be used for power saving purpose, the register value should be set to *00000000*. While the power down register value should be set to *00000011*.

Table 9 The binary value and Hex value for the configuration register values under different capacitor conversion time and voltage conversion time conditions for continuous conversion mode.

Cap Conversion time	Voltage Conversion Time							
	20.1 ms		32.1ms		62.1ms		122.1ms	
11.0 ms	00000001	0x01	01000001	0x41	10000001	0x81	11000001	0xC1
11.9 ms	00001001	0x09	01001001	0x49	10001001	0x89	11001001	0xC9
20.0 ms	00010001	0x11	01010001	0x51	10010001	0x91	11010001	0xD1
38.0 ms	00011001	0x19	01011001	0x59	10011001	0x99	11011001	0xD9
62.0 ms	00100001	0x21	01100001	0x61	10100001	0xA1	11100001	0xE1
77.0 ms	00101001	0x29	01101001	0x69	10101001	0xA9	11101001	0xE9
92.0 ms	00110001	0x31	01110001	0x71	10110001	0xB1	11110001	0xF1
109.6 ms	00111001	0x39	01111001	0x79	10111001	0xB9	11111001	0xF9

Cap setup register: this register allows the configuration of the capacitance input. Shown in Table 10, when we sense the normal force, we need to set this register to *0x80*, and when we need to sense the shear force, we need to set the register to be *0xA0* and *0xE0* respectively for x and y directions. Its address pointer is *0x07*, and default value is *0x00*.

Table 10 The capacitance setup register binary and HEX values for different capacitance configuration modes (normal, shear x, and shear)

Cap Setup Register	Binary	HEX
normal	10000000	0x80
shear (cin1+/-)	10100000	0xA0
shear (cin2+/-)	11100000	0xE0

EXC setup register (for voltage level $\pm Vdd/2$): this register allows the excitation signal configuration. I only calculated and listed the values for voltage level $\pm Vdd/2$ for a normal faster conversion time in the Table 11. The address pointer of this EXC setup register is *0x09*, and default value is *0x03*.

Table 11 The binary and HEX values for EXC setup register configuration different sensing modes and for differnet conversion time.

EXC Setup Register	Binary	HEX
Normal	00001011	0x0B
Normal (faster conversion)	10001011	0x8B
shear	00101011	0x2B
Shear (faster conversion)	10101011	0xAB

Status register: this register is a read-only register, which provides the current status of the AD7746 to the master controller. For example, we will know when the conversion is finished by reading a *00000011* from this register. The address pointer is *0x00*, and default value is *0x07*. For the debugging purpose, we need to check the status value regularly, and here is the indicating table:

Table 12 The indication of values of the status register of the AD7746

Status Register	Indication/ Meaning
00001111	exc output error
00000011	conversion on the enabled channel is finished
00000101	conversion on the voltage/temp channel is finished
00000110	conversion on capacitive channel is finished

After the initial configuration of the registers of the AD7746, the process of capacitance measurement followed by capacitance-to-digital conversion takes place. The digital cap data obtained is stored in *3 registers* (capacitance data register H, capacitance data register M and capacitance data register L) of *8-bit* size each, located at register pointer address *0x01, 0x02, and 0x03*, forming a *24-bit* capacitance data. The registers should be transferred and read sequentially by *I2C* bus onto our register block module.

The AD7746 is first reset to clear any data or settings. The excitation signal is then setup to be full strength of Vdd. Next, the CAPDAC's are set to null out the base capacitance of the system close to 0. The capacitive channel is setup to put it into single-ended mode at a sample update of a required timing, for example, *62 ms*. Finally, the AD7746 is placed into continuous conversion mode, where it will start producing *24-bit* capacitive data readings approximately every *62 ms*. The data is stored in three registers, each of *8-bits*, and must be read sequentially to ensure that no data corruption occurs. After the initialization sequence is complete, the microcontroller polls the status register of the AD7746 to determine when a capacitive data sample is available to be read.

When the status register bit goes high, the microcontroller reads from the three capacitive data registers sequentially and stores the data for processing.

4.2. Flexible PCB Design Version I

The layout and geometry of the printed circuit boards (PCBs) are critical to the functionality of the sensor. Initially, a flexible PCB (FPCB) was considered, as flexible PCB has many advantages compared with rigid PCB, for example, FPCB is small and light weight, foldable to conform to a 3-D shape, has better space utilization, high shock and vibration resistance, and high reliability during dynamic bending.

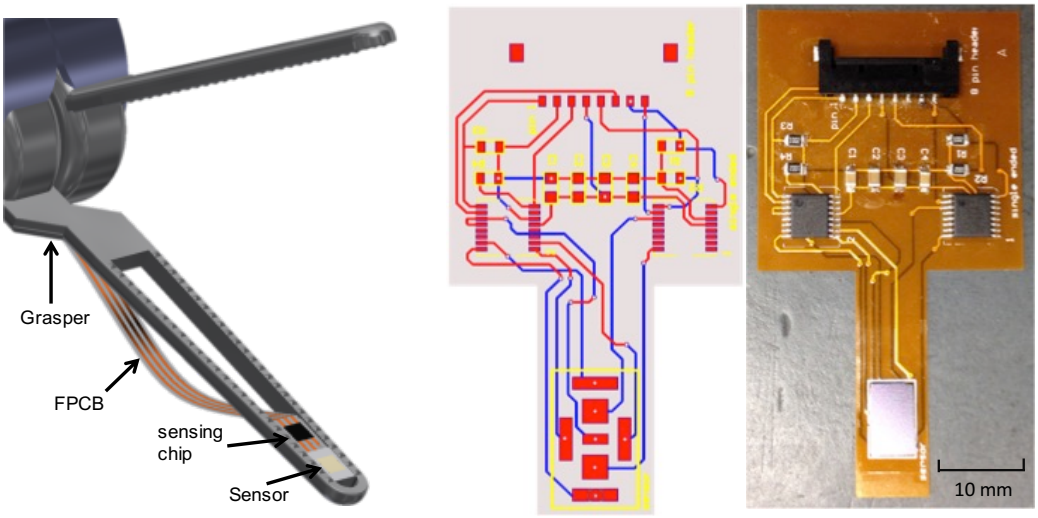

Figure 24 (left) PCB layout for single-sided sensor (right) real object after soldering components

Fig. 24 demonstrates the initial idea of integrating the capacitive sensor to the surgical grasper tip. The complexity of the circuit can be effectively reduced by implementing the sensor with the FPCB, and thus makes the device highly manufacturable. A first version FPCB is shown in Fig. 15(c). In the circuit board design, V_{DD}= *3 V* (*2.7 V* to *3.6 V* as recommended), C_1= *0.1 uF,* C_2= *10*

uF, and pull-up resistors $R_1 = R_2 = R_3 = R_4 = 100\ k\Omega$ are used. In order to eliminate the interference with surgical tasks, the narrow board region is designed on purpose for grasper integration.

The general idea is demonstrated below, on the flexible PCB, the sensor is connected to two CDC chips, PC provides the CDC chips with the required DC and AC voltage while get the data from the CDC chips. Next, the LabVIEW written code communicates with the CDC chips and get the desired capacitance/ force information from the sensors.

Our second version of the FPCB is shown in Fig. 25, we made it *16-inch* long to better integrate with the grasper.

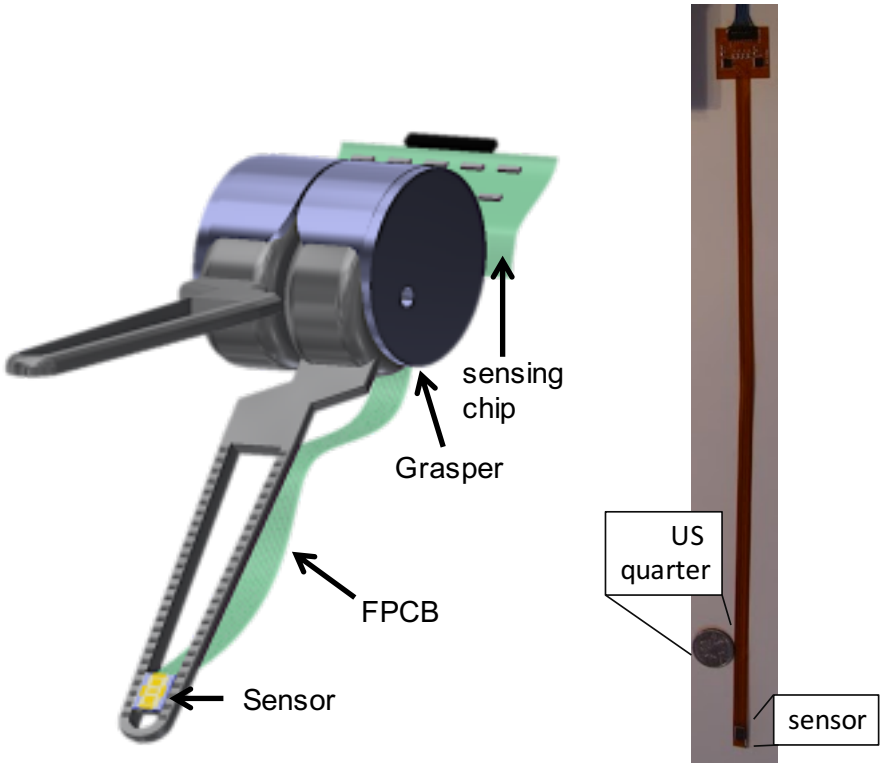

Figure 25 A 16-inch long version of the FPCB for better integration with the surgical grasper with a U.S. quarter for size comparison. The sensing circuit is left to the backsdie of the grapser to elimiate the size constrant.

4.3 Improved PCB Design Version II

Next, a four-layer PCB is considered, as this would reduce the complexity and cost of assembly of the device. In this case, the bottom layer contains the surface-mount components and a connector header to connect with the microcontroller, the second layer contains a ground plane (ground shield), the third layer contains a ground plane (ground shield), and the top layer would contain all other surface-mount components and one connector which connects with the sensor board.

The circuit interface PCB for sensor consists of a sensor and a through-hole *1.27 mm* pitch connector. The sensor board is *0.4 mm* thick and has dimensions of *11 mm* × *11 mm*. The sensor is soldered on the PCB through seven electrode pads from the front end.

The PCB for measuring capacitance is designed as a four-layer PCB board to reduce the complexity and cost of assembly of the device with a thickness of *0.8 mm* and a dimension of *14.20 mm* × *15.30 mm*. A 3D breakout layout of the sensing unit is shown in Fig. 26©. The PCB is connected to the sensor board using the *1.27 mm* pitch connector.

The main components on the PCB for measuring capacitance are a voltage regulator and two *24-bit* Capacitance-to-Digital Converters (CDC). The voltage regulator has a *470 pF* capacitor that connects between the bypass input and ground in order to reduce the noise from the internal reference, which also reduces output noise. The voltage regulator outputs a steady *3.3-V* voltage with *0.05mV* root mean square (RMS) voltage noise. The *3.3-V* voltage output is then is then fed into two CDCs.

The CDC AD7746 has a resolution down to *4 aF* and an accuracy of *4 fF*, with *0.7 mA* current consumption [136]. The core of the AD7746 is a *24-bit* Sigma-Delta architecture ADC which is modified to convert capacitance directly to a corresponding digital signal. It is designed for floating capacitors and can take in differential inputs for our two-directional shear force. One CDC is used to translate the capacitance reading in the normal direction (z-direction) and the other is for shear directions (x-direction and y-direction). The CDCs are connected with the control system by means of I^2C communication and two 10-kΩ resistors are used as the pull-up resistors on Serial Interface Clock Input (SCL) and Serial Interface Bidirectional Data (SDA) port on each of the CDCs. When running in continuous conversion mode, CDCs generates an excitation of *32 kHz* and are configured to update at a rate from *9.1 Hz* to *90.9 Hz*, with a conversion time from *109.6 ms* to *11 ms*.

In order to make sensor unit to be disposable, we made the boards to be two pieces, one for sensor board only, and one for the circuit board, they are easily connected together by 0.1'' micro-connectors (see Fig. 26c for the board connector location). With this novel design, we can easily toss away the sensor board after each clinical usage, and keep the circuit board for economic efficiency. And the connector design made no exposed wiring in the air, largely improved the noise performance. To further improve the noise performance of our capacitive sensing, a voltage regulator is implemented to regulate the changing voltage to a steady *3.3 V* with a voltage noise being only *0.02 mV*. So far, with this changed board design, we have improved our noise performance by more than 5X.

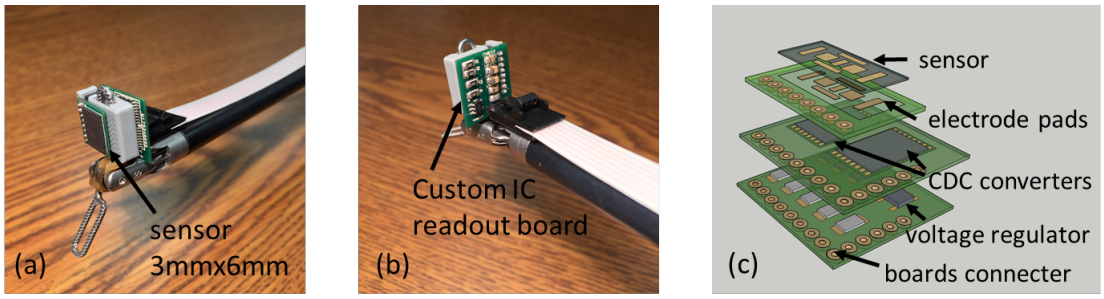

Figure 26 (a) The fabricated sensor integrated with surgical grasper by customized 3D print case (b) The backside of the custom readout circuit board (c) 3D breakout layout for the sensing unit

This is the first-time demonstration of our capacitive sensor successfully integrated with the surgical grasper. The fabricated sensor is flip-bonded to this custom printed circuit board (Fig. 26a) using a 3D printed case to integrated with surgical tools and the rest of the tactile feedback system. The advantage is obvious: the customized 3D printed case enables the sensor to be used with any surgical instrument, and even applications beyond medical robots. A 3D breakout layout of the sensing unit is shown in Fig. 26c.

4.4. Final PCB Design Version III

4.4.1. Revised circuit board

To recall that our previous version circuit board has a size of 14 *mm* x 15 *mm* x 0.8 *mm*, it is a 4-layer board with through hole connector. This board, while functional and miniature, had several areas that needed improvement. First, it cannot fit the trocar for the surgical applications; second, the exposed pins are in the way for surgical tasks, such as suture tying, tissue manipulation; third, the wires were too short to easily accomplish the desired tests and the height of the ribbon connector was an impediment to accomplishing some tasks; fourth, the sensor could shear off the board under an applied force that was high but still within the range that surgical tasks would need;

and finally, in order to suit for the surgical environment, we need to consider the tough environment that the sensor needs to survive in, i.e., to withstand the radio frequency (RF) interference in the operating room and the damp environment for the in-vivo even the ex-vivo test.

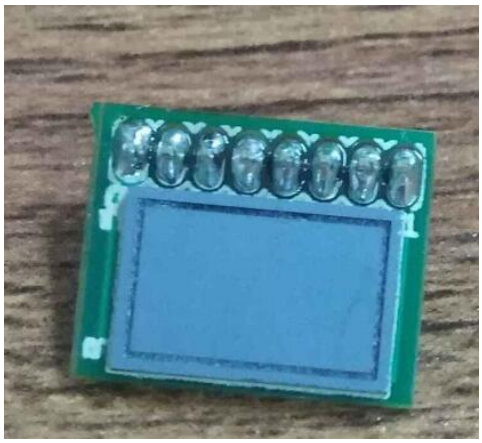

Figure 27 The exposed pins on the sensor board, which is in the way for doing surgical tasks

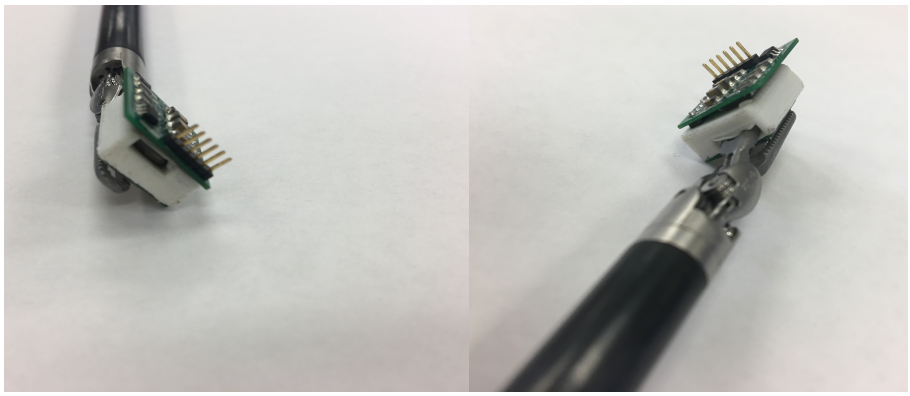

Figure 28 Last version PCB board version II,

All these issues must be considered in order to design the instrumented device, so that it can be properly integrated onto the tip of surgical instrument working safely in ex-vivo and in-vivo environments.

Our latest version PCB board, shown in Fig. 29, has a miniaturized size of 11 *mm* x 15 *mm* x 0.6 *mm* to fit the trocar, a thinner PCB with surface mounted flat drawer connector, to be used with a

1-meter-long flexible cable. Additional features of this version include an embedded thermal sensor, waterproofing coating, electrical ground planes as well as lightweight sensing structure (total weight 1.10 g).

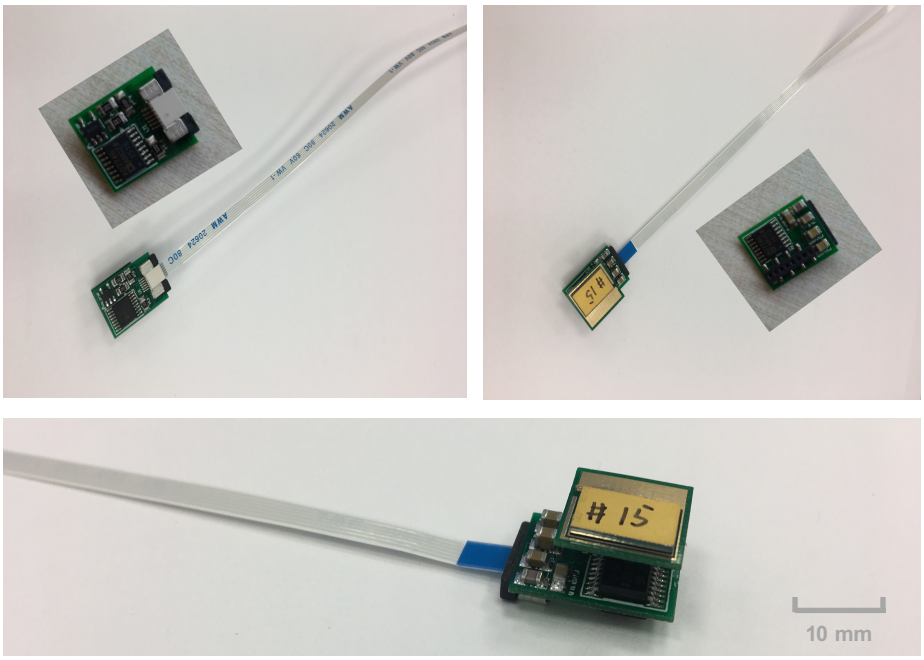

Figure 29 Latest PCB version with benefit of miniaturized size, reduced weight, waterproofing coating, grounding plane, embedded thermal sensor and more stable cable connection.

Fig. 29 shows our final version miniaturized sensor board to fit the trocar with 1-meter-long flat drawer connector, which is long enough for testing on da Vinci, much stable connection that will not fall off during the operation, and no extruded wires for any surgical application. It has additional features as embedded thermal sensor, waterproofing coating, grounding planes, as well as more steady connection between the sensor and the sensor board via glue. Each of these features will be detailed later.

Fig. 30 shows the latest fabricated sensor with the manufactured PCB integrated with the surgical grasper with a 3D print case.

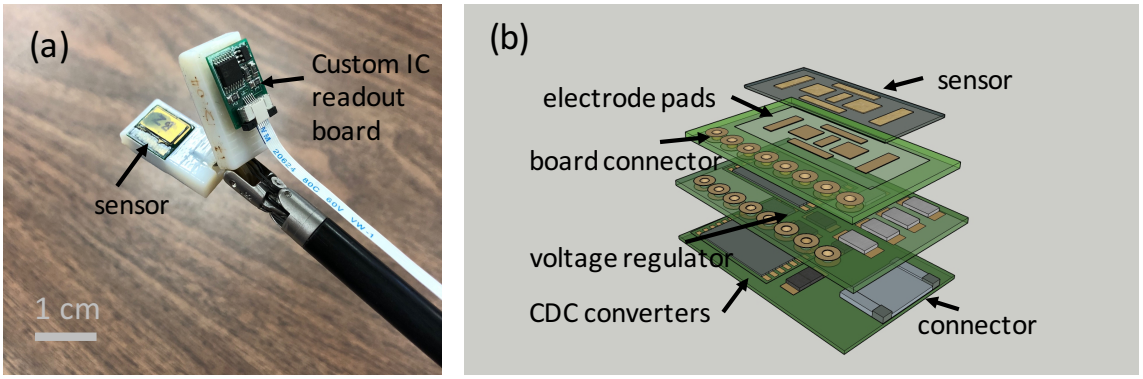

Figure 30 (a) The fabricated sensor integrated with surgical grasper by a custom 3D printed case (b) 3D breakout layout for the sensing unit

4.4.2. Noise & grounding

There are several ways been applied for grounding and to improve noise performance. For example, a surface-mounted connector was chosen, as opposed to a through-hole connector with exposed pins on the surface, to mitigate sensitivity to changes in the dielectric permittivity of the surrounding material. The sensor PCB is also covered by a ground plate on the top layer. Since multiple ground paths may exist, a cut is made in the ground loop to mitigate any effect from ground loops.

4.4.2.1. motivation

Capacitive sensor is very sensitive to, first, the dielectric influence, e.g. gentle human hand contact alone make a huge change of the capacitance. From the supplementary movie, we can find that if pins are exposed or the PCB is insufficiently grounded, touching near the sensor will read as a capacitance change due to the high permittivity of the human body as compared to air. The huge

change from the human hand contact is much larger than the continuous larger force applied by the hand after the initial contact. And this phenomenon is negatively influenced the performance of the sensing system because the sensor will be inevitably in contact with many types of materials, especially for ex-vivo test and in-vivo test. Second, capacitive sensor is sensitive to the noise coming from environment, especially for RF interference, which is common in surgical environment.

In order to get rid of the spikes that comes from human hand or dielectric influence and to get rid of the influences that comes from EM waves, a systematic grounding method must be developed. Because the nature of the sensor fabrication, it is difficult to make grounding signal directly to the sensor unless very complicated fabrication steps are developed. In this section, we will talk about an easy grounding method that is applied to our system for 1) the sensor PCB board 2) the capacitive sensor and 3) the connection method.

4.4.2.2. the sensor PCB board has a grounding plane

The initial plan is to make a sensor PCB board that have an exposed plane that is connected to a ground pin, making a ground plane. And we can connect the ground plane to the sensor, which has an exposed way to a conducting surface, to make a ground plane in the sensor itself. And apparently the connection method must also be conducting.

The way to make a ground plane to the sensor PCB board is as simple as has a surrounding area that is covered by Copper directly and is connected to a ground pin. To decrease the noise caused from the ground plane, we have cut the ground loop.

4.4.2.3. the sensor has a grounding surface

The most critical aspect for the grounding method is the sensor part. We had come up with three ways to add a grounding surface to the sensor.

4.4.2.3.1. embedded grounding layer

The first way is to ground a center gold layer and then connect the sidewalls to the grounded plane on the sensor PCB board (Fig. 31). However, since there is a conducting layer for the plates, we must separate the two layers by an insulating layer.

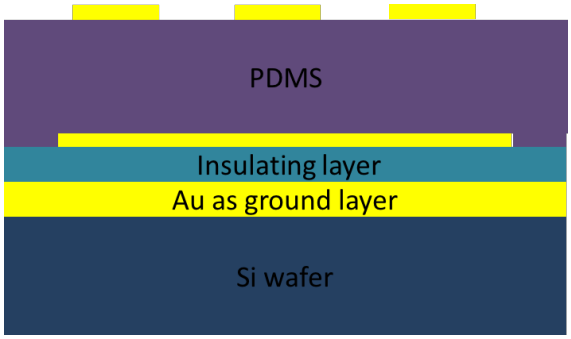

Figure 31 The demonstration of the first grounding method of the sensor

Two recipes have developed.

The first is to use CHA to deposit the insulating layer and the conducting layer. We have modified the CHA recipe to have *10-nm* Ti/*100-nm* Au/ *10-nm* Ti as the conducting layer and then deposit by CHA again *200-nm* SiO_2 as the insulating layer. The recipe is attached here for reference (Table 13). The benefit is the convenience by using the same machine. There are two concerns, first is 100nm Au layer maybe hard to contact to the grounded PCB plane. Second, the insulating plane can neither be too thick nor too thin, where the Au particles might diffuse through to cause short circuit.

Table 13 CHA recipe for using Au layer as grounding layer, SiO_2 as insulating layer

		Layer 1	Layer 2	Layer 3	Layer 4
Material index	(1-24)	Ti (1)	Au (7)	Ti (1)	SiO2 (9)
Rate	A/sec	1	2	1	1
Final thickness	KA	0.1	1	0.1	2
Crucible	(1-64)	1	5	1	4

The second is to use PECVD to deposit the insulating layer. And use CHA to deposit the conducting layer. We have tried to use CHA to deposit *20 nm* T/*300 nm* Au and use PECVD to deposit *1 um* SiO_2 or *0.5 um* SiO_2. The benefit is that we can deposit very thick layer SiO_2 to prevent the possibility of Au particle diffusing. The concern is the thick SiO_2 layer may cause stress issue. We can check the stress after the SiO_2 is deposit. *0.5 um* SiO_2 should be a good choice, but we may still have the Au diffusion problem. The way to check is adding a tape on the Au layer for pinhole density check after the process is done (Fig. 32)

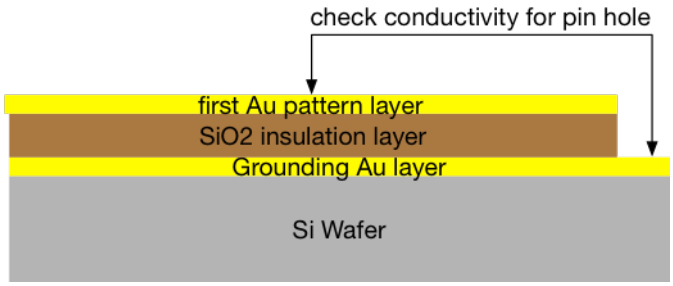

Figure 32 The demonstration of the pin hole check

Since the sidewall connection and the gold particle diffusion seem to be the two biggest challenges, we come up with another plan, instead of using very thin (*100 nm -200 nm*) sidewall connection, we can FDRIE the Si wafer to the grounding gold layer, and then use conductive polymer to connect with the gold layer without any problem. For the FDRIE of the silicon, we plan an oxide

hard mask on the backside of the silicon, then etch down and use gold as an etch stop. And to prevent the gold diffusion, we can deposit diffusion stop layer such as TiW. But both methods require us to design a mask and the fabrication would become more complicate. We can use this as a backup plan when we have run out

4.4.2.3.2. backside grounding layer

We can deposit the backside of the silicon wafer with a conducting layer, e.g. Au, and then easily connect this conducting surface with the grounded sensor board area.

4.4.2.3.3. use conductive silicon wafer

A similar way to the backside grounding layer is to use a conductive silicon wafer and then directly connect the backside of the wafer to the grounded sensor board area. It is easy and cheap at first though. Then we found that we cannot use thermal oxidation as the insulating method anymore, because the backside wafer will also be oxidized.

In conclusion, by considering all the three methods to make a ground (conductive) plane on the capacitive sensor, we have chosen the second method, which is as easy as depositing a gold layer on the backside of the sensor. To prevent the sensor being contaminated, we can deposit the gold layer the step after the silicon wafer get thermal oxidized.

Figure 33 The grounded sensor board and gold deposited assembled sensor

4.4.2.4. the conducting connection method

Now we have a conductive plane on the sensor and a grounding and conducting area on the sensor board, the final step is to come up a plan to make them connected.

First, it cannot be wires since we need a pristine surface for surgical tasks. Second, it cannot be rigid glue, because it will prevent the flexible polymer from moving with the applied force, and hinder the shear sensing performance and even the normal sensing performance. And third, it must to conductive for this signal connection. We have found the perfect product as conductive polymer; however, it has problems.

The first problem is it is by nature very thin, and with that thin layer, it is hard to have good conductivity. And second, it is hard to apply, most of the conductive polymer need inert environment to apply, which means glove box with nitrogen.

We have by far used three products. The first is conductive polymer PS:PTT (PH1000). The benefit of using this product is that the solvent of this product is water, which means we do not need glove box to apply it on our sensor, and it is comparably very conductive. However, it does not make our sensor has a grounding plane. By checking the conductivity of the sensor PCB board and the sensor surface, they are not connected.

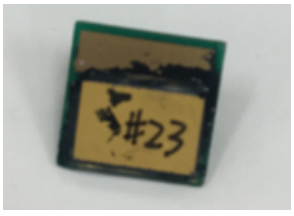

Figure 34 The sensor is contacted with the sensor board grounding area with PS:PTT, but not conducting

The second product is Poly (3,4-ethylenedioxythiophene)-poly(styrenesulfonate). To note, using this product we need to handle under inert and moisture free environment and use face shield and safety glasses, gloves, and complete lab suit at all times. After *24 hr- 48 hr* to let it dry, we can find that the sensor and the sensor board are successfully connected.

Figure 35 (left) The glove box which we applied the Poly (3,4-ethylenedioxythiophene)-poly(styrenesulfonate) (middle) the conductive polymer, the sensor, and the glass tube that used to apply the conductive polymer

The third method is the easiest and the one we chose to use right now, using silver paste. The downside of using silver paste is that the thin silver layer is easy to peel off and we need to check the conductivity of the surface every time after we applied. But since currently to prevent the suture slippage, we are attaching coarse surface to the sensor surface, the silver paste is safe in this way.

To check the performance of the grounding method we have applied in this section, we have designed and performed several measurements.

4.4.3. PDMS adhesion

PDMS adhesion has been a challenging task to address for clinical experiments. We cannot apply large shear force or the sensor would just fall off the sensor PCB board. By checking the fallen off

sensor and the sensor PCB board, we have figured that the problem comes from the poor adhesion between the PDMS and the gold electrode pads. And the problem must be solved since even the suture tying task would indicate large shear force. One commonly used surgical suture is silk 3-0 gauge, and it has a breaking force of *~20 N*.

The reason for lack of adhesion between PDMS and metal comes from the presence of a weak boundary layer (WBL) at the surface of PDMS. For instance, for PDMS, this WBL is expected to result from segregation of low-molecular-weight chains in the surface region. PDMS is one of the most unipolar materials, metals have an incredibly high surface tension, therefore metal layer does not stick.

4.4.3.1. fab related solutions

Fabrication related solutions include bombardment of the polymer surface by keV ions, laser beams, exposure to plasmas, chemical treatment and use MPTMS as molecular adhesive. The role of the plasma or ion-bombardment pretreatment is to eliminate the weak boundary layer via cross-linking.

We have applied the following methods to enhance the adhesion between the metal layer and PDMS.

The first method is use Ti or Cr as adhesion layer and then activate and hydroxylate the respective surfaces of the metal and PDMS by oxygen plasma or UV/O3 exposure in air. This is a common method for PDMS bonding and treatment, the plasma processing can help to improve the adhesion via etching or grafting of some functional groups. And The Handbook of Adhesives [137] (*p84*)

mentioned that chemical or electrolytic pretreatments of a bonding surface can greatly increase the strength of a metal, and form a highly adherent oxide. We need to pay attention to the temperature, time and power with the setup. And do the gold deposition as soon as possible after the treatment. But it did not work as we hope; the sensor still fell off the sensor board easily when we pushed a little harder.

The second method is to adjust the PDMS mixing ratio to be *10:1* instead of *5:1*. This method comes from a reference paper "experimental study of PDMS bonding to various substrates for monolithic microfluidic applications" and there is a table in that paper dealing with varying mixing ratio of uncured PDMS base and curing agent from *10:1* to *10:5* to investigate effects of average bond strength and standard deviation values of mixing ratio on different substrate (including gold). There is a tradeoff between the sensitivity and thickness. But the priority is to make our sensor work for larger force range. However, it was still not work as we hope.

The third method is to use MPTMS as molecular adhesive. This comes from a reference paper "Transfer of thin Au films to polydimethylsiloxane (PDMS) with reliable bonding using (3-mercaptopropyl) trimethoxysilane (MPTMS) as a molecular adhesive". From that paper, we learnt that we can prepare metal pattern on substrates, and then transfer to PDMS. But again, this method did not work.

The fourth method is to change gold to other bio-compatible metals/ alloys, hoping PDMS will have better adhesion with these metals/ alloys. Table 14 is a list of bio-compatible metals used in

medical applications. We have not tried this method before we moved to our next physical glue solution, detailed in next section.

Table 14 Bio-compatible metals used in medical applications

Division	Type of metal used
Cardiovascular	316L SS; CoCrMo; Ti; Ti6Al4V
Orthopaedic	316L SS; CoCrMo; Ti; Ti6Al4V; Ti6Al7Nb
Dentistry	316L SS; CoCrMo; TiNi; TiMo; Au, Ag, Pt and their alloys
Craniofacial	316L SS; CoCrMo; Ti; Ti6Al4V
Otorhinology	316L SS

4.4.3.2. glue related solutions

There are two categories of methods that we have designed and tried, indirectly and directly apply glue.

For indirectly applying glue, we have tried to modify our sensor PCB board to have 4 open holes at the four corners where we solder our sensor on with four different diameters. We tried to apply the super glue through the holes for better adhesion of the sensor to the sensor PCB board. However, this solution has one downside, exposing the pad to the surrounding environment, making it vulnerable to electric-magnetic waves and moisture.

Then we have considered using physical glue directly to apply between the sensor and the sensor PCB board. We have tried the following two materials. Devcon 2 ton epoxy No. 14310 and 704 silicon rubber sealant adhesive glue.

The result for sensor performance after applying epoxy glue in the version III circuit and sensor board using LabVIEW is listed in Table 15.

Table 15 Sensor performance after applying epoxy glue for the sensors with surface mount connector on the version II board using LabVIEW

version II result	z-normal	x-shear	y-shear
Force range (N)	5.1	11.1	11.85
Noise (fF)	0.836	0.247	1.442
Sensitivity (fF/N)	30.78	0.27	0.885
Resolution (N)	0.027	0.9	1.6

The force range for the normal direction is listed as *5.1 N* is because the linearity is from *0-5 N*, between *5 N* to *20 N*, there is a decreased sensitivity (loss of linearity) and we do not count that to be in the force range. While for the x-shear and y-shear direction, the sensor is always in the linear region, and the reason that the force range about *11 N* comes from the force applicator slippery after *11 N*. And the slippery comes from not enough normal force applied to hold the applicator. And it makes sense to get similar force range for the two shear directions because the normal force applied to the applicator is similar. The problem for using epoxy is that the linear force range for normal force is only 5N, not suitable for many surgical applications.

Then we have tried to use 704 glue, the result for sensor performance after applying 704 glue in the version III circuit and sensor board using LabVIEW is listed in Table 16.

Table 16 Sensor performance after applying 704 glue to the sensors with surface mount connector in the version III board using LabVIEW

version II result	z-normal	x-shear	y-shear
Force range (N)	11	12.4	12.2
Noise (fF)	0.868	0.255	0.087
Sensitivity (fF/N)	25.47	0.598	1.375
Resolution (N)	0.034	0.375	0.79

The force range for normal direction is also a linear force range, where we can apply normal force up to *20 N* for the normal direction, but the linear region is only *11 N*, better than epoxy. For x-shear and y-shear direction, it is the same reason: slippery prevent us to apply higher force.

From the above result, we can see that 704 glue has better performance than epoxy both from resolution point of view and force range point of view. And the reason for 704 glue has better performance is considered coming from its polymer-like structure. Thus, we are choosing 704 glue over epoxy for any further experiments.

The first is to run the calibration again with Arduino board, and compare with the sensor board that has no glue applied with both SMT connector sensor board and through hole connector sensor board. Here is the result.

Table 17 The sensor board performance with Arduino, comparing the with glue version and the no glue version for previous through hole connector sensor and SMT connector sensor

Resolution Performance (N)	Normal	x-shear	y-shear
SMT connector sensor with glue	0.004	0.268	0.127
SMT connector sensor with no glue	0.006	0.09	0.133
Thru hole connector sensor with no glue	0.055	0.25	1.45

From the table, we can see that the sensor board with 704 glue applied has worse performance than with no glue applied. It makes sense that there is degraded performance when glue is applied, but now we have much higher force range than with no glue case. It is a trade-off we need to consider. And right now, the force range is more important to think of than the resolution. The table also shows that even though, there is degraded performance than no glue version with SMT connector sensor board, it is still better than the version II with through hole connector sensor board no glue version, thanks to the increased noise performance that we have achieved from the SMT connector compared with the through hole connector version.

In conclusion, it is a good practice to add glue to the sensor board for gaining larger force range, with a little compromising the sensitivity performance. We are adapting this method to our final PCB board version III.

4.4.4. Water-resistant

Considering ex-vivo and in-vivo experiment in the long term, a waterproof seal is required in order to keep blood from entering the sensor. Researchers have shown success involving

force sensing with rubber materials [138] and we have incorporated it in our proposed force sensor design to address this issue.

4.5. Functionality Testing

This section deals with data acquisition and analysis on the collected data. Including developing an algorithm for configuring AD7746 and acquiring the stored digital capacitance data from it. The LabVIEW code is mainly to convert the data we can obtain from the CDC chip registers to the normal and shear capacitance value we want and then convert to the normal and shear force, which is the value of interest to our collaborators, the surgeons. The customized user interface is shown in Fig. 35, where we have three graphs each representing the normal cap code (*z* direction) and shear cap code (*x* and *y* direction) in hexadecimal system. On the right side, we have numbers indicating the capacitance code in hexadecimal system, in pico-Farad unit and finally, in newton system.

Figure 36 Screenshot for LabVIEW program user interface for testing AD7746

In order to prevent losing data, we need to wait until the conversion is complete, which requires *1 ms*. Also, there are two conditions when we need to stop, one is timeout the other is when we have

a register error. In the diagram, another block diagram is embedded in, which is the read register diagram.

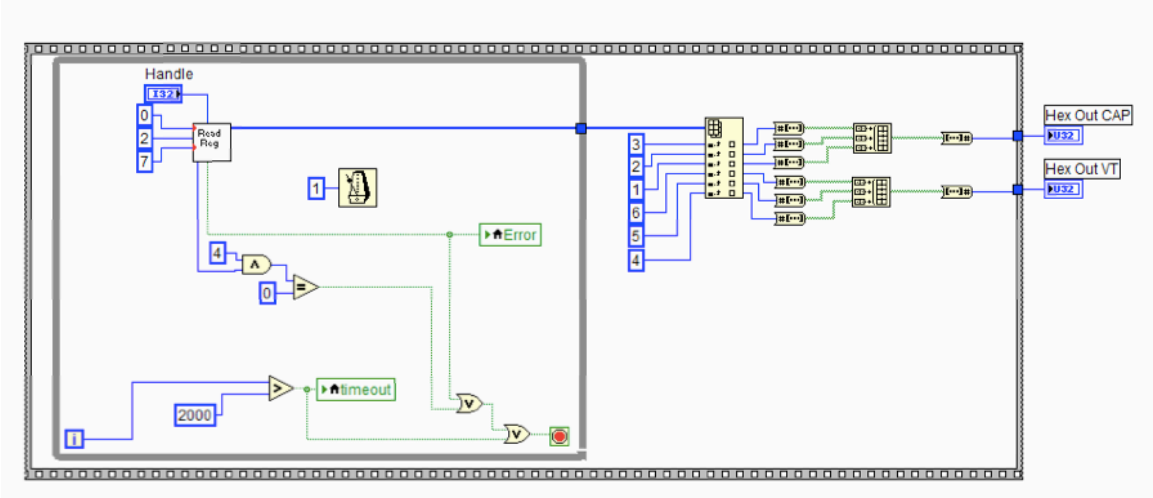

Figure 37 Screenshot for getting Hex output capacitance and voltage value diagram.

We can write to or read from all the CDC chip registers except the address pointer register, which is read only and has a total 19 address pointers, representing capacitance data, voltage data, cap offset, cap gain, configuration, voltage setup, excitation setup etc. The address pointer register determines which register is next to perform an operation, write or read.

The read register diagram is shown blow, where we take the register address, length of the buffer and if it is *24* or *16* or *8* bit information as inputs (2 is for *24* bit, 1 for *16* bit and 0 for *8* bit) and output Hex byte *0,1,2,3*. As can be seen from Fig. 46, the input value for the read register is *0, 2,* and *7*. Now we can understand without question that 0 is for register address, 2 is for *24* bit data retrieval, and *7* is for the buffer length. Details about the program are not included here for brevity. Just as one example, the number *90* in the graph below is caused by the reason that the start address for the CDC chip is 0x90 for a write and *0x91* for a read. Another thing worth mentioning is to reset the board before read the registers. If reset is successful, the status indication should be 7. If

this is the case, we can read all other registers. Otherwise, an error light shows up and we need to set all the registers to be zero.

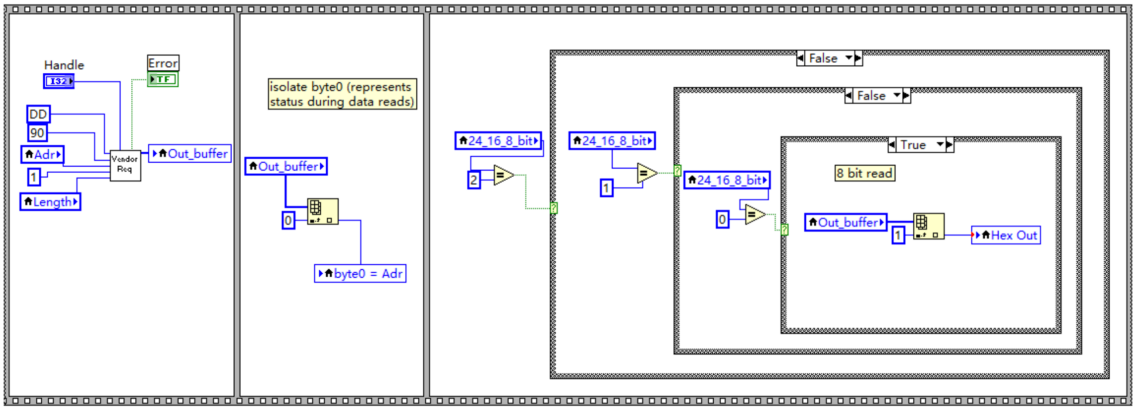

Figure 38 Screenshot for read register diagram

After getting the capacitance code, we can get the capacitance data from a simple conversion, and next, the RMS capacitance data and peak-to-peak capacitance data are known as well.

$$cap = \left(\frac{avg\ code - 800000}{800000} \times gain - offset\right) \times range\ pF$$

$$RMS\ cap = \frac{RMS\ code}{8388608} \times gain \times range\ pF$$

$$pk - pk\ cap = \frac{pk - pk\ code}{8388608} \times gain \times range\ pF$$

With this information, we are able to calculate the real-time RMS resolution and peak-to-peak resolution for the capacitive sensor, displayed in Fig. 39.

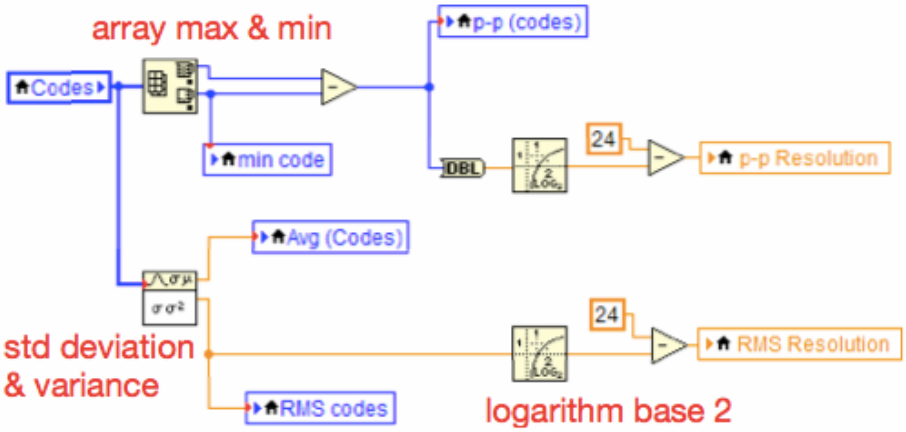

Figure 39 Screenshot for capacitance resolution calculation

In our experiment, the noise level is acquired at the beginning of the measurement to get noise analysis for a one-time testing. Then, the sensitivity value will be calculated for further real-time measurements to give us the measurement resolution. As shown in Fig. 40, after getting continuous samples, with the function of calculation unit, we can convert capacitance code to capacitance value, then, the force value can be calculated accordingly as well as the resolution, which is noise divided by sensitivity.

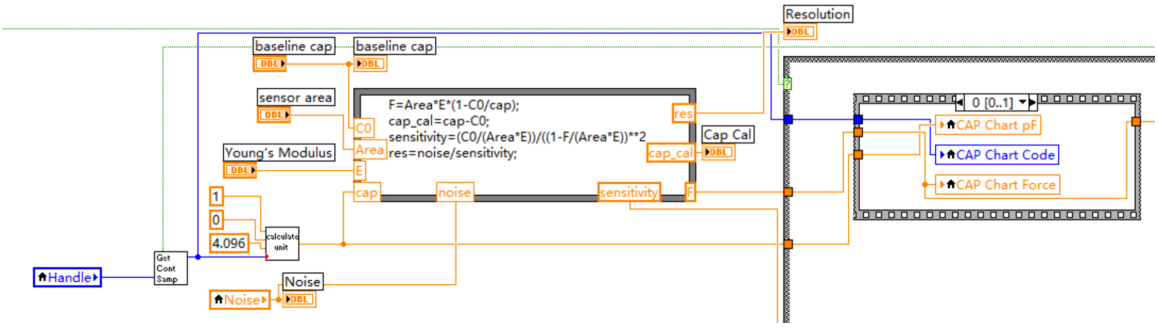

Figure 40 Screenshot for normal force calculation, sensitivity and resolution output schematic

1. input sensor parameters: center plate size, side plate size, sensor area, thickness of PDMS, Young's modulus, relative permittivity, and Poisson's ratio.

2. setup the register for our testing, whether we use channel 1 or 2 for testing, whether it is a single-ended testing or a differential testing, how you would you want the conversion time to be, and should it be in continuous mode or a one-time reading mode.

3. go to the analysis tab to get the baseline capacitance and noise performance.

4. go to the real-time tab, where after hitting the start key, we can watch the capacitance, force graph as well as their values simultaneously. The data for resolution is calculated for reference.

Figure 41 LabVIEW user interface

Chapter 5 Control Module

In order to visually interpret the tri-axial force data, we have created a Visual Studio application called HapticsManager.

5.1 Information Transmission

Communication protocols are rules or standards that allow a communication system to transmit information. For instance, Universal Asynchronous Receiver Transmitter (UART), Serial Peripheral Interface (SPI), Inter-Integrated Circuit (I2C), and RS232.

5.1.1 Communication Protocols

UART is one of the most used serial protocols. Most controllers have a hardware UART on board. It uses a single data line for transmitting and one for receiving data. Most often 8-bit data is transferred. There is no voltage level associated with UART, so you can have it at *3.3 V* or *5 V*, whichever your microcontroller uses. Note that UART is asynchronous communication, which means the microcontrollers which want to communicate via UART must agree on the transmission speed, the bit-rate, as they only have the start bit's falling edge to synchronize.

SPI is a simple serial protocol. A master sends a clock signal, and upon each clock pulse it shifts one bit out to the slave, and one bit in, coming from the slave. By using SS (Slave Select) signals the master can control more than 1 slave on the bus.

RS-232 is a serial protocol that is originally used for modems and teletypes. It is what is commonly called a serial port (or a COM port in MS-Windows). It uses ±12V levels for long distance communication.

The **I2C** protocol we used is a synchronous protocol which uses 2 wires, one for the clock (SCL) and one for the data (SDA). The master and slave send data over the same wire, controller by the master who creates the clock signal. The way it does is to use address for each slave.

5.1.2 Our Choice: I2C

The details for each of the mentioned protocols are summarized in the Table 18. With respect to the transmission (Tx) type, how many wires are used, the connectivity for each standard, the maximum (Max) speed, and application used in our daily life.

Table 18 Comparison for I2C, SPI, RS232, and UART (speed, connectivity, number of wires etc)

Standard	Tx type	Wire	Connectivity	Max speed	Application
I2C	synchro nous	2. SDA, SCL	Multiple masters, multiple slaves	1 MHz	Communications between processors
SPI	synchro nous	4. SCK, MISO, MOSI, SS	Single master, multiple slaves	75 MHz	Programming the processor SD memory cards
RS232	asynchr onous	2. Tx and Rx	Single-ended point to point	128 kbits/s	Computer terminals
UART	asynchr onous	2. Tx and Rx	Single-ended point to point	128 kbits/s	Diagnostic display

The reason we choose I2C protocol is: first, even though most I2C devices communicate at *100 kHz* or *400 kHz*, modern I2C specifications support up to *3.4 MHz* clock speed.

Second, the receiver always sends feedback to the transmitter (ACK) conveying a successful transmission, which leads to higher noise immunity. Third, unlike SPI, I2C can support a multi-master system, allowing more than one master to communicate with all devices on the bus. The most important reason is, I2C requires least number of wires (two wires) to perform serial data transfer, making the circuitry simple, but those two wires can support multiple (in our case, up to 127) slave devices. In general, I2C is a multiple master, multiple slave protocol (Fig. 42).

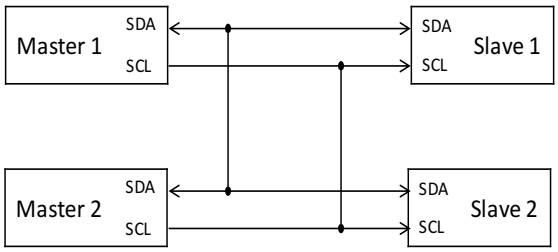

Figure 42 I2C is a multiple master, multiple slave protocol, redraw from [139]

Any number of data bytes can be transferred from the transmitter to receiver between the Start and the Stop conditions. The master sends out the Start sequence (S), followed by the *7-bit* Salve address and the $R/\overline{W}$ bit, indicating whether the next byte(s) will also come from the master of should come from the slave. The Slave acknowledges the address (A). Depending upon the value of the $R/\overline{W}$ bit, read/write operations are performed. When a slave receiver is addressed, it must generate an acknowledge (A) after each byte is received. Similarly, the master must generate an acknowledge after each byte that it receives from the slave transmitter. A master receiver signals an end of data to the slave transmitter by not generating an acknowledge ($\bar{A}$) after the last byte has been sent to the slave. The entire process repeats again, until the Master decides to Stop (P). The data transmission process is illustrated in Fig. 43.

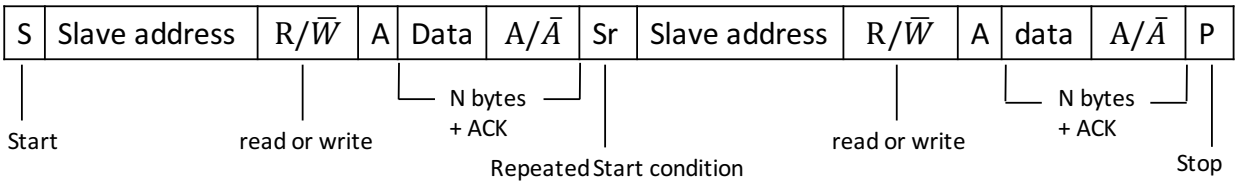

Figure 43 The I2C protocal data transimission process in a flowchart view.

5.1.3 I2C and Arduino Due

5.1.3.1 I2C address in Arduino Due

The I2C interface is extremely useful for connecting multiple devices, as they can all share the same two pins. This is because the devices are "addressable". Each device needs to have a unique address.

For the Arduino Due board, the slave address is a *7-bit* address, thus is in the range 0 to 127 decimal (*0x00* to *0x7F* in hex). However addresses 0 to 7, and 120 to 127 are reserved.

If a device has an address number larger than *127 (0x7F),* then that is the 8-bit address, which includes the read/write bit. We need to divide an *8-bit* address by two (shift right one) to get the correct address for the Wire library. For example if a datasheet says to use address 0xC0 for writing and 0xC1 for reading, that includes the read/write bit. Drop the "1" and divide by two, giving the "real" address of 0x60.

5.1.3.2 baud rate

The baud rate specifies how fast data is sent over a serial line. It's usually expressed in units of bits-per-second (bps) [140]. The higher a baud rate goes, the faster data is sent/received, but there are limits to how fast data can be transferred. You usually won't see speeds exceeding *115200* - that's fast for most microcontrollers. Get too high, and you'll begin to see errors on the receiving end, as clocks and sampling periods just can't keep up.

Baud Rate Mismatch—if two devices are not communicating at the same speed, data can be either misinterpreted, or completed missed. For the system debugging, when we find confusing data from all the receiving devices, we need to check to make sure the baud rates match up.

5.1.3.3 signal levels

I2C allows the connecting devices have different I/O voltages [139].

In general, in a system where one device is at a higher voltage than another, it may be possible to connect the two devices via I2C without any level shifting circuitry in between them. The trick is to connect the pull-up resistors to the lower of the two voltages. This only works in some cases, where the lower of the two system voltages exceeds the high-level input voltage of the higher voltage system–for example, a *5 V* Arduino and a *3.3 V* accelerometer.

5.2 Arduino Due Board

Arduino is an open-source platform used for building electronics projects. Arduino consists of both a physical programmable circuit board (often referred to as a microcontroller) and a piece of software, or IDE (Integrated Development Environment) that runs on your computer, used to write and upload computer code to the physical board [141].

Arduino Due is an Arduino board (shown in Fig. 26) which is based on a *32-bit* microcontroller with 54 digital input/output pins, 12 analog inputs, 4 *UART*s (hardware serial ports) and an 84 MHz clock. The provided sets of digital and analog I/O pins enable interfacing to our current

circuit using I2C serial communication. It also includes USB connection for loading program from personal computer to the board (see the programming port in Fig. 44).

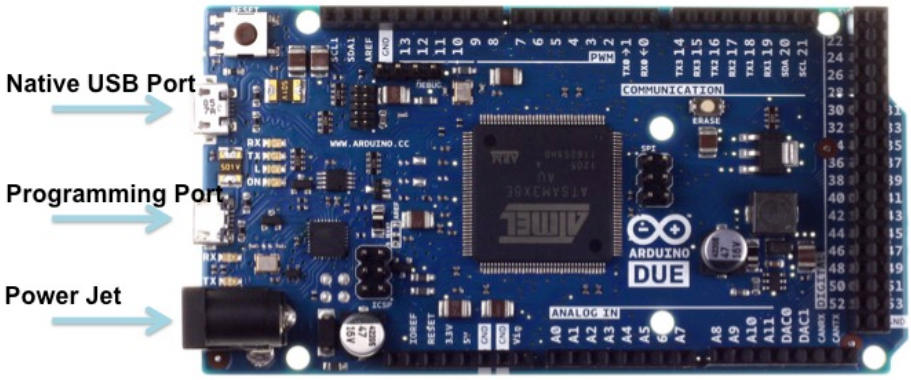

Figure 44 Arduino Due Board

As mentioned in previous section, in our case, the data acquisition includes, first, the capacitive sensor which can convert physical parameters into electrical signals, and next, a Capacitance-to-digital Converter (CDC) circuit, which can convert electrical signals into a form which can be converted to digital values. Our readout circuit encompassed two high resolution AD7746, which were implemented on a printed circuit board (PCB). Despite the fact that AD7746 can sample capacitance with discrete frequencies up to *90 Hz* it is applicable for single channel measuring only. Continuous mode with simultaneous sampling both channels is not possible by default by AD7746 since all the AD7746 chips share the same IP address. However, the I2C protocol relies on the fact that each device you connect as a unique address. Connecting multiple identical CDCs with the same permanent address would creating a conflict.

In this situation, there is no way to differentiate data from normal stress capacitance from one chip with data from shear stress capacitance from another chip. This problem was easily solved with

the use of an I2C multiplexer (MUX). A multiplexer is a device that can select one from many analog or digital inputs and forwards the selected input into a single line.

For our application, a commercial available chip Texas Instruments TCA9548A [142] was used to switch among the three-directional data and pass on to the microcontroller for further control and analysis. The bidirectional I2C bus consists of the serial clock (SCL) and serial data (SDA) lines. Both lines must be connected to a positive supply through a pullup resistor when connected to the output stages of a device. Data transfer may be initiated only when the bus is not busy.

The conversion time for one capacitance value can be set from *217.3 ms* down to *11 ms* at the compromise of higher noise, shown in Table 19 [136]. That is, *33 ms* ideal case for one *xyz* data packet. By taken the conversion time into consideration, and carefully chose the conversion time, we can minimize the noise and calculate the effective resolution from RMS noise.

Table 19 Typical capacitive input noise vs. conversion time [136]

Conversion time (ms)	Output data rate (Hz)	RMS noise (aF)	p-p noise (aF)
11.0	90.9	40.0	212.4
11.9	83.8	27.3	137.7
20.0	50.0	12.2	82.5
38.0	26.3	7.3	50.3
62.0	16.1	5.4	33.7
77.0	13.0	4.9	28.3
92.0	10.9	4.4	27.8
109.6	9.1	4.2	27.3

Figure 45 (a) shows a photograph of the controller board for the tactile sensing system. The multiplexer can be addressed by the Arduino microcontroller with the Wire library to connect and disconnect with the individual I2C lines of each sensor. The microcontroller was programmed to

get x-y-z data measurement, convert this to force values, and send out as a packet to the computer through the WiFi chip, where the computer will do the following signal processing and real-time data plot. The simplified system block diagram system is shown in Fig. 45 (b).

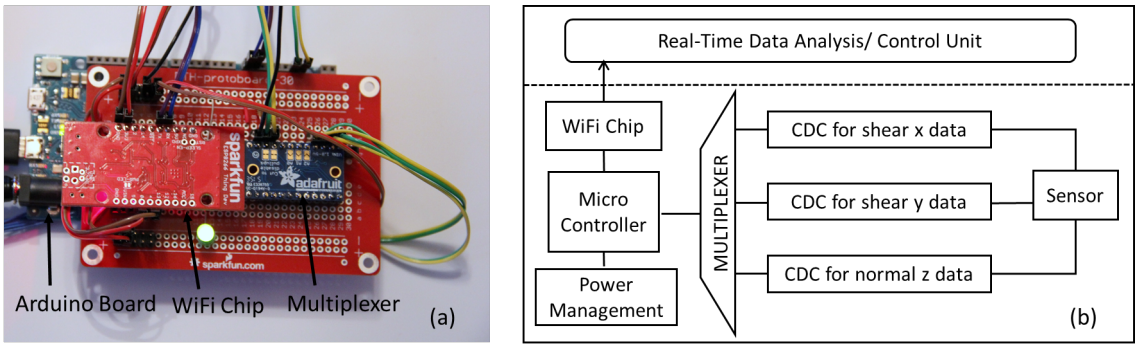

Figure 45 (a) The control unit of the tactile sensing system (b) system diagram for the tactile sensing system.

5. 3 Arduino IDE Coding

As for programming the microcontroller, the Arduino platform provides an integrated development environment (IDE) for all Arduino developers. To make things even simpler, we can use the "Wire" library in Arduino IDE. This library allows us to communicate with our I2C devices.

In order for the Arduino IDE to utilize its I2C capabilities, the following header file must be included.

```
# include <Wire.h>
```

The first step requires us to initialize the arduino loop known as

```
void setup()
```

This loop is the initialization stage of the arduino programming code where te initialization of variables, outputs, and things that only need to be run once, occur.

One function in this loop is Wire.begin(), which is a function that activates the wire.h library for initializing the I2C bus for the arduino.

Serial.begin() is another function that initializes the baud rate of the arduino software's serial monitor. This is necessary if we want to check that our code is working properly, as data will be streaming to this monitor.

Figure 46 shows the functionality we performed in the setup loop. First we initialize the WiFi transmission and setup the I2C bus baud rate to the fastest 115200. Then we perform the sensor initialization and set the current values to be 0 for all directions. Next, we perform the sensor calibration to get the baseline capacitance and variance for noise data for a dedicated number of sample points.

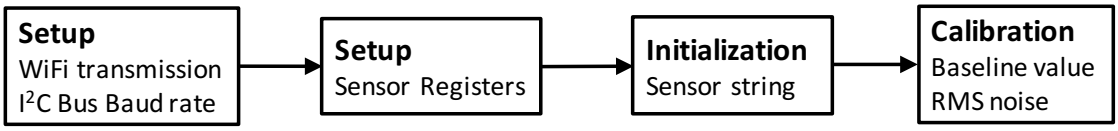

Figure 46 The flowchart demonstrating the functions we used in the setup loop.

Next comes the loop that will allow us to constantly read data from all three directions,

void loop()

which is the initialization of a loop that will continue as long as the Arduino board is powered. This is where all the data acquisition and also the switching between the sensors occurs.

For the master sending data to the slave we use:

```
Wire.beginTransmission (SLAVE_ADDRESS);
Wire.write (0x20);
```

One thing noted from the debugging process is: for the slave receiving data from the master, the receiveEvent is called from an Interrupt Service Routine (ISR), and we should not

a) Do serial prints
b) Use "delay"
c) Do anything lengthy
d) Do anything that requires interrupts to be active

Figure 47 shows the functions performed in the loop to constantly read x y z direction data and sending out to the custom HapticManager software. Firstly, we cleared the sensor values from the string. Then, we read sensor values directly from the CDCs. We transferred the data to a data conversion function, to convert the binary data to the capacitance data in fF unit. Then we calibrated for the new values taking account into the baseline capacitance and updated for the current values. Next, we generated the 3 direction force data packet in a form of Y[Z-data-byte][X-data-byte][Y-data-byte]Z in order to be easily sensed and analyzed by the master controller. Finally, we sent the data packet out through WiFi.

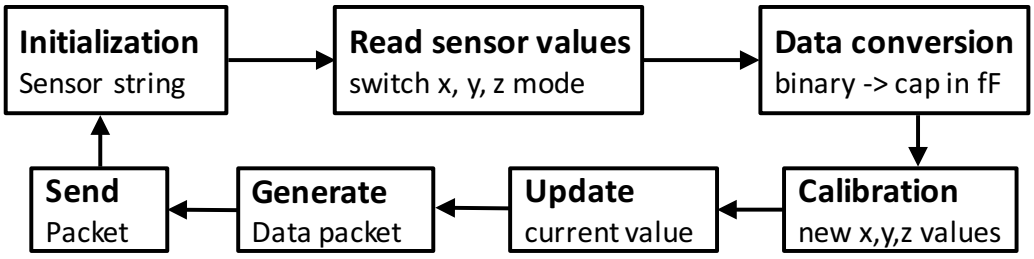

Figure 47 The functions performed in the loop to constantly read x y z direction data and sending out to the custom HapticManager software

The multiplexer has its own address that could be written to by the Arduino with the Wire library to connect (and disconnect) the individual I2C lines of each sensor.

5.4 Visual Studio Coding

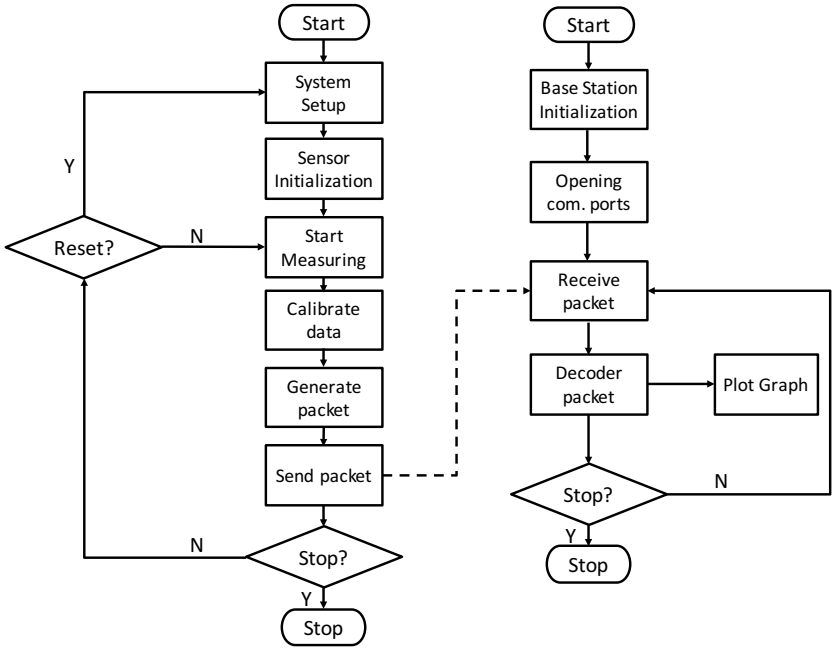

Figure 48 System flow chart

Figure 48 shows the system flow chart. The right side shows the functions performed by the custom computer software. After the data packets are generated and sent out through WiFi (detailed in

previous section as shown in the left side of the flow chart), the custom software on the computer received the packet, decoded the packet, and plotted the real-time data graph.

5.5. System Debug

The building of the system arouses lot of failure and debugging. I have summarized some debugging causes for future references. It includes hardware error, which will be detailed next, defect in A/D conversion, software error, failure of communication interface, human/software error and wire failure.

Table 20 System debugging summarize

Failure causes	**Failure modes**	**Failure effects**
Hardware error	Defect in D/A conversion	Incorrect output
Defect in A/D conversion, software error	Incorrect signal from sensor	Incorrect output
Software error	Conditioning of data from sensor is incorrect	Incorrect output
Software error	Corrupted signals to data processing or external system	Incorrect output
Failure of communication interface	Error on calibration	Incorrect output
Human/software error	Incorrect setting of parameters	Incorrect output
Hardware error	Loss of clock, wrong or changing frequency	Incorrect output
Wire failure	Loss of voltage to processor	Loss of signal history, calibration and settings info
Wire failure	Loss of voltage to sensor/ ADC	Loss or incorrect measurement of input signal
Wire failure	Loss of voltage to human interface	No display of data, setting of parameters not possible

Table 21 Concerns for sensor networks

Remaining issue	Short and long term drift	Sensor connectors & connections	Average reading of multiple sensors
Targeted issue	Operating temperature	Protective layer/ active protection	Data routing efficiency
	Energy consumption rate	Battery life, battery backup, uninterruptible power supply	Sensor accuracy requirements
	Data generation rate of sensor nodes	Response timings requirement	
Not relevant concerns	Sensor positioning in target area	Number of sensor nodes in the network	Individual sensor failures redundant sensor connection
	Corrosive environments		

When we got the final version III PCB, we can get the LabVIEW working, but no data display for Arduino, while the previous version II board still have data display with Arduino (same coding, same board). The debugging plan is made, as shown in Fig. 49. Things we have checked including coding (software), Arduino board (hardware), multiplexer (hardware), ribbon cable (hardware), circuit board (hardware), and sensor board (hardware). It is by far a complete checking list and we found where the error was.

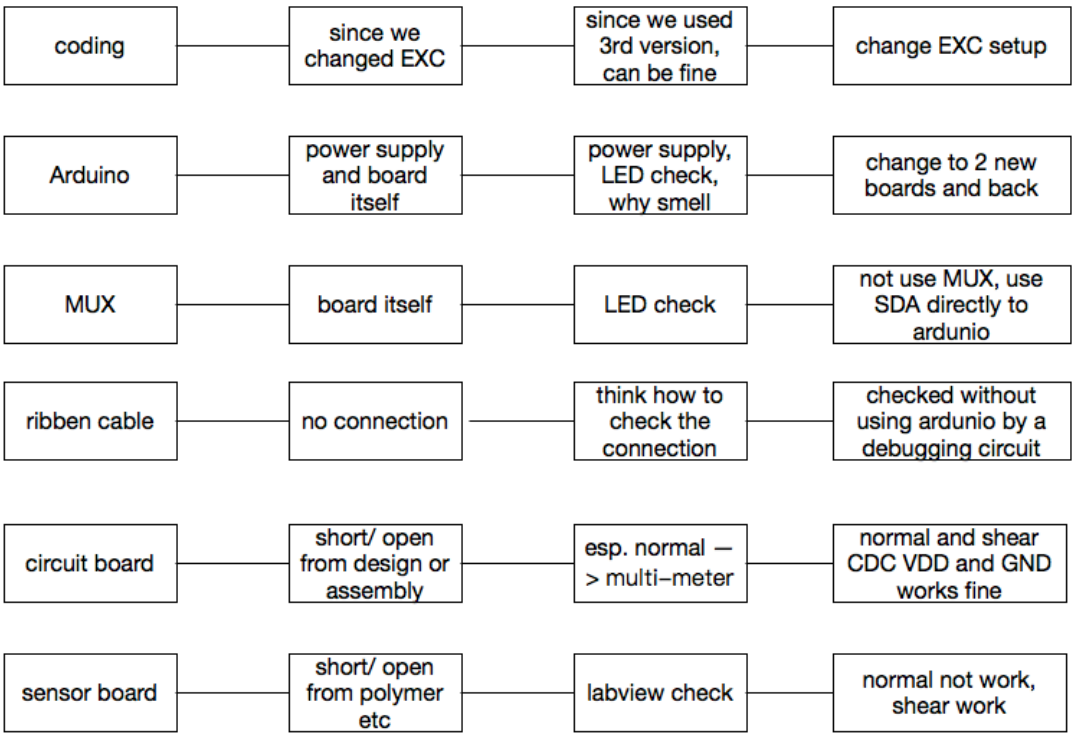

Figure 49 A complete debugging plan list to debug the Arduino system with the sensor board

And there are debugging books out there for references, such as "Why Programs Fail, Second Edition: A Guide to Systematic Debugging" [143]. Questions to consider, such as "can your device/IC even do the desired operation? (is it fast enough?)", "do you have any floating IC pins that should be tied to something –only pins labeled 'not connected' should be left floating; you must watch out for pesky enable pins that must be tied to the correct voltage" "did you accidentally destroy the IC/Device? –common for circuits involving a lot of power, and check circuit to make sure replacement won't also be destroyed".

Chapter 6 System Validation Results

A series of studies were conducted to evaluate the performance and effectiveness of the designed and developed sensing system in several applications for robotic minimally invasive surgery. Furthermore, these studies also aimed to better understand the benefits of the multi-axial force sensing system in robotic surgery. More specifically, these experiments were conducted as part of six major research investigations:

1. Investigation of the capacitance baseline (Section 6.1)
2. Investigation of the noise performance with different version boards and different software platform (Section 6.2)
3. Investigation of the force calibration with different version boards and different software platform (Section 6.3)
4. Investigation of the water-resistance method used in the newest version board (Section 6.4)
5. Investigation of thermal performance of the sensor under test (Section 6.5)

The system was evaluated by performing the following measurement.

6.1. Capacitance Baseline

Due to the parasitic capacitance variations in the system that cannot be controlled, a force is determined based on the measurement difference from "unload" capacitance measurements. The "unload" reference values are referred to as the baseline. To check the repeatability and reliability of the sensor fabrication process, circuit design and manufacturing, as well as the circuit assembly process, baseline capacitance values were examined by taking an average data from 5 trails for each sensor, where each trial was to average *100* data points at a *109 ms* conversion time for all *x,y,z* directions using custom LabVIEW program.

The noise performance is examined by taking root mean square (RMS) of unloaded sensor capacitance for the *100* data points. The noise discrepancy among the *x,y,z* direction is most likely due to difference in thermal noise, which is influenced by resistance of the electrical connections. Thermal noise is defined as $V_t = \sqrt{4kTBR}$, where k is Boltzmann's constant, T is absolute temperature, B is the *-3 dB* Frequency noise bandwidth, which is *8 Hz* for the *109.6 ms* conversion time in our case, and *R* is the resistance. The thermal noise is calculated to compare with the RMS noise value for each direction. To verify our theory, the same measurement was taken with *11 ms* conversion time (87.2 *Hz -3 dB* frequency bandwidth), to see if the result would scale in the expected manner.

Capacitance baseline values in x, y, and z for *18* fabricated and assembled sensors are shown below in Fig. 50. For the *x* and *y* directions, the baseline capacitance data should be *0* for the differential design. Besides the variance that caused by the fabrication and the assembly process, the discrepancy is mainly because of stray capacitance arising from the asymmetric circuit design (i.e., different trace lengths for the different directions). The stray capacitance for the *x* direction is calculated to be *0.487 pF*, while for the *y* direction it is calculated to be *0.0125 pF*, and are both consistent with the measured *x* and *y* values. An offset between *x* and *y* capacitance can readily be subtracted as long as the offset is constant over time and does not approach the dynamic range of the measurement circuit.

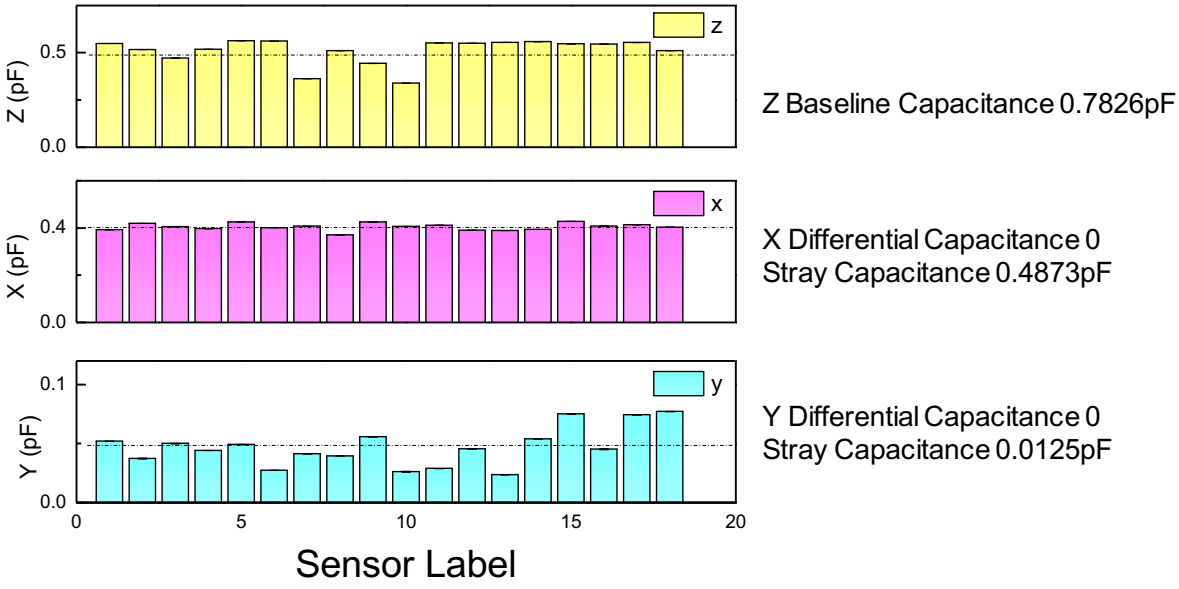

Figure 50 the measured sensor capacitance for three directions over 18 fabricated and assembled sensors. The dashed line in each graph shows the average number of the 18 measured sensors mean values

6.2. Noise Performance

6.2.2. Noise performance with version II board and LabVIEW

The noise performance is first examined by taking root mean square (RMS) of unloaded sensor capacitance for *100* data points with *109 msec* conversion time, resulting in *1.028 fF* RMS noise for normal-*z* direction, *0.309 fF* for shear-*x* direction, and *1.171 fF* for shear-y direction (shown in Fig. 51). Thermal noise is hypothesized as the cause for the noise discrepancy for the three directions. Supporting this hypothesis, the thermal noise attributed by the trace resistance is calculated to be *20.0323 pV* for normal-z direction, *2.96513 pV* for shear-x direction, and *18.3458 pV* for shear-y direction (Fig. 51). Plotting the calculated thermal noise and measured RMS noise in Figure 50, and they are sharing the same trend, suggesting the RMS noise is mainly caused by the thermal noise. To further support this hypothesis, the measurement, initially at *109 msec*

conversion time, was repeated with *11 msec* conversion time, yielding *3.404 fF* RMS noise for normal-*z* direction, *1.018 fF* for shear-*x* direction, and *3.390 fF* for shear-y direction, showing a ~ 3X noise performance for all three directions, as predicted by the square root of the increase of the bandwidth in the case of thermal noise.

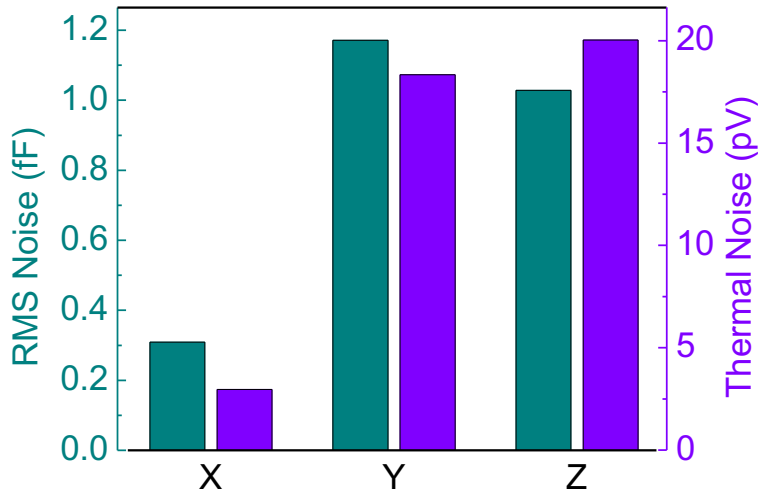

Figure 51 RMS noise for x, y, z direction compared with thermal noise calculated as $\sqrt{4kTBR}$ in x, y, z direction

Table 22 The noise performance tested by LabVIEW program and LabVIEW hardware with 109 ms conversion time and 11 ms conversion time

LabVIEW	z-normal	x-shear	y-shear
Noise (fF)/ *109 ms*	1.03	0.309	1.17
Noise (fF)/ *11 ms*	3.40	1.01	3.39

6.2.2. Version II board and Arduino

With a custom Arduino program using the fastest capacitance conversion setup, shortest mode

switching setup and shortest sensor switching setup, giving rise to a noise performance of *0.0942 fF* RMS noise for normal-*z* direction, *0.0786 fF* for shear-*x* direction, and *0.0826 fF* for shear-y direction, more than *3X* better than our previous best result [144].

Table 23 The noise performance tested by Arduino program and Arduino hardware board with the fastest conversion time and shortest delay time that can make accurate readings

Arduino (fastest)	z-normal	x-shear	y-shear
Noise (fF)	0.0942	0.0786	0.0826

We need to note that there is a trade-off between the data latency and the noise performance, with the fastest setup, we are getting the worst noise performance, but it is still more than 3X better than our previous best result.

In this setting, a data latency of less than *42 ms* was measured. For more details, see section 6.3.1.

6.2.3. Version III board and Arduino

Table 24 The noise performance tested by Arduino program and Arduino board with the lasted sensor board and adhesion method

Arduino (fastest)	z-normal	x-shear	y-shear
Noise (fF)	0.101	0.160	0.132

With the latest version sensor board, the noise performance is presented, we can see that all three directions have slightly worse performance due to the adhesion performance that we have used and the grounding methods been used. However, we can achieve much larger and more stable result as shown in Section 6.3.2.

6.3. Force Calibration

6.3.1. Version II board using LabVIEW/Arduino

Photographs of the normal force measurement setup and shear force measurement are shown in Fig. 52. As can be seen in Fig. 52 (a), we apply normal force directly to the sensor by a force gauge, pushing steadily with a manipulator and maintaining a normal direction using a custom 3D printed rail. As shown in Fig.51 (b), we apply shear force pushing on the side of a block while simultaneously applying a static normal force to prevent slipping.

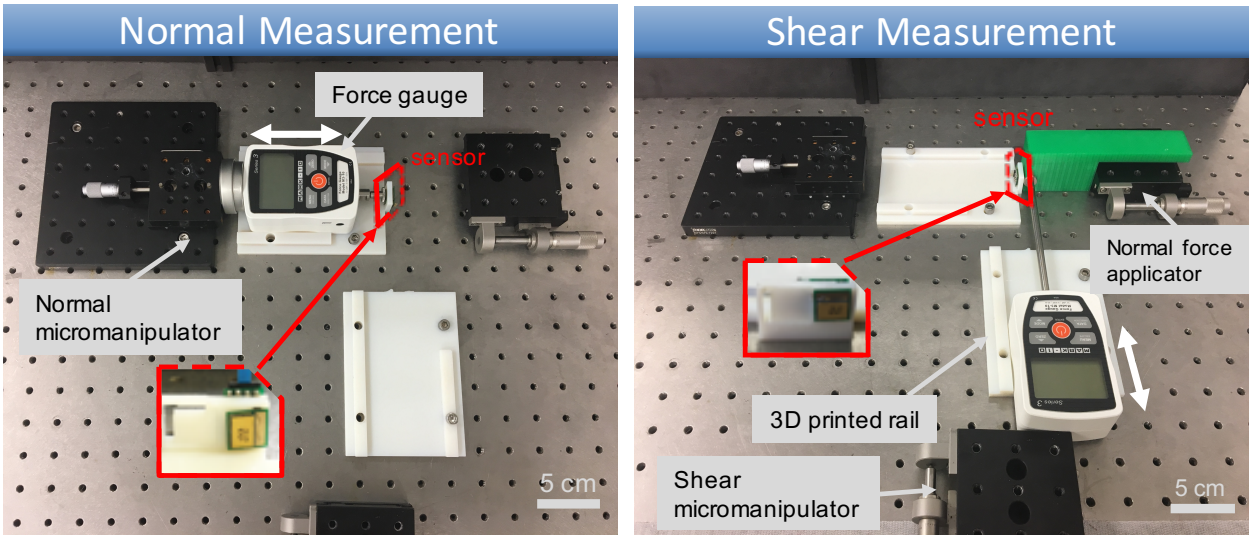

Figure 52 Experimental setup for measuring the capacitance with (a) applied normal force and (b) applied shear force.

The sensor was characterized with a conversion time of *11 ms*. At the start of each experimental trial, sensor data were collected with the sensor at rest in an unloaded state. After the baseline measurement of the unloaded state, capacitance was measured for a range of applied forces. The sensitivity of the sensor for each direction can be calculated by taking the slope of the measured data.

For real-time measurement, average capacitance data was calculated for a given load value, and

data points were plotted in Fig. xx for both normal and shear directions. The measurement was done with a custom Arduino program using the fastest capacitance conversion setup, shortest mode switching setup and shortest sensor switching setup, giving rise to a noise performance of *0.0942 fF* RMS noise for normal-*z* direction, *0.0786 fF* for shear-*x* direction, and *0.0826 fF* for shear-y direction, more than *3X* better than our previous best result.

A data latency of less than *42 ms* to collect a triaxial data package and transmit it to the computer through the Wired Ethernet for processing was measured. By taking into account a commonly achieved Wi-Fi latency in the clinical case of *1 ms* and a latency of less than *67 ms* from the actuators of the system, the total system latency should be less than *110 ms*. Studies show that it is desired to have a latency < *300 ms* [145] and it is required to have a latency < *500 ms* [146] to achieve desired performance.

Table 25 The system latency

	Sensor side	Actuator side
CDC conversion	*11x3=33 ms*	
Change of CDC status	*6 ms*	
Communication delay	*1x2=2 ms*	
Data processing delay	*1 ms*	
Total latency of the sensing system	*42 ms*	
Total latency of the actuator		*67 ms*
Total latency of the whole system	*109 ms*	

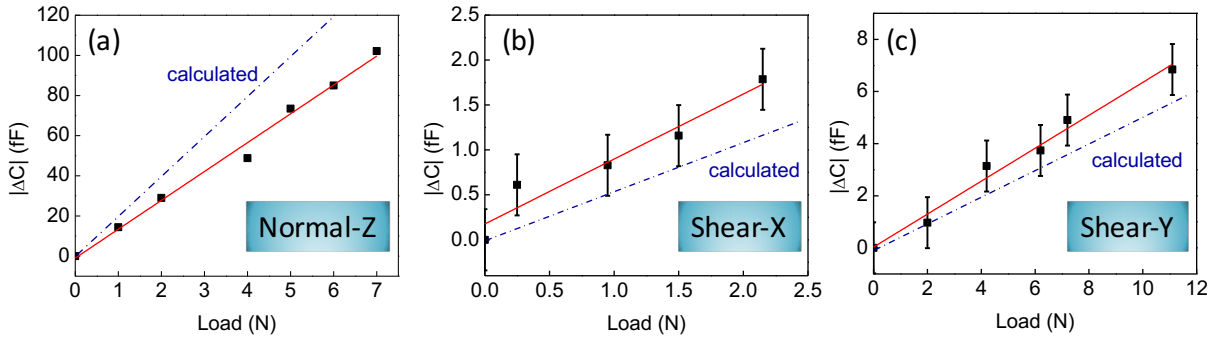

Figure 53 (a) The change of capacitance vs. the applied normal force (b) the change of capacitance vs. the applied shear x force (c) the change of capacitance vs. the applied shear y force by a force gauge. RMS capacitance data was used as capacitance error in the graphs.

Normal forces in the *1.5-4 N* range were shown to be relevant for inducing tissue damage [147], and shear forces as low as 8N were observed to cause suture breakage [148]. Our sensors operate in both of these ranges.

From the data graph shown above, the sensitivity for the normal *z* direction is measured by taking the slope of Figure 53 (a), calculated as

$$\frac{dC}{dF} = \frac{max - min}{force\ range} = \frac{0.102115}{7} = 0.014588 \frac{pF}{N} = 14.588\ fF/N$$

The discrepancy between *14.588 fF/N* and the theoretical *20 fF/N* lies mainly in the fabrication variance. Normal *z*-direction resolution is calculated by noise divided by its sensitivity

$$z\ resolution = \frac{noise}{sensitivity} = \frac{0.09423\ fF}{14.588\ fF/N} = 0.0065\ N.$$

By the same token, the sensitivity for the shear *x* direction is measured to be

$$\frac{dC}{dF} = \frac{max - min}{force\ range} = \frac{0.0017858}{2.15} = 0.0008306\ pF/N = 0.8306\ fF/N$$

And for shear *x*-direction resolution,

$$x\ resolution = \frac{noise}{sensitivity} = \frac{0.07855\ fF}{0.8306\ fF/N} = 0.0946\ N$$

The sensitivity for the shear *y* direction is measured to be

$$\frac{dC}{dF} = \frac{max - min}{force\ range} = \frac{0.12467}{6.5} = 0.01918\ pF/N = 19.18\ fF/N$$

As for shear *y*-direction resolution,

$$x\ resolution = \frac{noise}{sensitivity} = \frac{0.08257\ fF}{19.18\ fF/N} = 0.1328\ N$$

Sensor performance is summarized in Table 26. The discrepancy between the measurement value and the theoretical calculation for both *x* and *y* direction sensitivity is mainly attributed to variations in the fabrication process.

Table 26 Summary of sensor performance. Noise was calculated as RMS capacitance data for unloaded sensor over 100 data points, sensitivity was calculated as the slope of capacitance over load, and resolution was calculated as noise/sensitivity

Performance	z-normal	x-shear	y-shear
Noise (fF)	0.0942	0.0786	0.0826
Sensitivity (fF/N)	14.6	0.830	0.622
Resolution (N)	0.00645	0.0947	0.133

6.3.2. Version III board

The force calibration with the latest version III board is basically the same, but due to the fact that the board design is changed, the testing setup need to be modified. To reduce the 3D printer

material to be used in the future due to the design change, we have constructed a slide-in design where in the future only need to re-design and make the sensor holder part, and slide into the force gauge slideway.

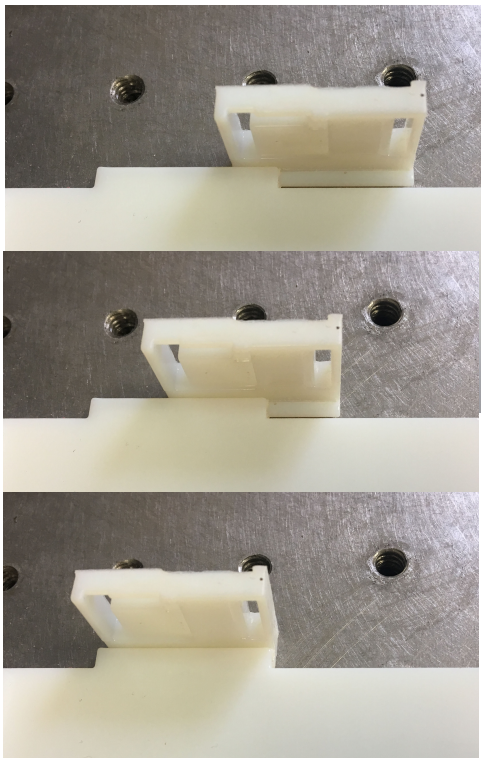

Figure 54 The slide in feature of the sensor holder for the testing setup.

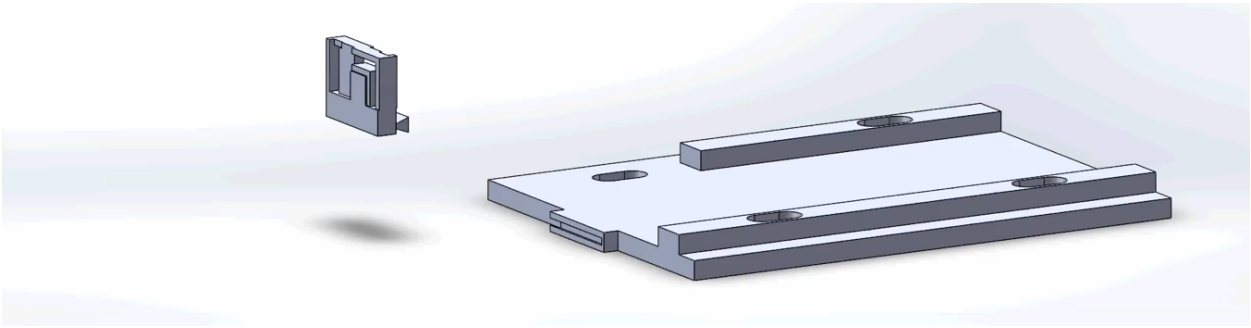

Figure 55 The slide-in design from solidworks

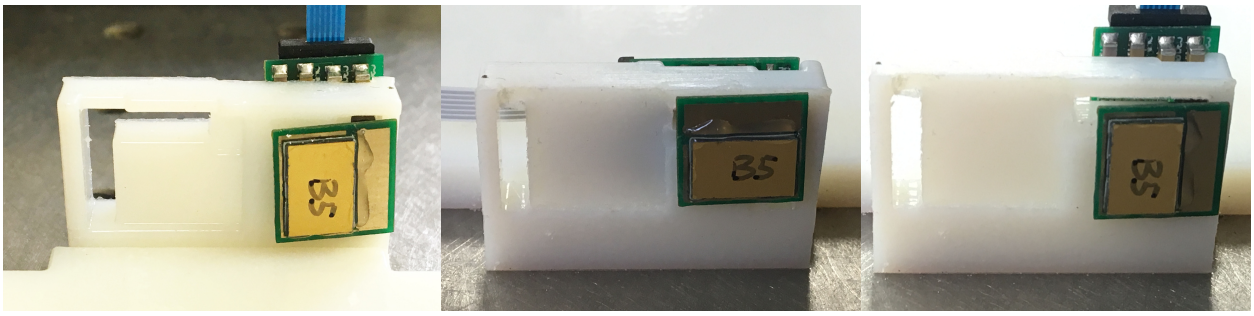

Figure 56 New design setup for normal-z, shear-x, and shear-y

With the improved adhesion between the sensor and the sensor board, now we can easily apply up to 20 N on the shear x, and y directions. The result is shown below.

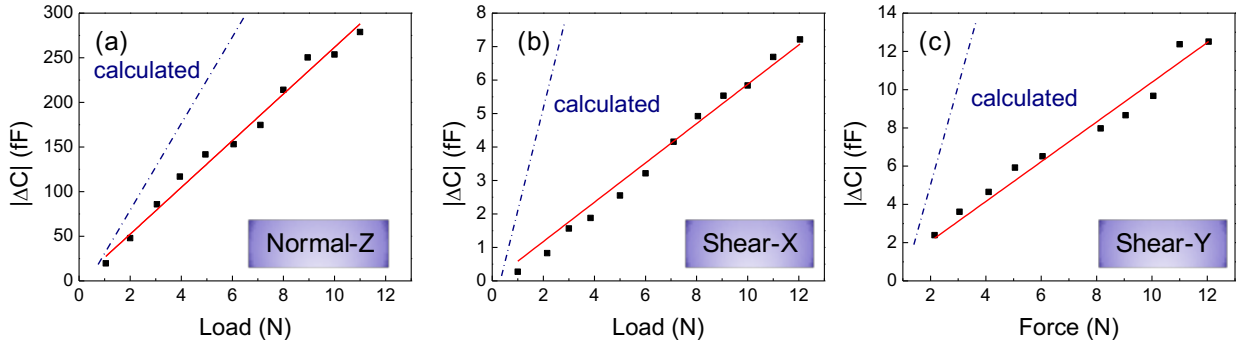

Figure 57 The force calibration result for the latest version sensor board with improved adhesion and miniaturized design.

The linear dynamic range can be considered as the resultant force of three axial force, calculated as $\sqrt{12^2 + 12^2 + 12^2} \cong 20.8\ N$.

Table 27 The summarized noise performance, sensitivity result, and derived resolution result

Version III result	Normal	x-shear	y-shear
Noise (fF)	0.101	0.160	0.132
Sensitivity (fF/N)	25.3	0.598	1.038
Resolution (N)	0.004	0.268	0.127

From the summarized noise performance, sensitivity derived from Fig. 56 and the calculated resolution we can find that we have much better improved physical dynamic range and slightly comprised resolution.

6.4. Water-Resistance Testing

Two water resistance measurements were carried out with our sensing system to examine the capability of the sensor system in liquid. First, capacitance and RMS noise values were taken before and after the sensor board and circuit board were fully immersed in water for one hour. Second, an underwater test was performed where the data was taken with the sensing system fully in water.

The sensor system survived the preliminary water test with no apparent degradation in performance, as shown in Fig. 58(a) and Fig. 58(b). This experiment shows that our sensor has the water rejection ability –the ability to completely recover after the liquid is removed. Fig. 58(c) shows the result for underwater test. It can be found that though the capacitance was changed from the baseline capacitance *0.48 pF* to *0.08 pF*, the values are very steady. The in-vivo test can be carried out with the sensing system by modifying the program to allow system reset to re-calibrate the baseline capacitance. More proficient under-water test would be performed soon.

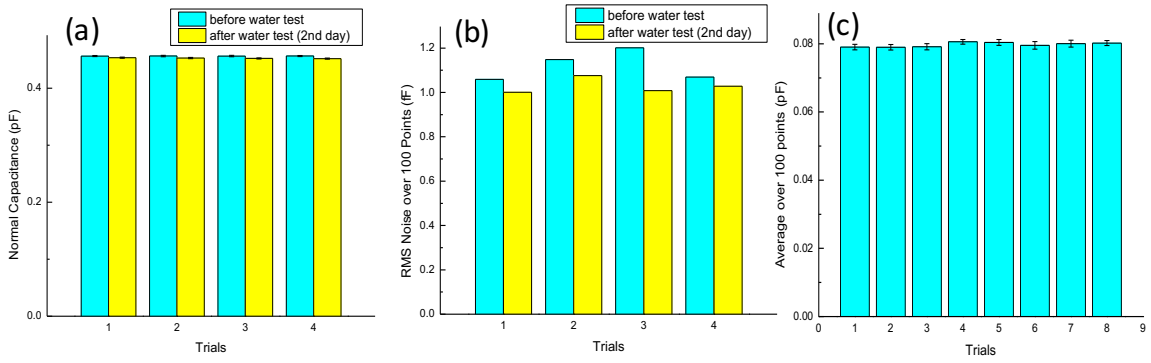

Figure 58 Sensor performance before and after the water test (a) normal baseline capacitance (b) RMS noise performance (c) in water test

6.5. Thermal Test with Final Version III Board for Shear Direction

It is believed that capacitive sensors are affected by temperature, capacitive sensors need some specialized design know-how to avoid this hazard. In order to account for any temperatures sensitivity of the capacitive sensors, we have carried out thermal tests with embedded internal temperature sensor to see if our differential design has the advantage as compensating the influence as we designed it.

A thermal measurement was carried out with our sensing system to examine the capability of temperature compensation using the differential design. First, a room temperature test was performed to get the baseline with the temperature sensor. The purpose of this step is to calculate the change of capacitance when doing the data analysis for shear-x and shear-y directions, and different sensor modes (differential or single). Then, the whole system is heated in an oven to a stable temperature, the heater is switched off, and the chamber is cooled down. At this point the sensor may be inspected any presence of temperature hysteresis (i.e., if there is any difference

between the results when temperature heating up, and cooling down and to verify the differential design helps to compensate for temperature variance).

We can test for both x-shear and y-shear directions with the setting be CH1 or CH2. And to verify if there is any beneficial for using differential design, we can test with both differential setting and single setting.

We used medium heating up setting for the oven, which is much faster than our precisely used slow setting and use *109 ms* conversion time for the sensor (*172 ms* effective update speed).
Test plan is as follows, for each sensor, there is an *8-step* test, if not run again:

1. Differential mode, CH2 (Y direction), ⬆ (heating up)
2. Single mode, CH2 (Y direction), ⬇ (cooling down)
3. Single mode, CH2 (Y direction), ⬆ (heating up)
4. Differential mode, CH2 (Y direction), ⬇ (cooling down)
5. Differential mode, CH1 (X direction), ⬇ (cooling down)
6. Differential mode, CH1 (X direction), ⬆ (heating up)
7. Single mode, CH1 (X direction), ⬇ (cooling down)
8. Single mode, CH1 (X direction), ⬆ (heating up)

Fig. 59 shows the single mode summary for the three sensors and both shear x and shear y (with CH1 represents shear x and CH2 represents shear y). From this we can find first, there is negligible temperature hysteresis for both shear directions and for all sensors, and second, there is a linear relationship between the capacitance change and the temperature change for both shear directions

and for all sensors. From the baseline values taken at room temperature, we can derive the change of capacitance with the change of temperature.

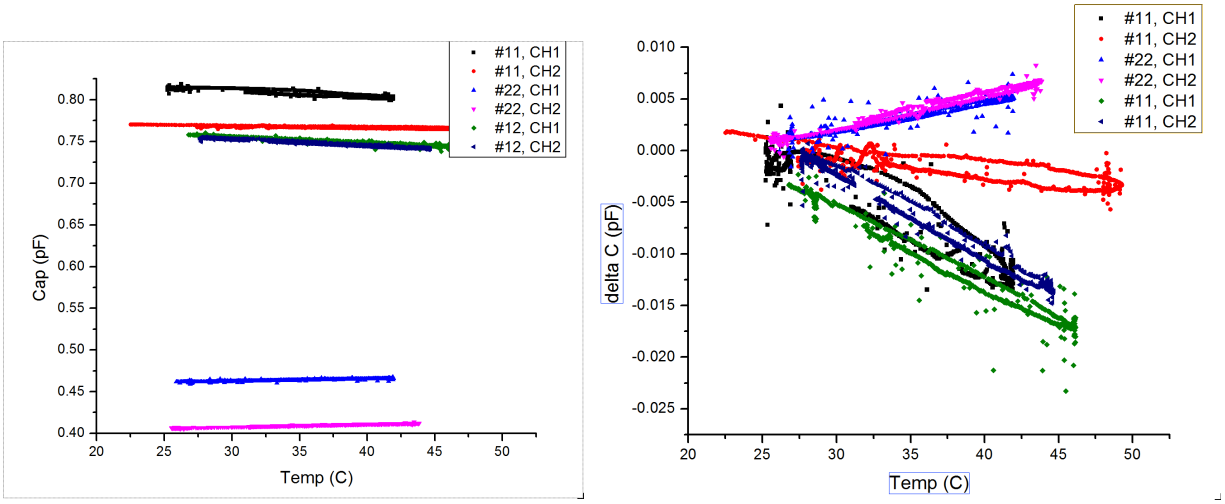

Figure 59 Single mode summary for both shear directions

Fig. 60 shows the results for a typical sensor #12, both differential shear directions and single pad shear directions, for both x-shear and y-shear. The result is as expected: differential shear result is better than single shear result –less temperature dependence. And it makes sense, since the differential design can compensate the temperature dependence of the materials.

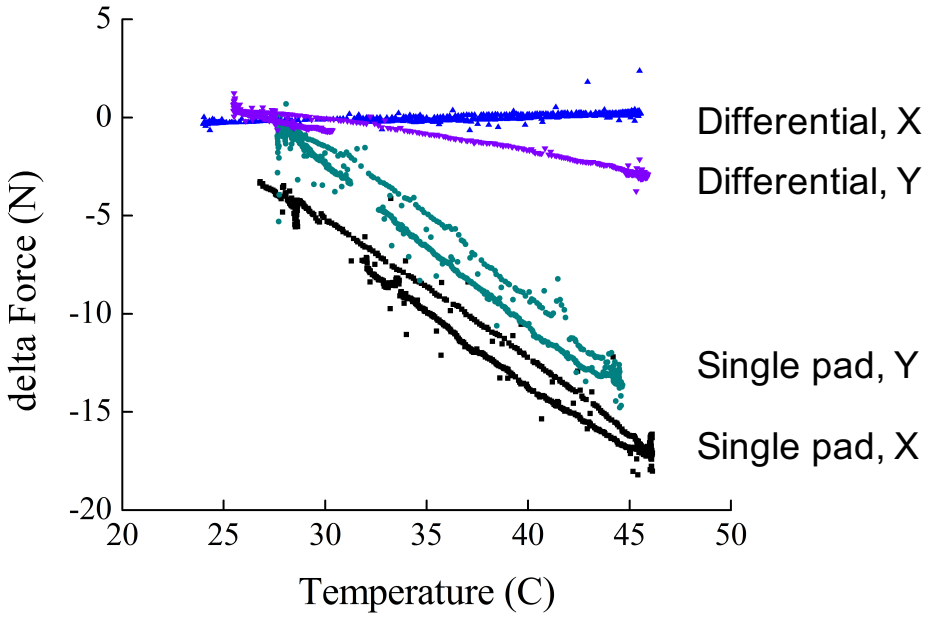

Figure 60 Thermal test result for sensor #12, we have results for both differential shear directions and single pad shear directions for both x-shear and y shear.

Chapter 7 User Study

7.1. Normal Force Test with da Vinci

7.1.1. Normal sensor with actuator

We have tried to use the normal force sensing to activate the actuator in the da Vinci [149]. We firstly modified our sensing capabilities to 5 discrete levels, and after communicate through the customized software, our sensor successfully activated the actuator to 5 discrete levels.

7.1.2. Peg transfer test

This study was set up to quantify the effects of tactile feedback on grip force. Shown in Fig. 61, the grip force can be recorded with the designed UI for a manual peg transfer task.

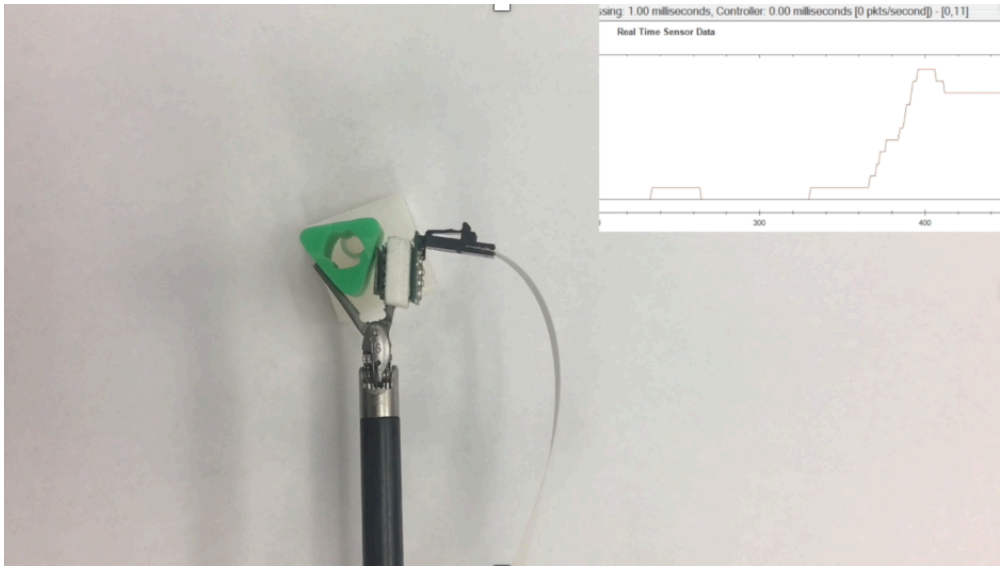

Figure 61 Hand controlled grasper doing peg transfer task, with normal force recording

Then we have used the da Vinci to perform a single-hand peg transfer task adapted from the Fundamentals of Laparoscopic Surgery (FLS) education module developed by the Society of American Gastrointestinal Endoscopic Surgeons (SAGES) with version II PCB. This experiment

showed the capability of our integrated normal force feedback system with the da Vinci surgical system. However, the stability of signal and restriction on the size posed challenges for us during the trials.

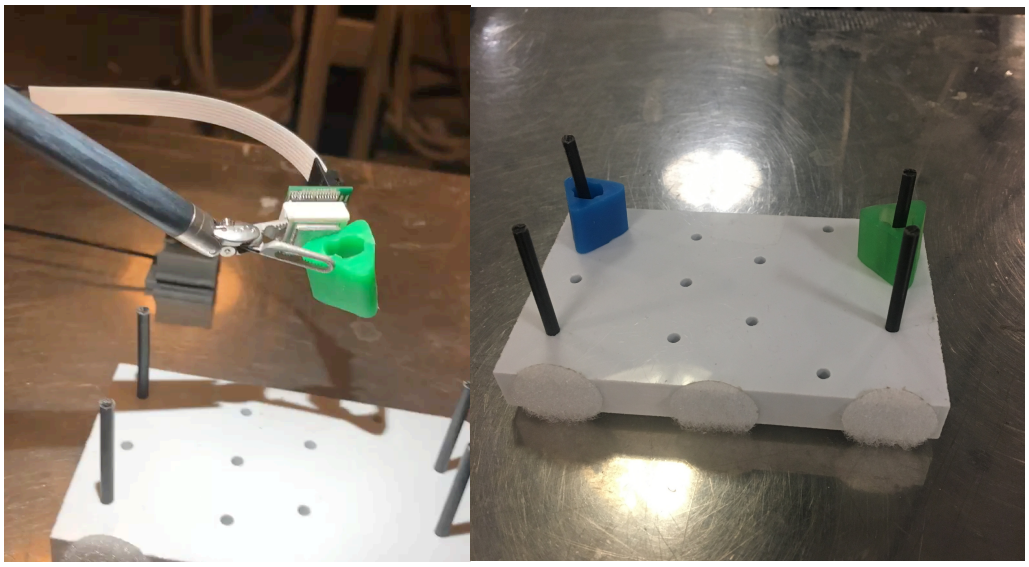

Figure 62 Peg transfer with version II PCB using da Vinci

With the improved version III PCB, subjects were asked to do peg transfer with and without pneumatic actuators. More subjects need to be recruited to complete the study to show if there is any significance in improved performance and whether the feedback system might hinder the task performance. The experimental setup can be seen in Fig. 63.

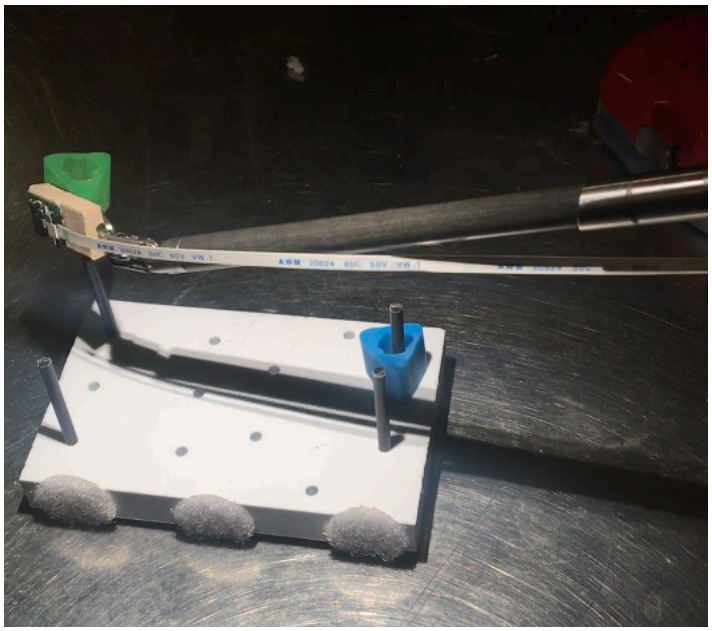

Figure 63 Peg transfer with version III PCB using da Vinci

7.2. Shear Force Test

Robotic surgery has become the most preferred approach for many surgical procedures as it offers distinct advantages compared with conventional minimally invasive surgery and open surgery since it has FDA approved in 2000 [24]. However, it has failed to provide comprehensive and effective tactile feedback to the surgeon, which can negatively influence the outcome of the surgery and is considered a major weakness in current RMIS systems [3].

Besides the well-understood normal force sensing, shear force sensing is also critical for clinical tasks, as it could prevent suture breakage and the slippage of tissue. In this paper, we will focus on the shear sensing feedback.

Large force concentrations at the tips of instrument graspers and limited depth perception have resulted in excessive frequent suture breakages [150-153]. When sutures are detected

intraoperatively, they can complicate surgical procedures and necessitate additional corrective measures [154]. When weakened sutures break inside the patient postoperatively, significant harm to the patient can result from peritonitis due to bowel anastomosis disruption [155] or hemorrhage from vascular anastomosis [156].

However, it does not mean that the surgeon should use minimal force during the suture tying procedures. The possibility of post-operative knot slippage is present when insufficient force is applied to tighten the knot, resulting in further risk to the patient.

As the popularity of robotically aided surgery increases, it becomes increasingly important to develop technologies that can warn surgeons when sutures are close to breaking [157, 158] while maintain good quality knots, improving the outcome of knot tying.

Previous attempts at predicting suture breakage have measured the strain in sutures with visual analysis, but these approaches are limited due to their dependence on image quality and specific visual cues [159]. Other approaches have used a visual overlay to relay force information to the surgeons control panel, but visual feedback has been shown to increase cognitive load and is not as effective as force feedback in reducing the applied force in certain applications [160-162].

In the part, we are going to explore the suture breakage, whether the normal and shear forces has any correlation and finally the suture tying experiment to see if our haptic feedback can help improve the result of clinical robotic surgery.

7.2.1. Suture breakage test

We have tested our sensor system to validate our shear sensing capability by a suture breakage test. In this test, we have place the suture in between the sensor and the force applicator, which is holding against the sensor by a force manipulator. The normal force applied to the sensor is kept the same by remaining the same amount of reading of the value on the force manipulator. One end of the suture is tied to the force gauge, by pulling the force gauge and record the largest force used during the test, we have the force value used to pull the suture to break. And we compare with the largest force recorded by the sensor, giving us the result shown in Fig. 64 (b), with the x-axis being the test run number. It is seen here the force used to break the suture is rather consistent, and the data from our capacitive sensor is rather convincing.

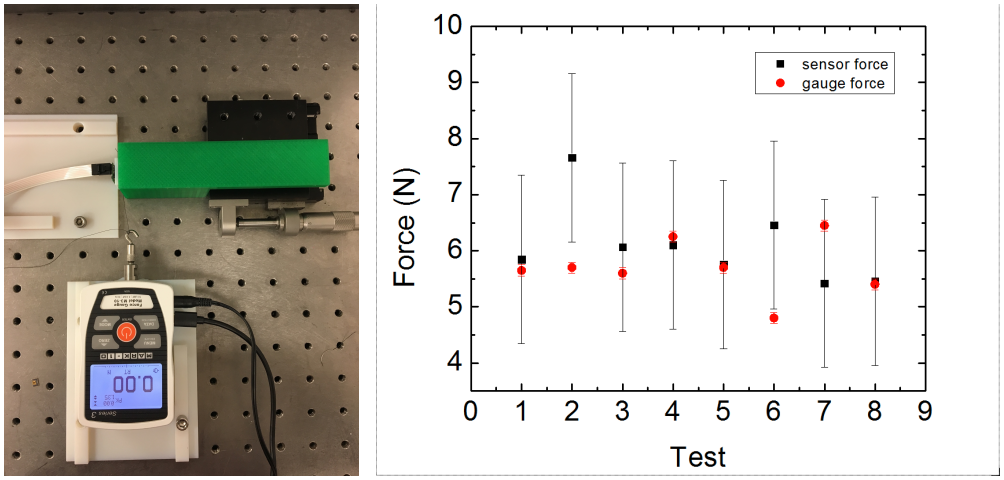

Figure 64 Suture breakage test with version II PCB with 5-0 suture (a) suture breakage test setup (b) results with recorded sensor force compared with the force recorded by the force gauge when tore broke

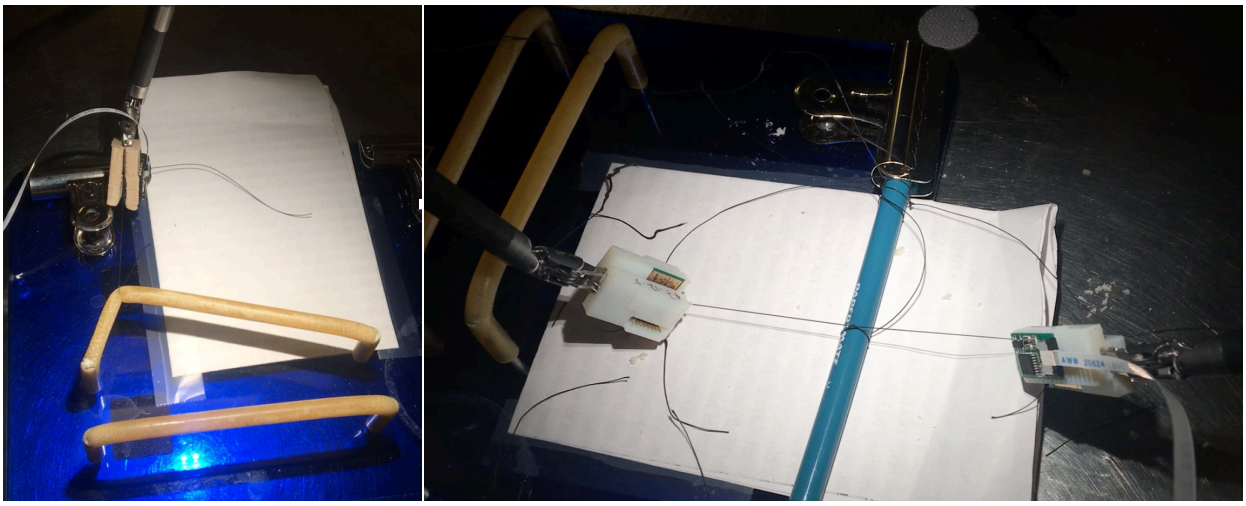

Figure 65 Suture breakage test with version III PCB with da Vinci

Suture breakage test using da Vinci with both normal force and shear force recording was performed. The 3-axial data was plotted in Fig. 66 (c).

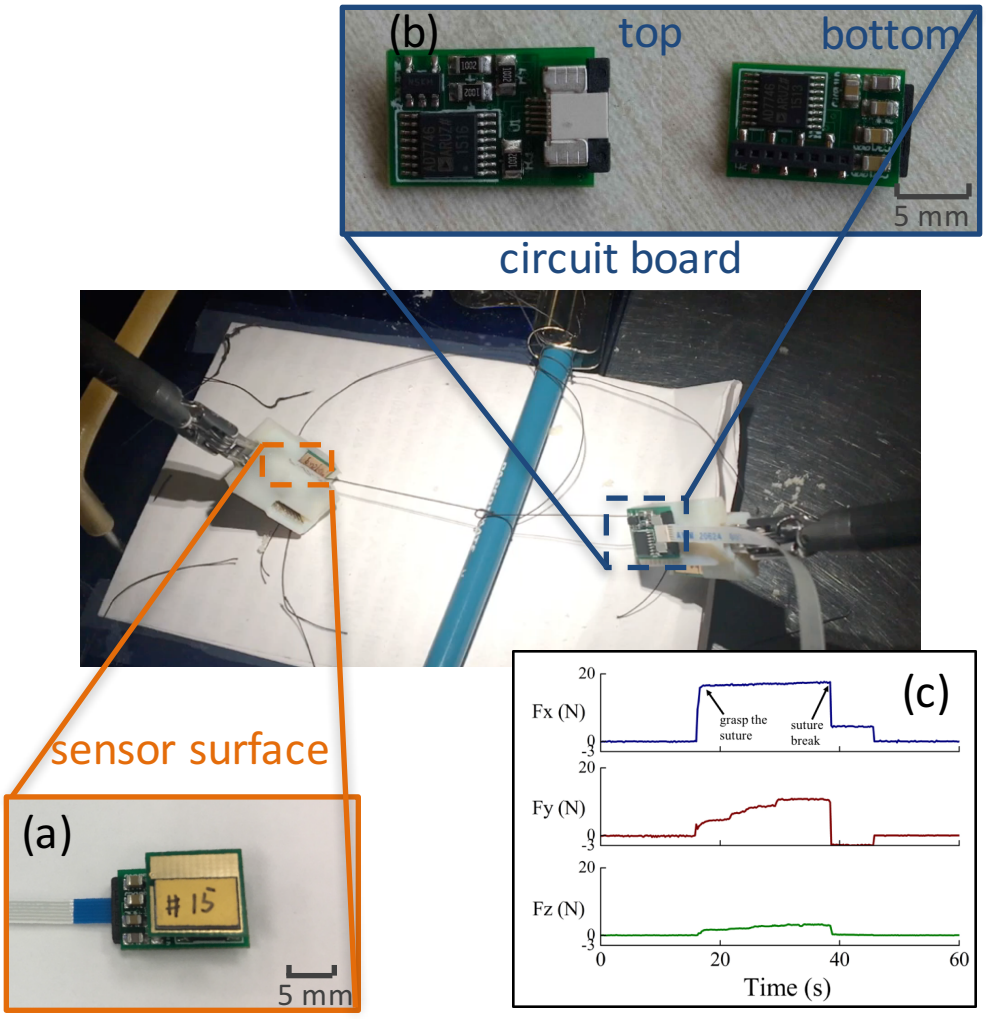

Figure 66 The surgical grapser-integrated force sensor performing knot tying and breakage tests. (a) sensor surface (b) front and backside of the circuit board (c) 3-axial testing result of knot tying and breakage.

7.2.2. Normal vs. shear test

Measurement plan: use da Vinci to tear the suture apart, record both normal and shear force.

Hypothesis: the larger normal force, the smaller shear force is needed to tear the suture.

7.2.3. Knot Tying Experiment

Suture breakage is common in knot-tying as the pulling motion introduces prominent shear forces. A shear sensor mountable on the da Vinci robotic surgical system's internal tension. HFS then provides vibration feedback as forces near a particular material's failure load.

The experiment is designed as follows:

- The number of suture breakages is recorded
- The knot fidelity is evaluated by measuring knot slippage (in mm)
- The time for complete the knot tying is recorded

Figure 67 Suture tying test

In prior work, our group designed and validated a vibrotactile feedback system with a uni-axial piezoresistive sensor [163]. A limitation of the uni-axial system is that the surgeon rarely pulls the suture in only one direction. More specifically, the actual tension in the suture is a combination of bi-axial shear and normal forces applied to the sensors. In this work, we seek to improve our prior design and develop a bi-axial shear sensor. This system is designed for integration onto the end effectors of robotic instruments and detects the applied force to sutures. Thus, a suture breakage warning system is constructed to reduce occurrences of suture failure by providing vibrotactile feedback when the measured tension approaches the suture's failure load. We hypothesize that such a system will reduce the occurrence of suture failures without negatively affecting the quality of knot produced during robot-assisted surgery.

Utilizing the developed shear sensors, a bi-axial shear feedback system was created that outputs vibrotactile feedback to the user while force is applied to sutures that nears the breakage force. This model is similar in method to our prior suture breakage study [163]. The configuration of the feedback system for this study is illustrated below (Figure 68).

Figure 68 The Shear Force Sensing Feedback System Flow Chart

The vibratory feedback system, described in greater detail in prior publications [163], was setup to provide two levels of vibratory feedback of increasing intensity. These vibrotactile feedback levels were attained by controlling the input voltage to an Eccentric Rotating Mass (ERM) vibration motor. This motor was mounted on the master controls of the da Vinci system in a manner

permitting contact of the operator's fingertips with the motor (Figure 70). The influence of other types of sensory feedback, including skin stretch, augmented reality, audio feedback, requires further investigation in the future.

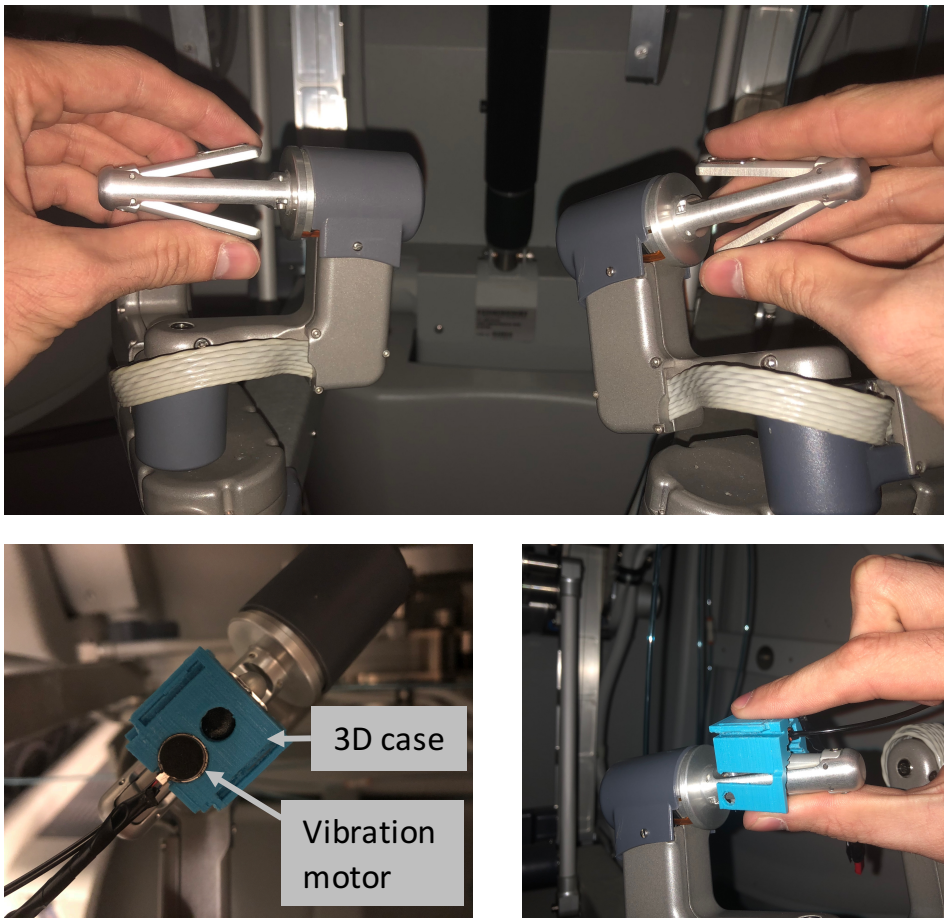

Figure 69 ***The mounted vibration motor on the da Vinci master controller (operator's hand in direct contact with the motor).***

Notably, the ultimate tensile strength of a suture depends on many factors (e.g., material, gauge, orientation, rate of applied tension, and potential material defect [164]). Silk 3-0 suture was used in this study. We have carried out a set of suture breakage testing to get a range of the breakage force value, which is consistent with result given in [164] of the Silk 3-0 sutures.

Based on user trials, feedback levels were varied in order to maximize the user experience (i.e., setting the timing of both the first feedback level to avoid unnecessary distraction and also the second level to provide enough time to respond before suture failure). Thus, shear force feedback was configured to provide vibration feedback to the fingertips of the operator at two levels of intensity for this study. The first level of vibratory feedback was activated at ~ 30 % below the failure load of the suture ($15\ N$ in [164]), and while the second level of higher intensity was activated at ~ 5 % below the failure load.

A total of 17 novice subjects were asked to tighten a knot by pulling on both free ends of the suture. Work with human subjects was approved by the Institutional Review Board (IRB) under protocol #11-000077. Each subject was provided with a setup containing ten knots, and HFS was enabled in an alternating fashion with the order of the trials randomized to avoid bias for HFS or no feedback trials. For each subject, five of the trials were tightened while HFS was enabled and five while HFS was disabled. A proctor set up the experiment by tying two knots in each suture in order to maintain consistency of tightness around a smooth, solid, cylindrical object, and then starting a third knot without tightening it. The subject was asked to tighten the third knot to replicate a surgeon tying multiple knots at the same location to ensure anastomoses stability. This approach also enabled the knots to easily slide out after the completion of the trial.

Removal of the knots was necessary for testing knot quality, measured as the amount of knot slippage (in mm) that occurred when pulling on both ends of the knot following removal from the solid cylinder. The number of suture breakages was counted with each trial having at maximum two possible breakages, one on each arm. The applied shear force was also recorded throughout

the trial. Data for each of the two trials in the same condition (i.e. HFS vs. No Feedback) were averaged and statistical analysis was performed.

In order to assess the efficacy of our haptic feedback system for suture tying in robotic surgery, we will measure the performance of 17 subjects with the HFS enabled and not enabled, including a total of 170 trials, 85 of which will utilize vibrotactile feedback and 85 of which will receive no feedback. A total of seven statistical analyses will be performed on the data:

(1) Population analysis of faults (suture breakage) occurred during the trials.
(2) Population analysis of suture quality (quantified by the slippage amount).
(3) Population analysis of average force data during each trial.
(4) Population analysis of average force value used for HFS and NF.
(5) Population analysis of time for completing one trial.
(6) Analysis of the learning process.
(7) Analysis of breakage rate for the HFS enabled trials and no feedback enabled trails between the first 4 trials and the later 6 trials.

For each of the *7* analysis, we analyze the difference using a paired (or unpaired depends on the situation) sample t- test when the population is normally distributed or using a Wilcoxon singed-rank test when the population cannot be assumed to be normally distributed.

Shown in Fig. 70, a total of *7* instances of suture breakage occurred during the HFS trials, while without HFS, there were *17* instances of failure. In this case, the bi-axial sensing feedback system helps to reduce the suture failure by *59%* ($p = 0.0371$). All suture failures occurred at the point

of contact with the grasper. This result is consistent with observations made in previous experiments conducted with the da Vinci microneedle driver.

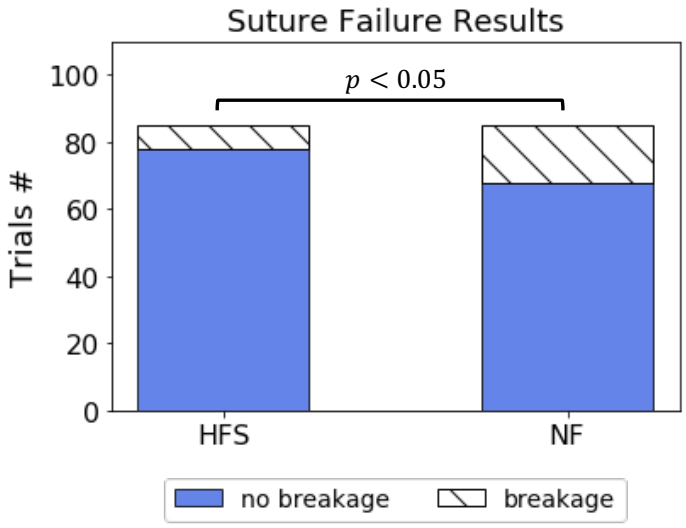

Figure 70 The number of suture breakage and no breakage for trials with HFS enabled and no feedback involved

Knot quality was measured by taking the slippage value of the tied knot, as shown in Figure 71. Results show 3.8% smaller slippage value with HFS enabled in comparison to no feedback. Though p=0.37940 suggests the result of improved slippage with the haptic feedback system is not statistically significant, we see no evidence that the knot quality is degraded by the HFS. The standard deviation for HFS, however, was 55% smaller than without feedback (the test statistic F=0.199061, is not in the 95% critical value accepted range [0.3621:2.7614], meaning the difference between the sample standard deviation of HFS and NF populations is big enough to be statistically significant). This finding suggests higher consistency of quality knots tied with HFS enabled than without.

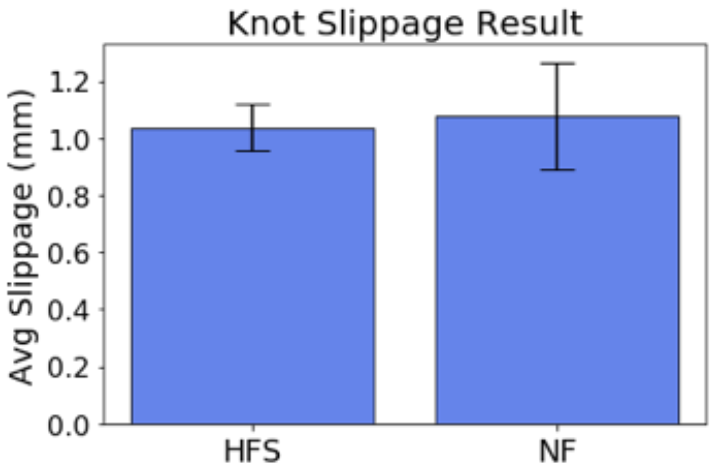

Figure 71 The average slippage value for 85 trials with HFS enabled and 85 trials with no feedback involved measured after each subject complete their full 10 trials

A 25.4% lower average force was observed for trials without feedback (p=0.00034) when comparing the average force for trials with and without suture breakage (Figure 72 left).

We also found that the average force used during trials where suture failure occurred is 11.6 N, while the average force for trials without a suture breakage is 9.6 N (p= 0.03925) (Fig. 72 right), suggesting a relationship between average force and suture breakage events. This relationship is inline with our observations of reduced average force and reduced suture breakage when using the HFS.

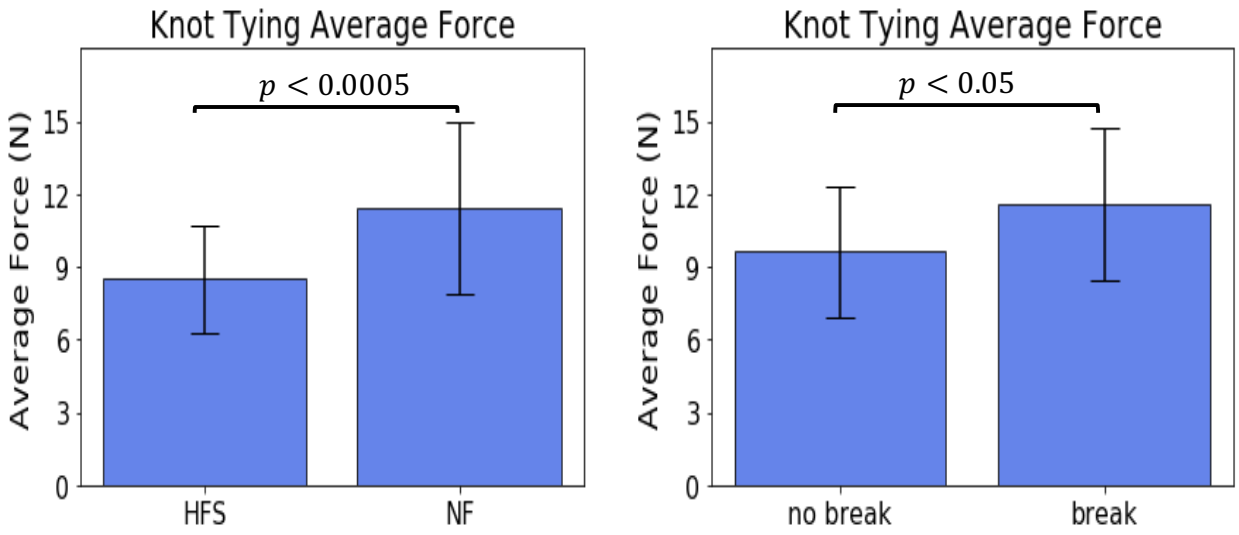

Figure 72 (left) The average combined bi-axial shear force used during each knot tying trial with HFS enabled and no feedback involved. (right) The average combined bi-axial shear force used during suture breakage trials and trials without suture breakage.

The time required for completing a one knot-tying trail with HFS enabled and without feedback is depicted in Figure 9. With HFS enabled, subjects took 13% longer than without feedback, but with a p=0.328948, there is no evidence that this difference is significant.

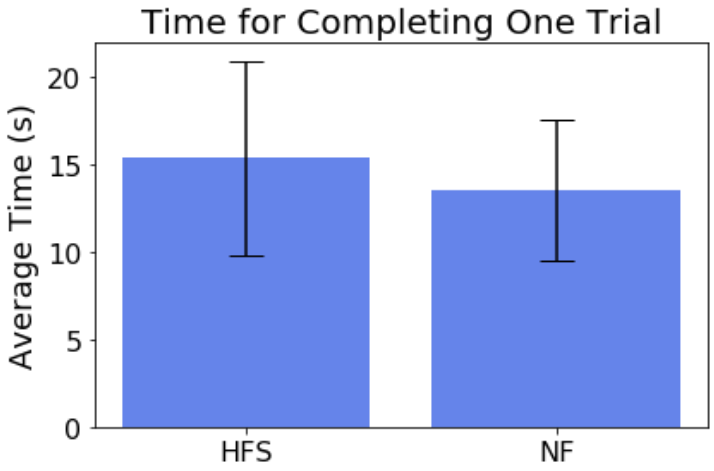

Figure 73 The average time for completing a knot tying task for each subject with HFS enabled and no feedback involved

Statistical analysis was performed to determine if subjects gained experience during the training (i.e., through the 10 trials they have performed). The knot quality of each subject's 1st and 2nd

trial was compared to the knot quality of the 9th and 10th trial. The results indicate that generally users tied more quality knots during the later trials compared to the initial trials (p=0.000129). A follow-on study could be performed to examine the role HFS played in improving knot quality over several trials by including a study where no haptic feedback is used.

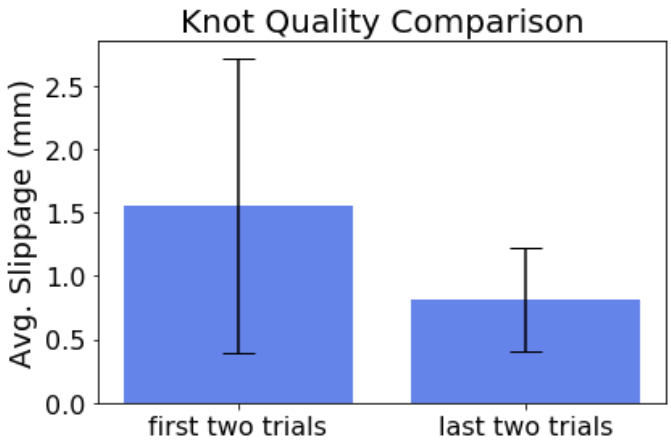

Figure 74 Comparison for the knot quality between the first two knots completed by the subjects vs the last two knots completed by the subjects. the average value and the standard deviation.

Our prior studies used 4 trials per subjects, while in this study each subject performed 10 trials. In order to investigate the potential for improvement through training as compared to our prior studies, we consider the first 4 trials for each subject as an initial training, or break-in, period. As such, we have compared the suture failure rate between the first 4 trials and the remaining 6 trials for the HFS group and NF group. For the HFS group, we have a significantly reduced breakage rate during the practice (p=0.02355) while for the NF group, there is no significant difference (p=0.45575). This result suggests that users required an adjustment period to acclimate to the feedback system, and significantly reduced the suture breakage rate, while subjects did not show improvement for trials without feedback. This result motivates further study in how users adapt to the feedback over multiple trials.

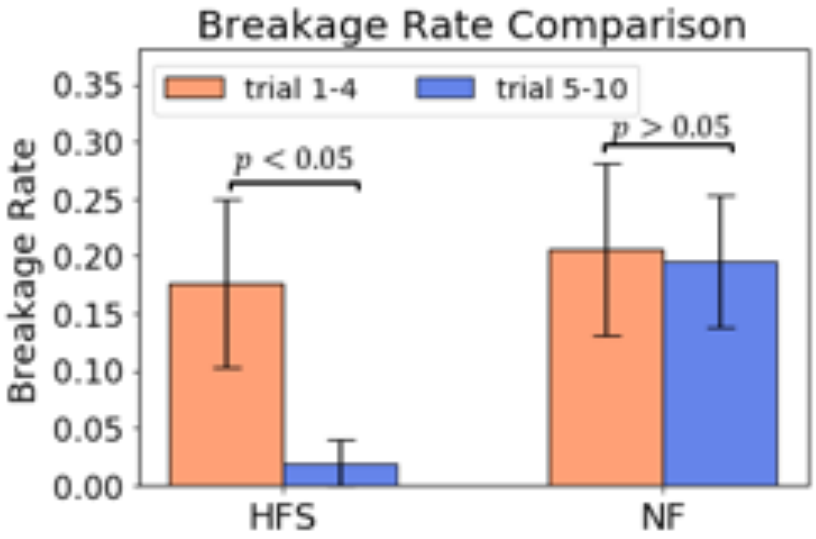

Figure 75 The breakage rate comparison of the HFS enabled trails and no feedback enabled trails between the first 4 trials and the later 6 trials.

The results of the suture breakage experiments provide valuable insight into the benefits of haptic feedback for robotic surgery involving suturing. Knot tying is one of the more challenging tasks in robotic surgery not only because of the complexity of forming a knot but also because the surgeon needs to determine how hard to pull a suture before the knot is sufficiently secure without weakening the suture material.

Forming a quality knot can mean the difference between a quick recovery for the patient or post-operative suture failure and serious complications. Several studies have demonstrated the mechanical superiority of knots tied with hands in comparison with knots tied with either the da Vinci robot or laparoscopically [165, 166].

7.3. Ex-Vivo Test

Subjects were asked to grab and hold four porcine bowel with different weight. A porcine model was used because it is a well-established model for abdominal surgery. For each investigation, two subjects were recruited, both have little to no experience with robotic surgery. The study was approved by the Animal Research Committee (ARC) under protocol number 2008-172-12A. Work with human subjects was approved by the Institutional Review Board (IRB) under protocol #11-000077. Each subject performed the task ten times, required to grip the bowel at maximum force they could apply with the da Vinci controller to prevent slippage and more importantly, to have a relative consistent normal force applied during the trial, and they should grab the bowel and hang in a direction as shown in the Figure 75 in order to get a relative consistent shear force applied during the trial. The applied grip and shear force were recorded throughout the study.

The number of faults parameter was recorded but not analyzed. This experimental design choice was made because of the difficulty that many novice subjects experienced picking up and handling the bowel tissue. This lack of inexperience and non-homogeneity of the tissue made this parameter too variable in novices to be valuable without requiring a very large number of subjects to be enrolled.

Figure 76 Ex-vivo porcine large intestine handled using da Vinci IS1200 Cadiere forceps

The initial testing result shows that the normal force recording is not valid. Shown in Fig. 77, though the grabbing of the bowel make relatively consistent capacitance change with respect to the starting capacitance, each releasing of the bowel has a decreased capacitance reading. We can assume that they have basically the same gripping force due to the mechanism of the da Vinci controller when at the maximum gripping force.

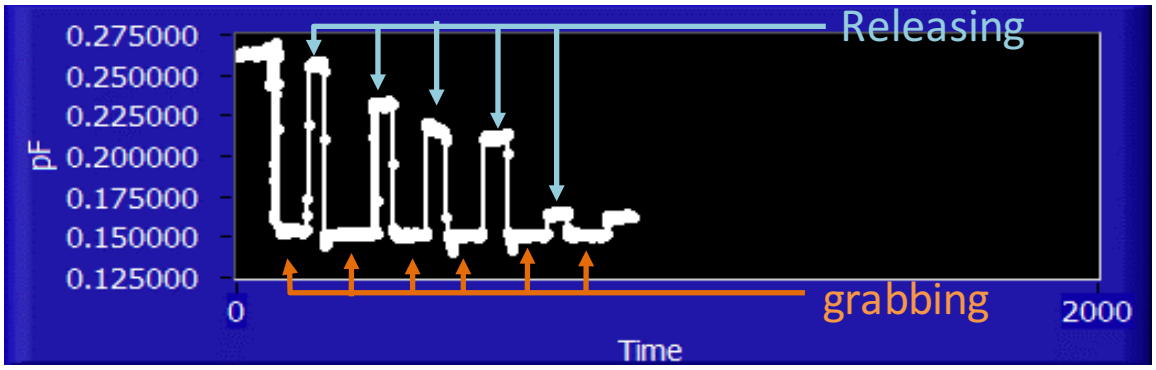

Figure 77 The normal force capacitance reading (in pF) for the first subject grabbing and releasing the first bowel

However, as for the shear, it is experiencing the similar situation, as shown in Fig. 78, the Y direction capacitance when releasing is growing as more test undergoes. And eventually, all the three directions capacitance went to overloaded capacitance reading when in touch with the bowel.

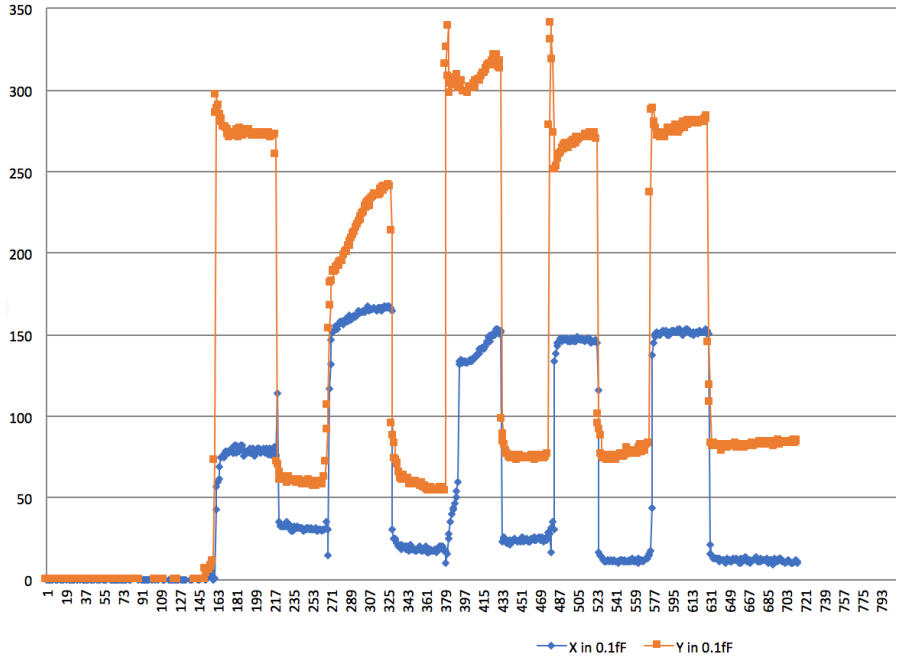

Figure 78 The shear force (x-direction and y-direction) change of capacitance readings (in 0.1fF) for the first subject grabbing and releasing the second bowel for the third time

After one day and we checked both normal and shear capacitance readings, they act correctly. We assume this task again proved that our sensor is water-proofing but not water-resistant. Ways to make the sensor system water-proofing is necessary and urgent.

Chapter 8: Summary

In this work, we have summarized the major tactile sensor technologies used for the medical surgery, piezoresistive sensors, piezoelectric sensors, optical sensors, magnetic sensors and the one we used for our project, capacitive sensors. Each sensor modality has its own advantages and disadvantages. The reason we choose capacitive sensors is we can overcome its shortcoming of complicated circuitry and noise sensitivity by using an existing capacitive to digital conversion chip, AD7746. One most recent single-sided capacitive sensor model is presented and all analytical and measured results are given. Flexible printed circuit board design was originally proposed but was replaced by a four-layer PCB design mainly for easier integration with the surgical tools. So far, we are able to evaluate our sensor system with a LabVIEW programmed user interface and control the haptic sensing system with an Arduino based microcontroller with a custom Visual Studio based program.

To our knowledge, this is the first demonstration of a novel multi-axis force sensor that was designed, fabricated and coupled with a custom sensing circuit for direct integration with a robotic surgical instrument. The sensors are made to quantify real-time forces applied at the tip of the surgical grasper. A sensor geometry is proposed that uses a single element and multiple electrodes to simultaneously sense shear and normal forces using precision capacitive transduction. All three directions demonstrated a resolution better than *0.3 N* and a linear dynamic range of *0- 20 N*. Results from the thermal experiment suggest the differential design is capable of compensating large temperature variance, making the system especially suitable for clinical use.

The results of the suture breakage experiments provide valuable insight regarding the benefits of haptic feedback for robotic surgery assisted suturing. Results show the bi-axial shear sensing system (with feedback enabled) reduced the incidence of suture failure by 59% ($p = 0.0371$), increased knot tightness by 3.8% ($p = 0.37940$), and resulted in 25% lower average applied force in comparison to trials without feedback ($p = 0.00034$). The time for trial completion with HFS enabled was 13% longer than that without feedback ($p = 0.328948$). Results of a 55% decrease in standard deviation of quality knots tied with HFS also indicate an improvement in consistency when using the feedback system.

The results suggest this system may improve outcomes related to knot tying tasks in robotic surgery and reduce instances of suture failure while maintaining the quality of knots produced.

The platform is ultimately intended for use in clinical applications of robotic surgery. The complete system has been integrated on a surgical instrument with the goal of connection to an experimental configuration. The ultimate demonstration of this system's utility will be if multi-axis tactile feedback can improve the outcomes of clinical procedures and enhance adoption of robotic systems for minimally invasive surgery in multiple procedures.

Chapter 9: Future Work

The results from this research suggest several possible directions both in continuing to advance the tactile feedback technology, and further evaluations of its benefit.

9.1. Robotic Surgery Training Study

The peg transfer task (Section 7.1) was performed without any valuable data analysis but for a verification of our system working together with the da Vinci system. Later, we can design a set of study with different actuating methods with normal force feedback and/ or shear force feedback, to check which combination of methods best improves the performance of users. It is hypothesized that the shear force value has a relationship with the subjects' proficiency.

The live tissue study (Section 7.3) was not complete because of the waterproofing issue. We are hoping to solve the waterproofing problem and then doing user study with the tactile feedback system activated and deactivated. We are hoping to use this study as a prove to show our capability to do ex-vivo tasks with improved performance (e.g., less normal and/ or shear force applied with feedback activated, fewer damages observed etc.).

9.2. Tactile Feedback System Improvement

For our sensing system, there are always some improvement can be done. For example,

1. miniaturization of the sensor board and circuit board from circuit design point of view.
2. separating the sensor board and circuit board to further miniaturizing the size and make sterilization easier.
3. making the system completely wirelessly by integrating with Bluetooth low energy (BLE).
4. making micro-scale force sensing array and compare its performance.

5. further improve the sensing parameters, such as sensitivity, resolution, and linear force range.

For the rest of the tactile feedback system, we can further improve the actuators, electronics, software and pneumatics.

9.3. Integration with other Feedback Methods

So far, we have experimented with the depressed-membrane pneumatic actuators and vibrotactile actuators, in the future, we can try other actuating methods, for example, mechanical actuator. We can also collaborate with the UCLA Graphics and Vision Lab who have been developing a machine vision system for automatically assessing a person's performance during Fundamentals of Laparoscopic Surgery (FLS) tasks [167].

9.4. Sterilization of the System

Sterilization is accomplished mainly by steam under pressure, by dry heat, by chemical sterilants by ethylene oxide (EtO), and many more, including gamma ray sterilization, electron beam sterilization etc [168]. The choice of the method for sterilization depends on a number of factors including the type of material that the object to be sterilized is made of, the number and type of microorganisms involved, the availability of sterilization methods etc.

The steam sterilization is achieved by exposing products to saturated steam at high temperatures (*121 C* to *132 C*). Steam sterilization process is not appropriate for many materials due to the high temperatures involved.

Dry heat sterilization utilizes hot air that is either free from water vapor, or has very little of it, and where this moisture plays a minimal or no role in the process of sterilization. Heat is absorbed by the exterior surface of an item and then passed inward to the next layer. Eventually, the entire item reaches the proper temperature needed to achieve sterilization.

Ethylene oxide (ETO) utilizes an alkaline agent gas that infiltrates packaged medical devices to kill microorganisms and thus achieve sterilization. ETO is toxic and flammable/ explosive at low temperatures and so is used on products that could get damaged or cannot withstand high temperature processes. This process can be typically applied on devices that incorporate electronic components, materials that get damaged at high temperatures, which suits our needs.

Also, the Standard Test Method for Determination of Effectiveness of Sterilization Processes for Reusable Medical Devices [169] set the standards for the sterilization processes, the comparison is listed in Table 28.

Table 28 Comparison between different sterilization processes

Sterilizer	Temperature	Pressure	Time
Steam autoclave lightly wrapped items heavily wrapped items	121 C (250 F) 132 C (270 F) 132 C (270 F)	15 psi 30 psi 30 psi	15 min 8 min 10 min
Dry heat, wrapped	170 C (340 F) 160 C (340 F) 150 C (285 F) 121 C (250 F)		60 min 120 min 150 min 180 min 12 hrs
Dry heat (rapid flow) unwrapped items packaged items	 190 C (375 F) 190 C (375 F)		 6 min 12 min
Chemical vapor	132 C (270 F)	20 -40 psi	20 min
Ethylene oxide	Ambient		8 -10 hrs

In conclusion, for our case, we would use ethylene oxide sterilization as our method.

9.5. Expand to other Applications

We can easily expand our tactile sensing system and/ or tactile feedback system to other minimally invasive surgical applications, specifically non-robotic laparoscopic surgery, remote surgery, and robotic surgery for clinical evaluation or for training purpose.

We can also apply our system to non-surgical applications, for example, general robotics, virtual reality etc.

Appendix

A. Python code for calculating the sensitivity vs design angle

```
import math

eps = 8.8542e-12*2.75; #dielectric constant

S0=1e-3; # width of the four trapezoid

x0= 0.24e-3; # initial value of overlap

h=0.25e-3; # designed width of trapezoid

d= 25e-6; # height of PDMS

E = 1e6; #1 MPa elastic modulus

p_ratio = 0.49; #poisson ratio

G = E/(2*(1 + p_ratio)); #shear modulus

A0=(S0-2*h)*x0+x0*x0;

A2=A0;

A3=A0;

A4=A0;

A5=A0;

Atrap=(S0-h)*h;

import pylab as p

import numpy as np


angle = p.linspace(0, 90, 1000000)

y=2*eps/d*S0- 4*eps/d*(h-x0)* (p.cos(angle*2*p.pi/360))/(p.sin(angle*2*p.pi/360));
```

```
tol = 2.4e-9

y[y > tol] = np.nan

y[y < -tol] = np.nan


p.plot(angle, y, 'g-', lw=1)

p.title('Sensitivity vs Design Angle', fontsize=20)

p.xlabel('Angle (in degree)', fontsize=16)

p.xticks(fontsize=16);

p.yticks(fontsize=16);


p.show()
```

B. Thinky Mixer Usage Procedure

The Thinky Mixer is capable of mixing up to 50ml/100g material at a time. The operation principle is it mixes the materials while remove air bubbles occurs or existing in the materials at the same time. The procedure is as follows:

1. Set the disposal transparent container with stirring material in the standard gray container.
2. Weigh the total, the disposal container together with the standard container and the material.
3. Open the door sliding it to front, set the standard container with material in the cup holder of the machine
4. Adjust the spinning balance (adjust the pointer of the balance indicator to the position of measured weight)
5. Close the door and power on.
6. Setting the mode: in our PDMS mixing case, we use mixing only mode, press the mode setting button until the mixing mode LED is lit on. Press timer up/ down button and set mixing time.
7. Start running.

C. Considerations with PDMS Usage

1. PDMS raw materials

   We are using Dow corning sylgard 182/184 Silicone Elastomer Kit which include base polymer and curing agent. Sylgard 182 cures slower at room temperature and thus allows longer working time. It is also better for thinner films.

2. Tools for PDMS processing
   a. Thinky mixer
   b. Syringe can be used alternatively to dispense instead of pouring
   c. Environmental plasma etcher for surface activation of PDMS prior to bonding
   d. Vacuum degassing chamber
   e. Curing oven
3. Controlling PDMS elasticity
   a. Tensile strength vs. curing temperature
      i. Higher curing temperature result in a stiffer (less elastic) film
   b. Tensile strength vs. mixing ratio
      i. More curing agent results in a stiffer film
   c. Tensile strength vs. film thickness
      i. Thinner PDMS is less elastic
4. Spincoating PDMS for controlled thickness
   a. Thickness vs. spin speed
   b. Thickness vs spin time

D. Scaling Calculation

In the semiconductor area, Dennard *et al.* [170] proposed a scaling methodology which maintains the electric field in the device constants, known as MOSFET scaling or Dennard scaling. I am using the same scaling methodology to calculate the performance when thinking about scaling our device dimensions ($S,\ l,\ d$) to a factor of $1/\kappa$.

The chip area (A) would be scaled to $1/\kappa^2$.

With the electric field in device (E) kept constant (1), we would have the power supply (V_{dd}) scaled to $1/\kappa$.

The current I would be scaled to $1/\kappa$ because of the scaled voltage.

The power dissipation P would scaled to $1/\kappa^2$.

And the power density $\sim P/A$ would be constant as a result.

The circuit delay time τ (CV/I) would be scaled to $1/\kappa$.

When talking about the capacitance, taking one of our base capacitances $C_0 = \frac{\epsilon_0 \epsilon_r S^2}{2d}$ as an example, we would have it scaled to $1/\kappa$.

When talking about normal force sensitivity, where $\frac{dC_z}{dF_{normal}} = \frac{C_0/AE}{(1-F_{normal}/AE)^2}$ (E in this equation is the young's modulus of the elastic material, not the electric field). Using the same approximation method as in Chapter 3.3.2.1, we would have a scaled factor $\frac{dC_z}{dF_{normal}} \sim \kappa$

When talking about shear force sensitivity, where $\frac{dC_x}{dF_{shear}} = \frac{dC_y}{dF_{shear}} \cong \frac{\epsilon_0 \epsilon_r (1+\upsilon) l}{AE}$ (E in this equation is the young's modulus of the elastic material, not the electric field). We would easily calculate with the l and A be scaled, we have $\frac{dC_{x,y}}{dF_{shear}} \sim \kappa$.

In conclusion, both normal force sensitivity and shear force sensitivity have improved with a factor of κ.

When thinking about thermal noise (which we count as the main cause of the noise source in our case), V_t=$\sqrt{4kTBR}$ ~$\sqrt{R}$~$\sqrt{\rho\frac{l}{A}}$~$\sqrt{\kappa}$

Resolution ($\frac{noise}{sensitivity}$) would also be improved at a factor of $\sqrt{1/\kappa}$.

However, we should note that, the sensitivity calculation has an estimation with the condition of $F_{normal} \ll AE$, meaning our linear dynamic range has this $F_{normal} \ll AE$ limitation. Thus, with A being scaled to $1/\kappa^2$, we would have our linear dynamic range also scaled to $1/\kappa^2$.

References

[1] U. Seibold, B. Kubler, and G. Hirzinger, "Prototype of Instrument for Minimally Invasive Surgery with 6-Axis Force Sensing Capability," pp. 496-501, 2005.

[2] A. Faragasso, J. Bimbo, Y. Noh, A. Jiang, S. Sareh, H. Liu*, et al.*, "Novel uniaxial force sensor based on visual information for minimally invasive surgery," pp. 1405-1410, 2014.

[3] P. Puangmali, K. Althoefer, L. D. Seneviratne, D. Murphy, and P. Dasgupta, "State-of-the-Art in Force and Tactile Sensing for Minimally Invasive Surgery," *IEEE Sensors Journal,* vol. 8, pp. 371-381, 2008.

[4] G. P. Haber, S. Crouzet, and I. S. Gill, "Laparoscopic and robotic assisted radical cystectomy for bladder cancer: a critical analysis," *Eur Urol,* vol. 54, pp. 54-62, Jul 2008.

[5] W. Y. Lau, K. C. Leow, and A. K. C. Li, "History of endoscopic and laparoscopic surgery," *World Journal Of Surgery,* vol. 21, pp. 444-453, May 1997.

[6] G. F. Buess, M. O. Schurr, and S. C. Fischer, "Robotics and allied technologies in endoscopic surgery," *Archives Of Surgery,* vol. 135, pp. 229-235, Feb 2000.

[7] G. P. Haber, S. Crouzet, and I. S. Gill, "Laparoscopic and robotic assisted radical cystectomy for bladder cancer: A critical analysis," *European Urology,* vol. 54, pp. 54-64, Jul 2008.

[8] E. Vaisbuch, C. Goldchmit, D. Ofer, A. Agmon, and Z. Hagay, "Laparoscopic hysterectomy versus total abdominal hysterectomy: A comparative study," *European Journal Of Obstetrics Gynecology And Reproductive Biology,* vol. 126, pp. 234-238, Jun 2006.

[9] C. KA, H. MJ, and G. A, "Ambulatory Surgery in the United States, 2006," National Health Statistics Reports, CDC2009.

[10] G. JC, K. KC, W. Y, R. V, L. G, and C. GM, "Perioperative safety and volume: outcomes relationships in bariatric surgery: a study of 32,000 patients," *J. Am. Coll. Surg. ,* vol. 213, pp. 771-7, 2011.

[11] M. R, B. EM, B. A, A. P, S. C, H. GB*, et al.*, "Nationwide use of laparoscopic hysterectomy compared with abdominal and vaginal approaches," *Arch Surg,* pp. 219-227, 2012.

[12] G. R, F. C, S. A, P. A, C. L, and S. M, "Laparoscopic splenectomy: conventional versus robotic approach--a comparative study," *J Laparoendosc Adv Surg Tech A,* pp. 393-8, 2011.

[13] S. JM and W. Y, "Robotically assisted laparascopic surgery," *Surg Endosc,* vol. 8, pp. 63-66, 1994.

[14] J. Shah, D. Buckley, J. Frisby, and A. Darzi, "Depth cue reliance in surgeons and medical students," *Surg. Endosc,* vol. 17, p. 1472, 2003.

[15] C. JA, S. AJ, W. WR, and M. CJ, "High Pressures Are Generated at the Tip of Laparoscopic Graspers," *J. Surgery,* vol. 69, pp. 127-130, 1999.

[16] E. A. M. Heijnsdijk, M. v. d. Voort, H. d. Visser, J. Dankelman, and D. J. Gouma, "Inter- and Intraindividual Variabilities of Perforation Forces of Human and Pig Bowel Tissue," *Surgical Endoscopy,* vol. 17, pp. 1923-1926, 2003.

[17] R. Anup and K. A. Balasubramanian, "Surgical Stress and the Gastrointestinal Tract," *J. Surgical Research,* vol. 92, pp. 291-300, 2000.

[18] D. D. Marucci, A. J. Shakeshaft, J. A. Cartmill, M. R. Cox, S. G. Adams, and C. J. Martin, "Grasper Trauma during Laparoscopic Cholecystectomy," *J. Surgery,* vol. 70, pp. 578-581, 2000.
[19] M. Schurr, G. F. Buess, B. Neisius, and U. Voges, "Robotics and telemanipulation technologies for endoscopic surgery: a review of the ARTEMIS project," *Surg. Endosc,* vol. 14, pp. 375-381, 2000.
[20] D. F. Louw, T. Fielding, P. B. McBeth, D. Gregoris, P. Newhook, and G. R. Sutherland, "Surgical robotics: a review and neurosurgical prototype development," *Neurosurgery,* vol. 54, pp. 525-37, 2004.
[21] A. R. Lanfranco, A. E. Castellanos, J. P. Desai, and W. C. Meyers, "Robotic surgery: a current perspective," *Ann Surg,* vol. 239, pp. 14-21, Jan 2004.
[22] (2016) Rise of the Surgical Robot and What Doctors Want. *Fortune*.
[23] . *The da Vinci® Surgical System*. Available: http://www.davincisurgery.com/da-vinci-surgery/da-vinci-surgical-system/
[24] G. I. Barbash, B. Friedman, S. A. Glied, and C. A. Steiner, "Factors associated with adoption of robotic surgical technology in US hospitals and relationship to radical prostatectomy procedure volume," *Ann Surg,* vol. 259, pp. 1-6, Jan 2014.
[25] R. H. van der Schatte Olivier, C. D. Van't Hullenaar, J. P. Ruurda, and I. A. Broeders, "Ergonomics, user comfort, and performance in standard and robot-assisted laparoscopic surgery," *Surg Endosc,* vol. 23, pp. 1365-71, Jun 2009.
[26] K. Moorthy, Y. Munz, A. Dosis, J. Hernandez, S. Martin, F. Bello*, et al.*, "Dexterity enhancement with robotic surgery," *Surg Endosc,* vol. 18, pp. 790-5, May 2004.
[27] S. A. Rivard. *da Vinci Hysterectomy*. Available: http://www.roboticsurgery4women.com/davinci_robotic_procedures_hysterectomy.html
[28] A. Fagotti, M. L. Gagliardi, F. Fanfani, M. G. Salerno, A. Ercoli, M. D'Asta*, et al.*, "Perioperative outcomes of total laparoendoscopic single-site hysterectomy versus total robotic hysterectomy in endometrial cancer patients: a multicentre study," *Gynecol Oncol,* vol. 125, pp. 552-5, Jun 2012.
[29] R. M. Suri, R. M. Antiel, H. M. Burkhart, M. Huebner, Z. Li, D. T. Eton*, et al.*, "Quality of Life After Early Mitral Valve Repair Using Conventional and Robotic Approaches," *Annals Of Thoracic Surgery,* vol. 93, pp. 761-769, Mar 2012.
[30] J. D. Schmitto, S. A. Mokashi, and L. H. Cohn, "Past, present, and future of minimally invasive mitral valve surgery," *J Heart Valve Dis,* vol. 20, pp. 493-8, Sep 2011.
[31] E. J. Hanly and M. A. Talamini, "Robotic abdominal surgery," *Am J Surg,* vol. 188, pp. 19S-26S, Oct 2004.
[32] S. Breitenstein, A. Nocito, M. Puhan, U. Held, M. Weber, and P. A. Clavien, "Robotic-assisted versus laparoscopic cholecystectomy: outcome and cost analyses of a case-matched control study," *Ann Surg,* vol. 247, pp. 987-93, Jun 2008.
[33] G. Jacobsen, R. Berger, and S. Horgan, "The role of robotic surgery in morbid obesity," *J Laparoendosc Adv Surg Tech A,* vol. 13, pp. 279-83, Aug 2003.
[34] M. R. Ali, B. Bhaskerrao, and B. M. Wolfe, "Robot-assisted laparoscopic Roux-en-Y gastric bypass," *Surg Endosc,* vol. 19, pp. 468-72, Apr 2005.
[35] C. J. Mohr, G. S. Nadzam, and M. J. Curet, "Totally robotic Roux-en-Y gastric bypass," *Arch Surg,* vol. 140, pp. 779-86, Aug 2005.

[36] C. J. Mohr, G. S. Nadzam, R. S. Alami, B. R. Sanchez, and M. J. Curet, "Totally robotic laparoscopic Roux-en-Y Gastric bypass: results from 75 patients," *Obes Surg,* vol. 16, pp. 690-6, Jun 2006.

[37] G. Hubens, L. Balliu, M. Ruppert, B. Gypen, T. Van Tu, and W. Vaneerdeweg, "Roux-en-Y gastric bypass procedure performed with the da Vinci robot system: is it worth it?," *Surgical Endoscopy And Other Interventional Techniques,* vol. 22, pp. 1690-1696, Jul 2008.

[38] B. E. Snyder, T. Wilson, B. Y. Leong, C. Klein, and E. B. Wilson, "Robotic-assisted Roux-en-Y Gastric bypass: minimizing morbidity and mortality," *Obes Surg,* vol. 20, pp. 265-70, Mar 2010.

[39] N. C. Buchs, F. Pugin, G. Chassot, F. Volonte, P. Koutny-Fong, M. E. Hagen*, et al.*, "Robot-assisted Roux-en-Y gastric bypass for super obese patients: a comparative study," *Obes Surg,* vol. 23, pp. 353-7, Mar 2013.

[40] M. Talamini, K. Campbell, and C. Stanfield, "Robotic gastrointestinal surgery: early experience and system description," *J Laparoendosc Adv Surg Tech A,* vol. 12, pp. 225-32, Aug 2002.

[41] M. A. Talamini, S. Chapman, S. Horgan, W. S. Melvin, and G. Academic Robotics, "A prospective analysis of 211 robotic-assisted surgical procedures," *Surg Endosc,* vol. 17, pp. 1521-4, Oct 2003.

[42] C. P. Delaney, A. C. Lynch, A. J. Senagore, and V. W. Fazio, "Comparison of robotically performed and traditional laparoscopic colorectal surgery," *Dis Colon Rectum,* vol. 46, pp. 1633-9, Dec 2003.

[43] A. M. Lacy, J. C. Garcia-Valdecasas, S. Delgado, A. Castells, P. Taura, J. M. Pique*, et al.*, "Laparoscopy-assisted colectomy versus open colectomy for treatment of non-metastatic colon cancer: a randomised trial," *Lancet,* vol. 359, pp. 2224-9, Jun 29 2002.

[44] G. Scozzari, F. Rebecchi, P. Millo, S. Rocchietto, R. Allieta, and M. Morino, "Robot-assisted gastrojejunal anastomosis does not improve the results of the laparoscopic Roux-en-Y gastric bypass," *Surg Endosc,* vol. 25, pp. 597-603, Feb 2011.

[45] M. Nasir, S. Panteleimonitis, J. Ahmed, H. Abbas, and A. Parvaiz, "Learning Curves in Robotic Rectal Cancer Surgery: A literature Review," *Journal of Minimally Invasive Surgical Sciences,* vol. 5, 2016.

[46] C. R. Wagner, N. Stylopoulos, and R. D. Howe, "The role of force feedback in surgery: analysis of blunt dissection," pp. 68-74, 2002.

[47] A. Abiri, A. Tao, M. LaRocca, X. Guan, S. J. Askari, J. W. Bisley*, et al.*, "Visual-perceptual mismatch in robotic surgery," *Surg Endosc,* Dec 06 2016.

[48] N. Enayati, E. De Momi, and G. Ferrigno, "Haptics in Robot-Assisted Surgery: Challenges and Benefits," *IEEE Rev Biomed Eng,* vol. 9, pp. 49-65, 2016.

[49] M. Morino, L. Pellegrino, C. Giaccone, C. Garrone, and F. Rebecchi, "Randomized clinical trial of robot-assisted versus laparoscopic Nissen fundoplication," *Br J Surg,* vol. 93, pp. 553-8, May 2006.

[50] C. N. Gutt, T. Oniu, A. Mehrabi, A. Kashfi, P. Schemmer, and M. W. Buchler, "Robot-assisted abdominal surgery," *Br J Surg,* vol. 91, pp. 1390-7, Nov 2004.

[51] I. E. Nakadi, C. Melot, J. Closset, V. DeMoor, K. Betroune, P. Feron*, et al.*, "Evaluation of da Vinci Nissen fundoplication clinical results and cost minimization," *World J Surg,* vol. 30, pp. 1050-4, Jun 2006.

[52] G. A. Antoniou, C. V. Riga, E. K. Mayer, N. J. Cheshire, and C. D. Bicknell, "Clinical applications of robotic technology in vascular and endovascular surgery," *J Vasc Surg,* vol. 53, pp. 493-9, Feb 2011.
[53] D. J. Beebe, A. S. Hsieh, D. D. Denton, and R. G. Radwin, "A silicon force sensor for robotics and medicine," *Sensors and Actuators A: Physical,* vol. 50, pp. 55-65, 1995.
[54] L. Beccai, S. Roccella, A. Arena, F. Valvo, P. Valdastri, A. Menciassi*, et al.*, "Design and fabrication of a hybrid silicon three-axial force sensor for biomechanical applications," *Sensors and Actuators A: Physical,* vol. 120, pp. 370-382, 2005.
[55] S. Omata and Y. Terunuma, "New tactile sensor like the human hand and its applications," *Sensors and Actuators A: Physical,* vol. 35, pp. 9-15, 1992.
[56] J. Dargahi, "A piezoelectric tactile sensor with three sensing elements for robotic, endoscopic and prosthetic applications," *Sensors And Actuators a-Physical,* vol. 80, pp. 23-30, Mar 1 2000.
[57] M. Leineweber, G. Pelz, M. Schmidt, H. Kappert, and G. Zimmer, "New tactile sensor chip with silicone rubber cover," *Sensors and Actuators A: Physical,* vol. 84, pp. 236-245, 2000.
[58] L. Hyung-Kew, C. Sun-Il, K. Kyung-Hyun, K. Seong-Jin, Y. Kwang-Seok, and Y. Euisik, "A modular expandable tactile sensor using flexible polymer," pp. 642-645, 2005.
[59] H. B. Muhammad, C. M. Oddo, L. Beccai, C. Recchiuto, C. J. Anthony, M. J. Adams*, et al.*, "Development of a bioinspired MEMS based capacitive tactile sensor for a robotic finger," *Sensors and Actuators A: Physical,* vol. 165, pp. 221-229, 2011.
[60] H. Su, M. Zervas, C. Furlong, and G. S. Fischer, "A Miniature MRI-Compatible Fiber-optic Force Sensor Utilizing Fabry-Perot Interferometer," pp. 131-136, 2011.
[61] J.-S. Heo, J.-H. Chung, and J.-J. Lee, "Tactile sensor arrays using fiber Bragg grating sensors," *Sensors and Actuators A: Physical,* vol. 126, pp. 312-327, 2006.
[62] J. Peirs, J. Clijnen, D. Reynaerts, H. V. Brussel, P. Herijgers, B. Corteville*, et al.*, "A micro optical force sensor for force feedback during minimally invasive robotic surgery," *Sensors and Actuators A: Physical,* vol. 115, pp. 447-455, 2004.
[63] G. F. Buess, "Robotics and Allied Technologies in Endoscopic Surgery," *Archives of Surgery,* vol. 135, p. 229, 2000.
[64] C. R. Wagner and R. D. Howe, "Force Feedback Benefit Depends on Experience in Multiple Degree of Freedom Robotic Surgery Task," *IEEE Transactions on Robotics,* vol. 23, pp. 1235-1240, 2007.
[65] J. Dargahi, R. Sedaghati, H. Singh, and S. Najarian, "Modeling and testing of an endoscopic piezoelectric-based tactile sensor," *Mechatronics,* vol. 17, pp. 462-467, 2007.
[66] J. Rosen, B. Hannaford, M. P. MacFarlane, and M. N. Sinanan, "Force controlled and teleoperated endoscopic grasper for minimally invasive surgery-experimental performance evaluation," *IEEE Transactions on Biomedical Engineering,* vol. 46, pp. 1212-1221, 1999.
[67] G. Tholey and J. P. Desai, "A Modular, Automated Laparoscopic Grasper with Three-Dimensional Force Measurement Capability," pp. 250-255, 2007.
[68] K. J. Rebello, "Applications of MEMS in Surgery," *Proceedings of the IEEE,* vol. 92, pp. 43-55, 2004.

[69] P. Valdastri, K. Harada, A. Menciassi, L. Beccai, C. Stefanini, M. Fujie*, et al.*, "Integration of a miniaturised triaxial force sensor in a minimally invasive surgical tool," *IEEE Trans Biomed Eng,* vol. 53, pp. 2397-400, Nov 2006.
[70] A. I. Aviles, S. M. Alsaleh, P. Sobrevilla, and A. Casals, "Force-feedback sensory substitution using supervised recurrent learning for robotic-assisted surgery," *Conf Proc IEEE Eng Med Biol Soc,* vol. 2015, pp. 1-4, 2015.
[71] A. O. El Saddik, M.; Eid, M.; Cha, J., *Haptics Technologies bringing touch to multimedia*, 2011.
[72] S. J. Biggs, Mandayam A. Srinivasan, "Haptic Interfaces," *Handbook of virtual Environments,* pp. 93-116, 2002.
[73] T. B. Sheridan, "Musings on Telepresence and Virtual Presence," *Presence,* vol. 1, pp. 120-126, 1992.
[74] K. J. Kuchenbecker, J. Fiene, and G. Niemeyer, "Improving contact realism through event-based haptic feedback," *Ieee Transactions on Visualization And Computer Graphics,* vol. 12, pp. 219-230, Mar-Apr 2006.
[75] M. A. Srinivasan and C. Basdogan, "Haptics in virtual environments: Taxonomy, research status, and challenges," *Computers & Graphics-Uk,* vol. 21, pp. 393-404, Jul-Aug 1997.
[76] M. L. McLaughlin, *Touch in Virtual Environments: Haptics and the Design of Interactive Systems*, 2002.
[77] S. A. Seah, M. Obrist, A. Roudaut, and S. Subramanian, "Need for Touch in Human Space Exploration: Towards the Design of a Morphing Haptic Glove - ExoSkin," *Human-Computer Interaction - Interact 2015, Pt Iv,* vol. 9299, pp. 18-36, 2015.
[78] I. F. Costa and R. Balaniuk, "LEM - An approach for real time physically based soft tissue simulation," *2001 Ieee International Conference on Robotics And Automation, Vols I-Iv, Proceedings,* pp. 2337-2343, 2001.
[79] N. Langrana, G. Burdea, J. Ladeji, and M. Dinsmore, "Human performance using virtual reality tumor palpation simulation," *Computers & Graphics,* vol. 21, pp. 451-458, Jul-Aug 1997.
[80] R. M. d. M. Liliane dos Santos Machado, Marcelo Knorich Zuffo, "Fuzzy Rule-Based Evaluation for a Haptic and Stereo Simulator for Bone Marrow Harvest for Transplant."
[81] C. H. King, M. O. Culjat, M. L. Franco, J. W. Bisley, E. Dutson, and W. S. Grundfest, "Optimization of a pneumatic balloon tactile display for robot-assisted surgery based on human perception," *IEEE Trans Biomed Eng,* vol. 55, pp. 2593-600, Nov 2008.
[82] C. H. King, M. O. Culjat, M. L. Franco, C. E. Lewis, E. P. Dutson, W. S. Grundfest*, et al.*, "Tactile Feedback Induces Reduced Grasping Force in Robot-Assisted Surgery," *IEEE Trans Haptics,* vol. 2, pp. 103-110, Apr-Jun 2009.
[83] E. Olivieri, G. Barresi, D. G. Caldwell, L. S. Mattos, E. Olivieri, G. Barresi*, et al.*, "Haptic Feedback for Control and Active Constraints in Contactless Laser Surgery: Concept, Implementation, and Evaluation," *IEEE Trans Haptics,* vol. 11, pp. 241-254, Apr-Jun 2018.
[84] B. T. Bethea, A. M. Okamura, M. Kitagawa, T. P. Fitton, S. M. Cattaneo, V. L. Gott*, et al.*, "Application of haptic feedback to robotic surgery," *J Laparoendosc Adv Surg Tech A,* vol. 14, pp. 191-5, Jun 2004.

[85] E. P. Westebring-van der Putten, R. H. Goossens, J. J. Jakimowicz, and J. Dankelman, "Haptics in minimally invasive surgery--a review," *Minim Invasive Ther Allied Technol,* vol. 17, pp. 3-16, 2008.
[86] P. Saccomandi, E. Schena, C. M. Oddo, L. Zollo, S. Silvestri, and E. Guglielmelli, "Microfabricated tactile sensors for biomedical applications: a review," *Biosensors (Basel),* vol. 4, pp. 422-48, Dec 2014.
[87] W. S. McMath, S. K. Yeung, E. M. Petriu, D. C. Petriu, and M. D. Colven, "High sampling resolution tactile sensor for object recognition," pp. 579-583, 1993.
[88] R. D. Ponce Wong, J. D. Posner, and V. J. Santos, "Flexible microfluidic normal force sensor skin for tactile feedback," *Sensors and Actuators A: Physical,* vol. 179, pp. 62-69, 2012.
[89] P. Yong-Lae, C. Bor-Rong, and R. J. Wood, "Design and Fabrication of Soft Artificial Skin Using Embedded Microchannels and Liquid Conductors," *IEEE Sensors Journal,* vol. 12, pp. 2711-2718, 2012.
[90] P. Dario, D. De Rossi, C. Domenici, and R. Francesconi, "Ferroelectric polymer tactile sensors with anthropomorphic features," vol. 1, pp. 332-340, 1984.
[91] Z. Chu, P. M. Sarro, and S. Middelhoek, "Silicon Three-axial Tactile Sensor," vol. 1, pp. 656-659, 1995.
[92] H.-K. Lee, S.-I. Chang, and E. Yoon, "A Flexible Polymer Tactile Sensor: Fabrication and Modular Expandability for Large Area Deployment," *Journal of Microelectromechanical Systems,* vol. 15, pp. 1681-1686, 2006.
[93] H. B. Muhammad, C. Recchiuto, C. M. Oddo, L. Beccai, C. J. Anthony, M. J. Adams*, et al.*, "A capacitive tactile sensor array for surface texture discrimination," *Microelectronic Engineering,* vol. 88, pp. 1811-1813, 2011.
[94] X. Liu, Iordachita, II, X. He, R. H. Taylor, and J. U. Kang, "Miniature fiber-optic force sensor based on low-coherence Fabry-Perot interferometry for vitreoretinal microsurgery," *Biomed Opt Express,* vol. 3, pp. 1062-76, May 01 2012.
[95] S. M. De Rossi, T. Lenzi, N. Vitiello, M. Donati, A. Persichetti, F. Giovacchini*, et al.*, "Development of an in-shoe pressure-sensitive device for gait analysis," *Conf Proc IEEE Eng Med Biol Soc,* vol. 2011, pp. 5637-40, 2011.
[96] S. Schostek, M. O. Schurr, and G. F. Buess, "Review on aspects of artificial tactile feedback in laparoscopic surgery," *Med Eng Phys,* vol. 31, pp. 887-98, Oct 2009.
[97] P. Puangmali, L. Hongbin, L. D. Seneviratne, P. Dasgupta, and K. Althoefer, "Miniature 3-Axis Distal Force Sensor for Minimally Invasive Surgical Palpation," *IEEE/ASME Transactions on Mechatronics,* vol. 17, pp. 646-656, 2012.
[98] A. E. Arnau Vives, *Piezoelectric Transducers and Applications*: Springer-Verlag, 2008.
[99] R. S. Dahiya and M. Valle, *Robotic tactile sensing technologies and systems*: New York: Dordrecht Heidelberg, 2013.
[100] Y. H, B. M, and A. K, "Tactile sensing for dexterous in-hand manipulation in robotics: a review," *Sensors Actuators A* pp. 171-87, 2011.
[101] S. Najarian, J. Dargahi, and Mehrizi, *Artificial tactile sensing in biomedical engineering*: New York: McGraw-Hill, 2009.
[102] R. S. Dahiya, G. Metta, M. Valle, and G. Sandini, "Tactile sensing—from humans to humanoids," *IEEE Trans. Robot,* vol. 26, pp. 1-20, 2010.

[103] H. Liu, P. Meusel, and G. Hirzinger, "A tactile sensing system for the DLR three-finger robot hand," *in Proc. Int. Symp. Meas. Control Robot,* pp. 91-96.1837, 1995.
[104] M. A. Diftler, J. R. Platt, C. J. Culbert, R. O. Ambrose, and W. J. Bluethmann, "Evolution of the nasa/darpa robonaut control system," *in Proc. IEEE Int. Conf. Robot. Autom.,* pp. 2543-2548, 2003.
[105] B. L. Gray and R. S. Fearing, "A surface micromachined microtactile sensor array," *in Proc. Int. Conf. Robot. Automat.,* vol. 1, pp. 1-6, 1996.
[106] R. J. D. Souza and K. D. Wise, "A very high density bulk micromachined capacitive tactile imager," *in Proc. Int. Conf. Solid-State Sens. Actuators, Transducers,* pp. 1473-1476, 1997.
[107] P. A. Schmidt, E. Mael, and R. P. Wurtz, "A sensor for dynamic tactile information with applications in human-robot interaction & object exploration," *Robot. Autonomous Syst.,* vol. 54, pp. 1005-1014, 2006.
[108] E. S. Kolesar, R. R. Reston, D. G. Ford, and R. C. Fitch, "Multiplexed piezoelectric polymer tactile sensor," *J. Robot. Syst. ,* vol. 9, pp. 37-63, 1992.
[109] J. Dargahi, M. Parameswaran, and S. Payandeh, "A micromachined piezoelectric tactile sensor for an endoscopic grasper—theory, fabrication and experiments," *J. Microelectromech. Syst.,* vol. 9, pp. 329-335, 2000.
[110] Y. Yamada, T. Maeno, I. Fujimoto, T. Morizono, and Y. Umetani, "Identification of incipient slip phenomena based on the circuit output signal of PVDF film strips embedded in artificial finger ridges," *in Proc. SIC Robots Syst.,* pp. 2638-2643, 2005.
[111] B. Choi, H. R. Choi, and S. Kang, "Development of tactile sensor for detecting contact force and slip," *in Proc. IEEE/RSJ Int. Conf. Intell. Robots Syst.,* pp. 2638-2643, 2005.
[112] J. E. Barg, X. Jin, M. Wiltshire, M. Abolhasani, and J. F. Holzman, "Photoconductive sensors for distributed optical sensing," *in Electrical and Computer Engineering (CCECE), 2010 23rd Canadian Conference on,* pp. 1-4,2-5, 2010.
[113] S. M. Abdullah, "Organic Semiconductors: Applications in Solar Photovoltaic and Sensor Devices," *Materials Science Forum,* vol. 737, 2013.
[114] M. O'Toole and D. Diamond, "Absorbance Based Light Emitting Diode Optical Sensors and Sensing Devices," " *Sensors,* pp. 2453-2479, 2008.
[115] T. F. Refaat, "AlGaAsSb/InGaAsSb phototransistors for 2-μm remote sensing applications," *Optical Engineering* pp. 1647-1650, 2004.
[116] Z. Tian, S. Y. Scott, and H. P. Loock, "Refractive index sensor based on an abrupt taper Michelson interferometer in a single-mode fiber," *Optics Letters,* pp. 1105-1107, 2008.
[117] K. A. Murphy, "Quadrature phase-shifted, extrinsic Fabry–Perot optical fiber sensors," *Optics Letters,* pp. 273-275, 1991.
[118] E. Zimmermann, A. Verweerd, W. Glaas, A. Tillmann, and A. Kemna, "An AMR sensor-based measurement system for magnetoelectrical resistivity tomography," *IEEE Sensors J.,* vol. 5, pp. 233-241, 2005.
[119] L. Xu, H. Yu, S.-J. Han, S. Osterfeld, R. L. White, N. Pourmand*, et al.*, "Giant magnetoresistive sensors for DNA microarray," *IEEE Trans. Magn.,* vol. 44, pp. 3989-3991, 2008.
[120] C. Albon, A. Weddemann, A. Auge, K. Rott, and A. Hütten, "Tunneling magnetoresistance sensors for high resolutive particle detection," *Applied Physics Letters,* 2009.

[121] E. Torres-Jara, I. Vasilescu, and R. Coral, "A soft touch: Compliant tactile sensors for sensitive manipulation," *CSAIL, Mass. Inst. Technol., Cambridge, MA, Tech. Rep,* 2006.
[122] L. Jamone, G. Metta, F. Nori, and G. Sandini, "James: A humanoid robot acting over an unstructured world," *in Proc. 6th IEEE-RAS Int. Conf. Humanoid Robots, Genoa, Italy,* pp. 143-150, 2006.
[123] T. J. Nelson, R. B. V. Dover, S. Jin, S. Hackwood, and G. Beni, "Shear sensitive magnetoresistive robotic tactile sensor," *IEEE Trans. Magn.,* vol. MAG-22, pp. 394-396, 1986.
[124] H. Yousef, M. Boukallel, and K. Althoefer, "Tactile sensing for dexterous in-hand manipulation in robotics—A review," *Sensors and Actuators A: Physical,* vol. 167, pp. 171-187, 2011.
[125] M. Jakopec, S. J. Harris, F. Rodriguez y Baena, P. Gomes, and B. L. Davies, "The Acrobot®system for total knee replacement," *Industrial Robot: An International Journal,* vol. 30, pp. 61-66, 2003.
[126] U. Kim, D.-H. Lee, W. J. Yoon, B. Hannaford, and H. R. Choi, "Force Sensor Integrated Surgical Forceps for Minimally Invasive Robotic Surgery," *IEEE Transactions on Robotics,* vol. 31, pp. 1214-1224, 2015.
[127] R. Haslinger, P. Leyendecker, and U. Seibold, "A fiberoptic force-torque-sensor for minimally invasive robotic surgery," pp. 4390-4395, 2013.
[128] Y. Yang, F. Wang, P. Zhang, C. Shi, Y. Zou, H. Qin*, et al.*, "Robot-assisted versus conventional laparoscopic surgery for colorectal disease, focusing on rectal cancer: a meta-analysis," *Ann Surg Oncol,* vol. 19, pp. 3727-36, Nov 2012.
[129] C. R. Wottawa, B. Genovese, B. N. Nowroozi, S. D. Hart, J. W. Bisley, W. S. Grundfest*, et al.*, "Evaluating tactile feedback in robotic surgery for potential clinical application using an animal model," *Surg Endosc,* vol. 30, pp. 3198-209, Aug 2016.
[130] M. Y. Cheng, C. L. Lin, Y. T. Lai, and Y. J. Yang, "A polymer-based capacitive sensing array for normal and shear force measurement," *Sensors (Basel),* vol. 10, pp. 10211-25, 2010.
[131] J. A. Dobrzynska and M. A. M. Gijs, "Polymer-based flexible capacitive sensor for three-axial force measurements," *J. Micromech. Microeng,* 2012.
[132] S. R, "A three-axis high-resolution capacitive tactile imager system based on floating comb electrodes," *J. Micromech. Microeng,* 2013.
[133] R. A. Brookhuis, H. Droogendijk, M. J. d. Boer, R. G. P. Sanders, T. S. J. Lammerink, R. J. Wiegerink*, et al.*, "Six-axis force-torque sensor with a large range for biomechanical applications," *J. Micromech. Microeng,* 2014.
[134] Y. Mi, Y. Chan, D. Trau, P. Huang, and E. Chen, "Micromolding of PDMS scaffolds and microwells for tissue culture and cell patterning: A new method of microfabrication by the self-assembled micropatterns of diblock copolymer micelles," *Polymer,* vol. 47, pp. 5124-5130, 2006.
[135] N. Q. Balaban, U. S. Schwarz, D. Riveline, P. Goichberg, G. Tzur, I. Sabanay*, et al.*, "Force and focal adhesion assembly: a close relationship studied using elastic micropatterned substrates," *Nat Cell Biol,* vol. 3, pp. 466-72, May 2001.
[136] "24-Bit Capacitance-to-Digital Converter with Temperature Sensor," in *datasheet*, ed.
[137] *Handbook of Adhesives*: Springer US, 1990.

[138] M. Ohka, Y. Mitsuya, I. Higashioka, and H. Kabeshita, "An Experimental Optical Three-axis Tactile Sensor for Micro-Robots," *Robotica,* vol. 23, pp. 457-465, 2005.
[139] SFUPTOWNMAKER. *I2C*. Available: https://learn.sparkfun.com/tutorials/i2c
[140] Jimbo. *Serial Communication*. Available: https://learn.sparkfun.com/tutorials/serial-communication
[141] B_E_N. *What is an Arduino?* . Available: https://learn.sparkfun.com/tutorials/what-is-an-arduino
[142] "TCA9548A Low-Voltage 8-Channel I2C Switch with Reset datasheet," ed. Texas Instruments: Texas Instruments.
[143] A. Zeller, *Why Programs Fail: A Guide to Systematic Debugging*. San Francisco, CA, USA: Morgan Kaufmann Publishers Inc., 2005.
[144] Y. Dai, A. Abiri, S. Liu, O. Paydar, H. Sohn, E. P. Dutson*, et al.*, "Grasper Integrated Tri-Axial Force Sensor System for Robotic Minimally Invasive Surgery," in *39th Annual International Conference of the IEEE EMBS*, Jeju Island, Korea, 2017.
[145] M. Perez, S. Xu, S. Chauhan, A. Tanaka, K. Simpson, H. Abdul-Muhsin*, et al.*, "Impact of delay on telesurgical performance: study on the robotic simulator dV-Trainer," *Int J Comput Assist Radiol Surg,* vol. 11, pp. 581-7, Apr 2016.
[146] M. Anvari, "Robot-assisted remote telepresence surgery," *Semin Laparosc Surg,* vol. 11, pp. 123-8, Jun 2004.
[147] C. R. Wottawa, "An Investigation into the Benefits of Tactile Feedback for Laparoscopic, Robotic, and Remote Surgery," University of California, Los Angeles, 2013.
[148] A. Abiri, O. Paydar, A. Tao, M. LaRocca, K. Liu, B. Genovese*, et al.*, "Tensile strength and failure load of sutures for robotic surgery," *Surg Endosc,* Dec 07 2016.
[149] A. Abiri, X. Guan, Y. Dai, A. Tao, Z. Xiao, E. P. Dutson*, et al.*, "Depressed-Membrane Pneumatic Actuators for Robotic Surgery," presented at the The 38th Annual International Conference of the IEEE Engineering in Medicine and Biology Society (EMBC'16), 2016.
[150] J. A. Cartmill, A. J. Shakeshaft, W. R. Walsh, and C. J. Martin, "High Pressures Are Generated at the Tip of Laparoscopic Graspers," *ANZ Journal of Surgery,* vol. 69, pp. 127-130, 1999.
[151] D. D. Marucci, A. J. Shakeshaft, J. A. Cartmill, M. R. Cox, S. G. Adams, and C. J. Martin, "Grasper trauma during laparoscopic cholecystectomy," *Aust N Z J Surg,* vol. 70, pp. 578-81, Aug 2000.
[152] V. Bhatia and R. K. Tandon, "Stress and the gastrointestinal tract," *Journal of Gastroenterology and Hepatology,* vol. 20, pp. 332-339, 2005.
[153] S. De, J. Rosen, A. Dagan, B. Hannaford, P. Swanson, and M. Sinanan, "Assessment of Tissue Damage due to Mechanical Stresses," *The International Journal of Robotics Research,* vol. 26, pp. 1159-1171, 2016.
[154] K. A. LeBlanc, "Laparoscopic incisional and ventral hernia repair: complications-how to avoid and handle," *Hernia,* vol. 8, pp. 323-31, Dec 2004.
[155] R. Anup and K. A. Balasubramanian, "Surgical stress and the gastrointestinal tract," *J Surg Res,* vol. 92, pp. 291-300, Aug 2000.

[156] J. Melinek, P. Lento, and J. Moalli, "Postmortem analysis of anastomotic suture line disruption following carotid endarterectomy," *J Forensic Sci,* vol. 49, pp. 1077-81, Sep 2004.
[157] Y. Hirano, N. Ishikawa, and G. Watanabe, "Suture damage after grasping with EndoWrist of the da Vinci Surgical System," *Minim Invasive Ther Allied Technol,* vol. 19, pp. 203-6, Aug 2010.
[158] J. Diks, D. Nio, M. A. Linsen, J. A. Rauwerda, and W. Wisselink, "Suture damage during robot-assisted vascular surgery: is it an issue?," *Surg Laparosc Endosc Percutan Tech,* vol. 17, pp. 524-7, Dec 2007.
[159] J. Martell, T. Elmer, N. Gopalsami, and Y. S. Park, "Visual measurement of suture strain for robotic surgery," *Comput Math Methods Med,* vol. 2011, p. 879086, 2011.
[160] H. S. Vitense, J. A. Jacko, and V. K. Emery, "Multimodal feedback: an assessment of performance and mental workload," *Ergonomics,* vol. 46, pp. 68-87, Jan 15 2003.
[161] C. E. Reiley, T. Akinbiyi, D. Burschka, D. C. Chang, A. M. Okamura, and D. D. Yuh, "Effects of visual force feedback on robot-assisted surgical task performance," *J Thorac Cardiovasc Surg,* vol. 135, pp. 196-202, Jan 2008.
[162] J. C. Gwilliam, M. Mahvash, B. Vagvolgyi, A. Vacharat, D. D. Yuh, and A. M. Okamura, "Effects of haptic and graphical force feedback on teleoperated palpation," pp. 677-682, 2009.
[163] A. Abiri, S. J. Askari, A. Tao, Y. Y. Juo, Y. Dai, J. Pensa*, et al.*, "Suture Breakage Warning System for Robotic Surgery," *IEEE Trans Biomed Eng,* Sep 10 2018.
[164] A. Abiri, O. Paydar, A. Tao, M. LaRocca, K. Liu, B. Genovese*, et al.*, "Tensile strength and failure load of sutures for robotic surgery," *Surg Endosc,* vol. 31, pp. 3258-3270, Aug 2017.
[165] M. Kitagawa, D. Dokko, A. M. Okamura, and D. D. Yuh, "Effect of sensory substitution on suture-manipulation forces for robotic surgical systems," *J Thorac Cardiovasc Surg,* vol. 129, pp. 151-8, Jan 2005.
[166] R. W. Livermore, A. C. M. Chong, D. J. Prohaska, F. W. FCooke, and T. L. TJones, "Knot security, loop security, and elongation of braided polyblend sutures used for arthroscopic knots," *Am J Orthop (Belle Mead NJ),* vol. 39, pp. 569-576, 2010.
[167] B. Allen, V. Nistor, E. Dutson, G. Carman, C. Lewis, and P. Faloutsos, "Support vector machines improve the accuracy of evaluation for the performance of laparoscopic training tasks," *Surg Endosc,* vol. 24, pp. 170-8, Jan 2010.
[168] (2011, Aug 09). *Sterilization Methods and Their Impact on Medical Devices Containing Electronics*. Available: https://www.maximintegrated.com/en/app-notes/index.mvp/id/5068
[169] "Standard Test Method for Determination of Effectiveness of Sterilization Processes for Reusable Medical Devices," ed: ASTM E1766-95, 2007.
[170] R. H. Dennard, F. H. Gaensslen, V. L. Rideout, E. Bassous, and A. R. LeBlanc, "Design of ion-implanted MOSFET's with very small physical dimensions," *IEEE Journal of Solid-State Circuits,* vol. 9, pp. 256-268, 1974.